Extreme galaxies: TeV gamma-ray emission from the Blazar 1ES 2344+514

Extreme Galaxies

TeV Gamma-ray Emission from the Blazar 1ES 2344+514

Mark Quinn B.Sc.

Thesis presented for the award of

Master of Science

Galway-Mayo Institute of Technology

Supervisor: Dr. P. Moriarty

Co-Supervisor: Prof. D. J. Fegan

Submitted to the Higher Education and Training Awards Council

July 2005

GMIT
GALWAY-MAYO INSTITUTE OF TECHNOLOGY
INSTITIÚID TEICNEOLAÍOCHTA NA GAILLIMHE-MAIGH EO

POSTGRADUATE CANDIDATE STATEMENT

THESIS PRESENTATION/AWARD

HETAC Postgraduate Research Degree Policy and Procedures require that a hardbound copy of the thesis be prepared in accordance with HETAC postgraduate research degree policy and procedures. Accordingly, there is a requirement for *"A Statement, signed by the candidate and the supervisor(s), indicating that the thesis represents the candidate's own work, or, in the case of a thesis based on a group project, indicating the extent of the candidate's individual contribution and making reference to any other theses submitted or material published by each collaborator in the project, should also be submitted at this time."*

Candidate Name: **MARK QUINN**
MRA Ref. **1850**
Register/Award **MSc**

Thesis Title: **EXTREME GALAXIES**

Supervisor : **Patrick Moriarty**

I, the above named, certify that the thesis wholly represents my own work.

Signature: Mark Quinn (Student) Date: 20/10/05

I, the above named Supervisor, certify that the thesis represents the candidate's work.

Signature: Patrick Moriarty (Supervisor) Date: 20/10/05

Abstract

This thesis describes an investigation of Very High Energy (VHE) gamma-ray emission from the blazar galaxy 1ES 2344+514, based on data from five observational seasons (1999-2004) using the Whipple 10-metre telescope in southern Arizona. The 65 hours of data consists mostly of tracking observations without contiguous OFF-source control data. A matching procedure was used to select a surrogate OFF-run compatible with each ON-source observation, to allow for determination of the background signal. Analyses of the data was carried out using both the standard Supercuts criteria and the multivariate kernel method.

The TeV flux of 1ES 2344+514, above 400 GeV, was determined to be $(0.29 \pm 0.14) \times 10^{-7}$ $m^{-2}s^{-1}$. To allow a comparison with the flux as determined by HEGRA from 1997 to 2002, the flux above 800 GeV was calculated to be $(0.07 \pm 0.04) \times 10^{-7} m^{-2}s^{-1}$. This compares very well with the HEGRA value, although it is noted that the uncertainties are a factor of two larger. An estimate of the spectral index of 1ES 2344 is derived from the quiescent flux values, although the uncertainty on the value is extremely large due to the limited statistics.

To my family.

Acknowledgements

The completion of this thesis marks the end of a chapter in my life, spanning almost 3 years, and would not have been possible without the encouragement and support of some key individuals.

My deepest gratitude goes to my supervisor Dr. Pat Moriarty, who provided me with valuable guidance and direction in my research, not to mention an uncountable number of hours spent proof reading successive drafts of this thesis. My sincerest thanks to you for your dedicated assistance and hard work in bringing this project to completion.

This work was undertaken at a time when postgraduate research at G.M.I.T. was in its infancy. I was indeed fortunate in having the facilities of a new physics research lab and the company of the other postgraduate students from within the Science department. A big thank you to Lisa, Karen, Brian, Gavin, Brenden, Andrew and Deirdre, for all the friendship, assistance and those many occasions of relieving lunch-time humour.

Part of my research was conducted at the Whipple Observatory in Tucson, and I must express thanks to my colleagues whom I worked with there, particularly John Kildea, Peter Cogan and Stella Bradbury. I am also grateful to Trevor Weekes, the VERITAS group leader, for his hospitality and inspiration during my time at the Whipple Observatory.

Last but not least, I must express my deepest thanks to my Family, who forever have being a source of support, love and happiness in my life.

Contents

List of Figures

List of Tables

Chapter 1

Introduction

1.1 The High-Energy Universe

The most conclusive evidence in revealing the high-energy nature of the universe is the phenomenon of **cosmic rays**. The energy of this cosmic radiation extends from 10^7 eV to beyond 10^{20} eV per particle, and clearly must originate in the most energetic environments in the universe, environments which operate as cosmic particle accelerators, such as supernovae, active galactic nuclei and gamma-ray bursts. The study of cosmic rays and their sources offers insight into complex electromagnetic processes, providing us with the greatest of natural laboratories that cannot be duplicated on Earth - places where we can question, discover and test our theories of high-energy physics with observation.

Since their discovery in 1912 the nature and origins of cosmic rays has been a central focus of astrophysics. From measurements made on board satellites and high-altitude balloons, it has been shown that these cosmic rays are charged particles travelling at speeds close to that of light. The majority are protons, although other heavier atomic nuclei are present, extending up to uranium. Since cosmic rays are charged particles their trajectories are altered by interstellar magnetic fields. They therefore arrive at Earth from random directions and carry little information regarding their source and origin. The true provenance of these

energetic particles remains one of the deepest mysteries of modern astrophysics.

It is evidently difficult to observe the high-energy universe from this charged component alone. However, neutrons, neutrinos and electromagnetic radiation are uncharged and so are not subject to magnetic deflections, and hence they can retain directional information. Unfortunately, neutrinos are extremely difficult to detect since they are weakly interacting, and free neutrons are unstable and can only reach Earth if they were extremely energetic. Electromagnetic radiation does not suffer these problems. While radio and optical photons provide indirect evidence of high-energy processes, study of the extreme high-energy regime requires detection of the highest energy photons: **gamma rays**. Indeed the history of gamma-ray astrophysics began long before experiments could provide detections, with work by Feenberg & Primakoff in 1948, Hayakawa & Hutchinson in 1952, and especially Morrison (1958) who advocated the potential importance of gamma-ray astronomy as a method of studying high-energy astrophysical processes directly.

Unfortunately, the detection of cosmic gamma rays is hindered by the Earth's dense atmosphere which prevents high-energy photons from passing through. This opacity is primarily due to attenuation from absorption, scattering and pair production. Life on Earth would not have evolved unshielded from this high-energy radiation. While this is fortunate in one respect it nevertheless poses a problem for scientists hoping to investigate extraterrestrial sources of such radiation. Furthermore, cosmic ray interactions with nuclei in the atmosphere give rise to a large background of secondary gamma rays, making detection of primary gamma radiation difficult.

Since the early theoretical speculations there have been many technological advances which has allowed for the first time the ability to detect photons at the highest energies. Within the past few decades a genesis has occurred which has seen many developments in both ground-based and satellite-borne gamma-ray detectors, revolutionising the field and moving it from a curiosity to a mainstream

branch of astronomy.

The gamma-ray energy domain is the most extensive of the electromagnetic spectrum, spanning at least fourteen decades in energy, from approximately

$$E = m_e c^2 \cong 0.5 \times 10^6 \text{eV} \text{ to } \geq 10^{20} \text{eV}$$

This range is as large as the rest of the observed spectrum combined and a variety of detector technologies is required to span it. Therefore it is convenient to introduce several subdivisions, taking into account the specific scientific objectives and detection methods relevant to different energy bands. Generally, observational gamma-ray astronomy can be divided into five areas, as defined by Weekes (2003). These conventional subdivisions are as above in Table 1.1.

Name	**Energy Range**	**Detector**
Low(LE)/Medium(ME)	0.1 - 30 MeV	Satellite
High Energy (HE)	30 MeV - 100 GeV	Satellite
Very High Energy (VHE)	100 GeV - 100 TeV	Ground-based: Cherenkov Telescope Air Shower Array > 10 TeV
Ultra High Energy (UHE)	> 0.1 PeV	Ground-based: Air Shower Array Fluorescence detector

Table 1.1: Energy bands and detection methods. Adapted from Weekes (2003)

While low- to high-energy gamma rays are observed by satellite- or balloon-borne detectors, the highest energy gamma-ray regimes (VHE and UHE) can be best addressed using ground-based instruments. It is the VHE range which is investigated in this thesis.

1.2 Gamma-Ray Production Mechanisms

Very-high-energy gamma rays are not produced from thermal processes. The total thermal emission from a hot body, such as a star, at temperature T varies as T^4. However, from Wien's displacement law, the emitted spectrum peaks

at $E_p \propto T$: $E_p/\mathrm{eV} \approx 4 \times 10^{-4} T/\mathrm{K}$. Even for stars with temperatures as high as 10^6 K, peak photon emission energy is less 1 keV. It is therefore clear that thermal processes cannot account for the production of VHE gamma radiation with photon energies exceeding 10^7 keV. We must therefore look to **non-thermal** processes for the origin of such radiation.

Non-thermal processes which can give rise to electromagnetic radiation include radioactive decay of nuclei or particles, collisions involving high-energy particles, particle-antiparticle annihilation and acceleration of charged particles. In this chapter, the principal processes relevant to the production of VHE photons are outlined, and some potential cosmic VHE sources are described.

1.2.1 Acceleration of Charged Particles

Electromagnetic radiation is emitted by charged particles whenever they are subject to an acceleration. To generate VHE photons it is necessary to accelerate particles to energies at least as high as the photon energy, and mechanisms by which this can occur form an integral part of models of TeV emission.

For a particle with charge q and mass m, subjected to an acceleration by a force F, the emitted power is given by:

$$P = \frac{q^2}{6\pi\varepsilon_0 c^3}\left(\frac{F}{m}\right)^2 \tag{1.1}$$

The radiation pattern is dipolar, and the radiation is polarised with the electric field vector lying parallel to the direction of acceleration. Since the emission power is inversely proportional to the square of the particle mass, a lower mass particle will radiate more energy per second for a given force than a heavier particle: electrons are 3×10^6 times more efficient at radiating energy than protons.

The mechanisms described in this section are primarily concerned with radiation from electrons. For example, high-energy electrons can produce gamma radiation as a result of electromagnetic interaction with nuclei (Bremsstrahlung), photons (inverse-Compton scattering) or magnetic fields (synchrotron radiation).

Each of these processes is described in more detail below.

Synchrotron Radiation

An electron moving in a magnetic field experiences a force which acts to constrain its motion to a helical path along the direction of the magnetic field lines. The acceleration experienced causes the electron to radiate, and for a low-energy electron, the radiation is dipolar and monochromatic.

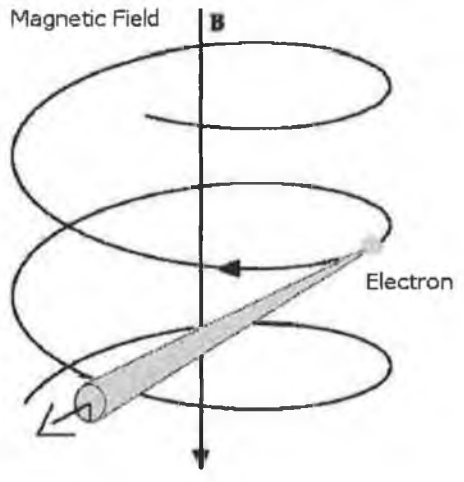

Figure 1.1: The gyration of an electron in a magnetic field.

If the electron is travelling **relativistically** with a **Lorentz factor** γ, the emission is beamed tangentially in a narrow cone of half angle $\sim 1/\gamma$ directed along the instantaneous direction of motion.[1] A continuous spectrum of polarised radiation results. The overall spectrum of the emission consists of the sum of a large number of harmonics of the basic cyclotron emission. The summed spectrum is relatively peaked, with maximum emission at 0.29 ν_c, where ν_c is the critical

[1]The Lorentz factor $\gamma = \frac{1}{\sqrt{1-\beta^2}}$ where $\beta = u/c$ with the particle velocity u and speed of light c.

frequency:

$$\nu_c = \frac{\gamma^2 eB}{2\pi m_e} \tag{1.2}$$

and B is the magnetic field strength perpendicular to the direction of motion. While emitting synchrotron radiation an electron will 'cool' as its energy is degraded. The rate of this cooling is given by:

$$\frac{dE_e}{dt} = 10^{-14} B^2 \gamma^2 \tag{1.3}$$

therefore and the electron will lose half its energy by synchrotron emission in a time t given by:

$$t = \frac{5}{\gamma B^2} \tag{1.4}$$

An electron population radiating in an astrophysical environment will typically have a power-law spectrum:

$$\frac{dN_e}{dE_e} \propto E_e^{-p} \tag{1.5}$$

and the resulting synchrotron radiation will have a spectral energy distribution $F_\nu \propto \nu^\alpha$ where

$$\alpha = \frac{1-p}{2} \tag{1.6}$$

The study of the synchrotron spectrum can provide much insight into the particle population within a cosmic accelerator. It can be noted that higher-energy electrons radiate more rapidly and thus lose energy faster. The depletion of the higher energy electrons would lead to a steeper power-law synchrotron spectrum above the critical frequency (ν_c) which is dependent on the magnetic field (see Figure 1.2).

A source emitting high-energy radiation with a power-law spectrum and with a high degree of polarisation would generally indicate that synchrotron accelera-

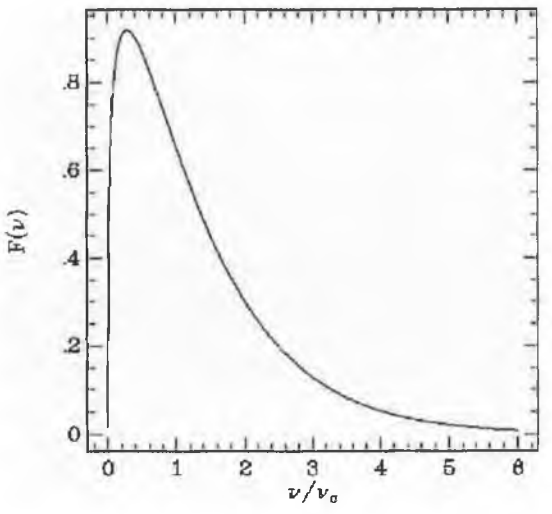

Figure 1.2: Frequency distribution of synchrotron electrons showing the characteristic peak emission near $0.29\nu_c$ where ν_c is the critical frequency as defined in Equation 1.2

tion is present. To produce gamma rays directly by synchrotron radiation, either the electrons must be very highly relativistic, or a very intense magnetic field is required. Investigating the ratio of polarised to unpolarised emission can provide an indication of the uniformity of the source magnetic field in astrophysical environments. The observation of a synchrotron component can also indicate the presence of relativistic electrons which may provide a target field for photons and generate high-energy gamma rays by the inverse-Compton mechanism.

Inverse-Compton Scattering

Compton scattering implies a photon colliding with an electron causing a transfer of energy from the photon to the electron. The reverse process, inverse-Compton scattering, occurs when a low-energy photon gains energy from an interaction with a high-energy electron. This interaction is of considerable importance in astrophysical environments where the density of low-energy photons is high and where there is a supply of relativistic electrons.

In the collision between a relativistic electron with energy $E_e = \gamma m_e c^2$ and a photon of energy $\varepsilon = h\nu$, the scattered photon energy in the laboratory system,

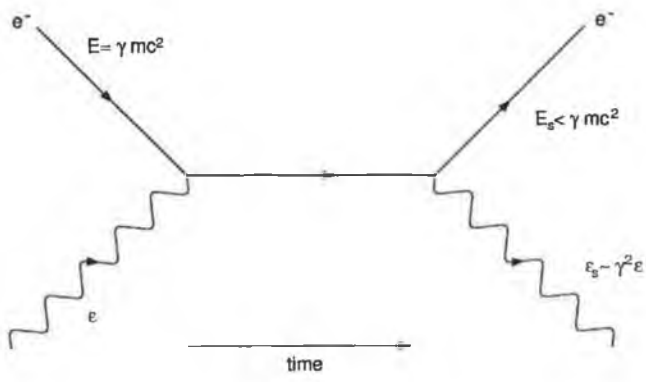

Figure 1.3: Inverse-Compton scattering of a relativistic electron with a photon.

averaged over all angles of incidence and scattering, is $\approx \frac{4}{3}\gamma^2\varepsilon$. This process can easily turn a radio photon into a gamma-ray photon. The low-energy photons may belong to the cosmic background radiation ($T = 2.7$ K), which has an energy density of 0.4×10^{-13} J.m^{-3}. Alternatively, the low-energy photons may be the synchrotron photons emitted by the energetic electron population itself. In the latter case the process can be described as **synchrotron self-Compton** (SSC) scattering.

The energy transferred to the photon depends on the cross-section and on the scattering angle at which the electron and photon meet. For a maximum energy transfer (E_{max}), the particles must meet head-on, reversing the photon direction in the collision, while a minimum energy (E_{min}) will be transferred when the scattering angle is 90°.

The probability of the electron-photon interaction, i.e. the cross-section, is given by the **Klein-Nishina** formula:

$$\sigma_{\mathrm{KN}} = \pi r_e^2 \frac{1}{\eta}\left[\left(1 - \frac{2(\eta+1)}{\eta^2}\right)\ln(2\eta+1) + \frac{1}{2} + \frac{4}{\eta} - \frac{1}{2(2\eta+1)^2}\right] \qquad (1.7)$$

where $\eta = \gamma\varepsilon/m_e c$, and $r_e = 2.818 \times 10^{-15}$m is the classical electron radius.

For low-energy collisions, the cross-section is simply the **Thomson cross-section** $\sigma_T = \frac{8}{3}\pi r_e^2$, independent of energy. However, for very high energy electron-photon interactions ($\varepsilon >> m_e c^2$) the Klein-Nishina formula reduces to:

$$\sigma \approx \frac{3}{8}\sigma_T \frac{m_e c^2}{\gamma\varepsilon}\left[\ln\left(\frac{2\gamma\varepsilon}{m_e c^2}\right) + \frac{1}{2}\right] \propto \frac{\ln E_e}{E_e} \tag{1.8}$$

so that the interaction probability decreases at higher energies. In this regime, the electron energy loss through scattering becomes independent of the incident photon energy. Such an **ultra-relativistic encounter** (with $\varepsilon >> m_e c^2$) would yield photon energies:

$$E_{\min} \approx \frac{m_e c^2}{4\gamma}$$

$$E_{\max} \approx E_e = \gamma m_e c^2$$

Using a power-law energy distribution for the electrons, $dN_e/dE_e \propto E_e^{-\alpha}$, the inverse-Compton spectrum takes the form of a two-component distribution peaking on the border between the Thomson and Klein-Nishina regimes where $\frac{4}{3}\gamma^2\varepsilon \sim \gamma m_e c^2$ (Figure 1.4).

Bremsstrahlung

When charged particles are deflected by an electrostatic field they emit photons by the process known as Bremsstrahlung. The rapid deceleration of a high-energy electron by the field of a nucleus can lead to a large fraction of the electron energy being radiated as a photon.

The total energy loss ($-dE$) per path length (dx) averaged over all radiated frequencies (up to the initial energy of the electron) is:

$$\left\langle -\frac{dE}{dx}\right\rangle_{brem} = \frac{P_{brem}}{c} = \frac{E}{L_{brem}} \propto Z^2 \ln\left(Z^{-\frac{1}{3}}\right) E \tag{1.9}$$

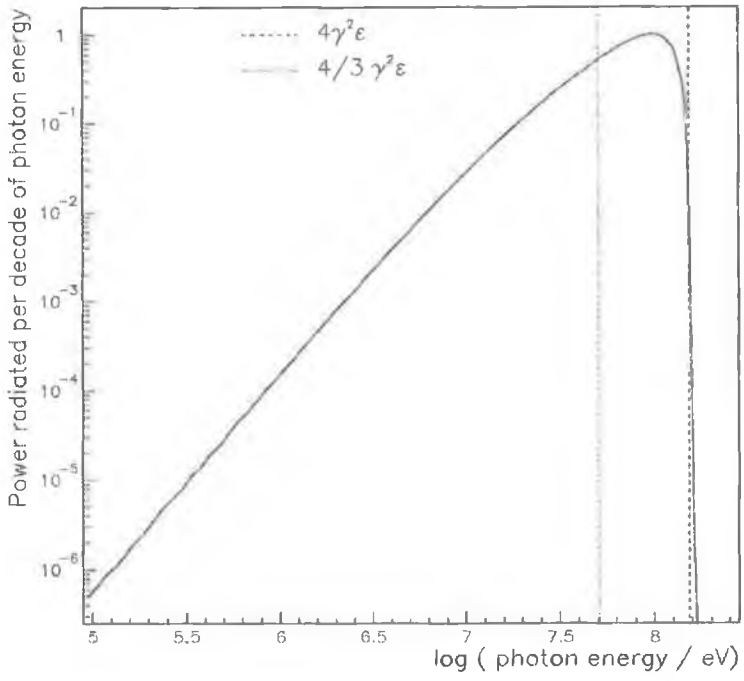

Figure 1.4: The energy distribution for the inverse-Compton scattering of a relativistic 10 GeV electron with a 0.1 eV photon (Skelton 1999).

where P_{brem} is the power radiated through Bremsstrahlung and L_{brem} is the radiation length. The thickness of the atmosphere (roughly 1000 g.cm^{-2}) is equivalent to $\sim 25 L_{brem}$ in air. Energy dissipation is proportional to electron energy E and atomic number Z and therefore becomes important for high-energy electrons and heavier target nuclei. The solution of Equation 1.9 is:

$$E = E_0 e^{-\frac{x}{L_{brem}}} \tag{1.10}$$

Bremsstrahlung plays an important role in gamma-ray production by cosmic ray electrons in the **interstellar medium** (ISM). The development of electromagnetic cascades in the upper atmosphere, an important element in ground-based gamma-ray detection, also depends heavily on Bremsstrahlung.

1.2.2 Particle Decay

Gamma rays are produced in the decay of some elementary particles. The most important decay process for astrophysical gamma-ray generation is the decay of neutral pions (π^0). Neutral pions are one of the by-products from nuclear collisions of hadronic particles and have a very short lifetime, 0.84×10^{-16}s (Eiderlman et al. 2004). The decay process produces two gamma-ray photons:

$$\pi^0 \rightarrow \gamma + \gamma \tag{1.11}$$

Each photon will have approximately half the total energy of the π^0. VHE and UHE gamma rays can therefore result from the decay of neutral pions with sufficiently high energies.

1.2.3 Particle/Antiparticle Annihilation

When a particle interacts with its antiparticle, e.g., an electron and a positron, their combined mass-energy together with their kinetic energy can be released in the form of two or more gamma-ray photons. The rest-energy of an electron is 0.511 MeV. Therefore an electron/positron annihilation occurring at rest will produce two gamma-ray photons, each with an energy of 0.511 MeV.

1.3 Sources of VHE Gamma Rays

VHE gamma rays are produced near the most violent astrophysical regions in the universe. Several such sources are listed in Table 1.2.

So far only a handful of sources with energy above 100 GeV have been confirmed (three shell-type supernova remnants, six active galactic nuclei and four pulsar nebulae) but this situation is currently in a state of flux as the H.E.S.S. array (Section 2.4.2) uncovers new sources.

Object	Type	Dist
Crab Nebula	SNR	2 kpc
RX J1713-3946	SNR	1.5 kpc
PSR B1259-63	Pulsar binary	1.5 kpc
Galactic Centre	-	8 kpc
Mrk 421	AGN	122 Mpc
Mrk 501	AGN	138 Mpc
1ES 2344+514	AGN	177 Mpc
1ES 1959+650	AGN	189 Mpc
PKS 2155-304	AGN	445 Mpc
H 1426+428	AGN	490 Mpc

Table 1.2: A summary of the VHE source catalogue as of 2004

1.3.1 Supernova Remnants

The evolution of a star is largely dependent on its mass, which dictates the size of the gravitational potential and the rate of nuclear fusion. The evolution of large stars with mass greater than 3 $M_{\odot}$ can climax in the destructive transformation of a supernova and may offer many possibilities for high-energy gamma-ray production.[2]

Supernova explosions have durations of the order of seconds, and result in the violent ejection of stellar material into space. As much as 10^{44} J may be transferred as kinetic energy to the rapidly moving ejecta. The gaseous cloud, composed of constituents of the former star, is termed a **Supernova Remnant** (SNR). If there remains a core of the original star, it can continue to be quite active. If conditions are right the immediate aftermath of a supernova may bequeath a pulsar (a rapidly rotating sphere of neutrons) or indeed a black hole, either of which would provide an energy source within the remnant to drive subsequent high-energy emission.

Depending on its morphology, the remnant may display emission from a spherical shell (**shell-type**) or from a filled centre (**plerion**). A number of remnants have both a shell and plerionic component. In a plerion such as the **Crab Nebula**, the high-energy electrons emit radio to x-ray **synchrotron** radiation as they

[2] $M_{\odot}$: mass of the Sun : 1.9891 x 10^{30}kg

travel through the magnetic field of the inner nebula. The electrons are continually injected into the nebula from the pulsar. The **inverse-Compton** scattering of the synchrotron electrons on the ambient photons produces the subsequent rise in the energy distribution above 400 MeV to the VHE region, and its later decay towards the highest measured photon energies of 50 TeV. This behaviour results in two distinct peaks in the spectral energy distribution (SED), as seen in Figure 1.5 . The Crab Nebula is a strong, steady source first detected at TeV energies by the Whipple telescope in 1989 (Weekes 1989). It is now considered the standard candle for VHE astronomy (Aharonian et al. 2004a), and it is routinely used for instrument calibration and the development of analysis techniques. The flux from a VHE source is sometimes quoted in units of the Crab Nebula flux. [3]

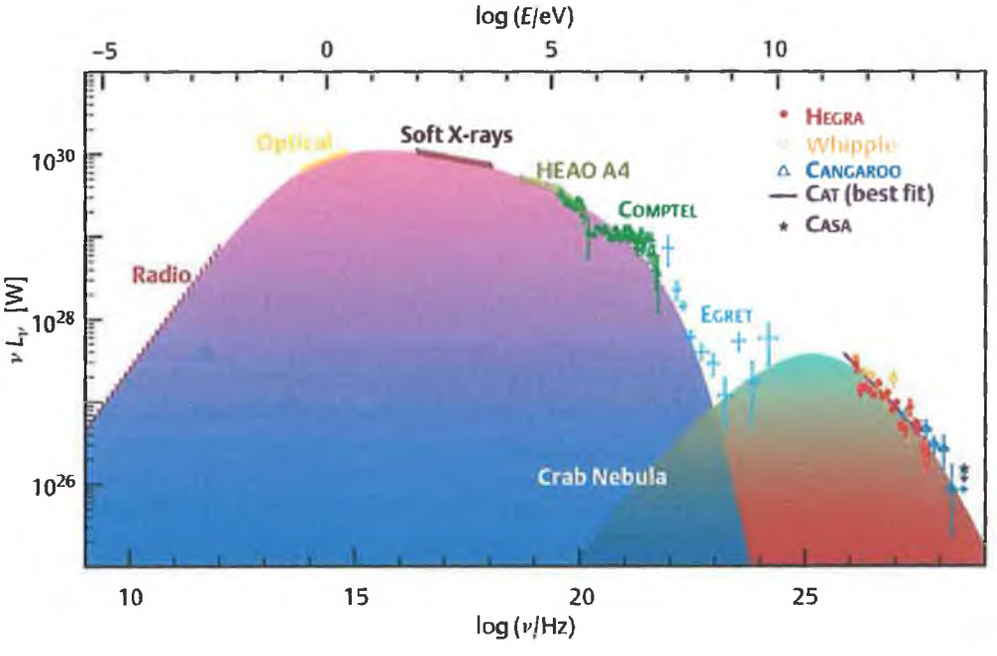

Figure 1.5: The broad-band spectral energy distribution of the emission from the Crab Nebula.

Another possible mechanism by which supernovae can create gamma rays is the acceleration of charged particles in a **shock front**. This acceleration is

[3]The VHE gamma-ray flux of the Crab Nebula above 1 TeV, as quoted by Hillas et al. (1998), is $(2.1 \pm 0.2) \times 10^{-7}$ m^{-2} s^{-1}.

thought to be the origin of cosmic-rays with energies up to 100 TeV. A shock front can be formed as a result of supernova ejecta travelling into the **interstellar medium** (ISM) at supersonic velocity. Particles crossing the shock front may be scattered back and forth repeatedly across the shock boundary and in doing so, gain energy by first-order **Fermi acceleration** (see Drury et al. (1994)). As the energy increases, the particle is increasingly likely to escape the diffusive acceleration process. However, escape is only possible into the region downstream of the shock, i.e. to the inside of the SNR shell.

SNRs offer the most potential in establishing the origin of high-energy cosmic rays. With the lack of sufficient spatial resolution to resolve the extended SNR source, direct evidence has been wanting. Recently a TeV detection at the 20σ level[4] has been reported by **H.E.S.S.** from the SNR RX J1713.7 (Aharonian et al. 2004b). Achieving a precision of 1 arcminute has revealed the shell structure of the SNR (Berge et al. 2005). There appears to be a strong spatial correlation between the H.E.S.S. gamma-ray data and the x-ray data which demonstrates that very high energy particles are being generated there. This shell-type remnant was first claimed to emit in the TeV regime by the **CANGAROO** group (Muraishi et al. 2000).

1.3.2 Active Galactic Nuclei (AGN)

Active galactic nuclei involve the most powerful sources of luminosity in the Universe. They range from the nuclei of some nearby galaxies emitting approximately 10^{33} W to distant quasars emitting more than 10^{40} W. The emission is spread widely across the electromagnetic spectrum, often peaking in the ultraviolet, and with significant luminosity in the x-ray and infrared bands. The emission is spatially unresolved except in the radio band, where there is sometimes evidence for collimated outflows ('jets') travelling at relativistic speeds (Figure 1.6). The power output of AGN is typically variable on time scales of years, and sometimes

[4]The quantity σ represents the strength of a detected gamma-ray signal, i.e. the number of standard deviations above the background level.

on time scales of days, hours, or even minutes. Causality implies that the variation period of an object must be greater than the time for light to cross that object. The observed emission variability, therefore, provides an upper bound to the diameter of the emission region in AGN. The very high luminosities imply high masses whose gravity can combat the radiation pressure that would otherwise blow the object apart.

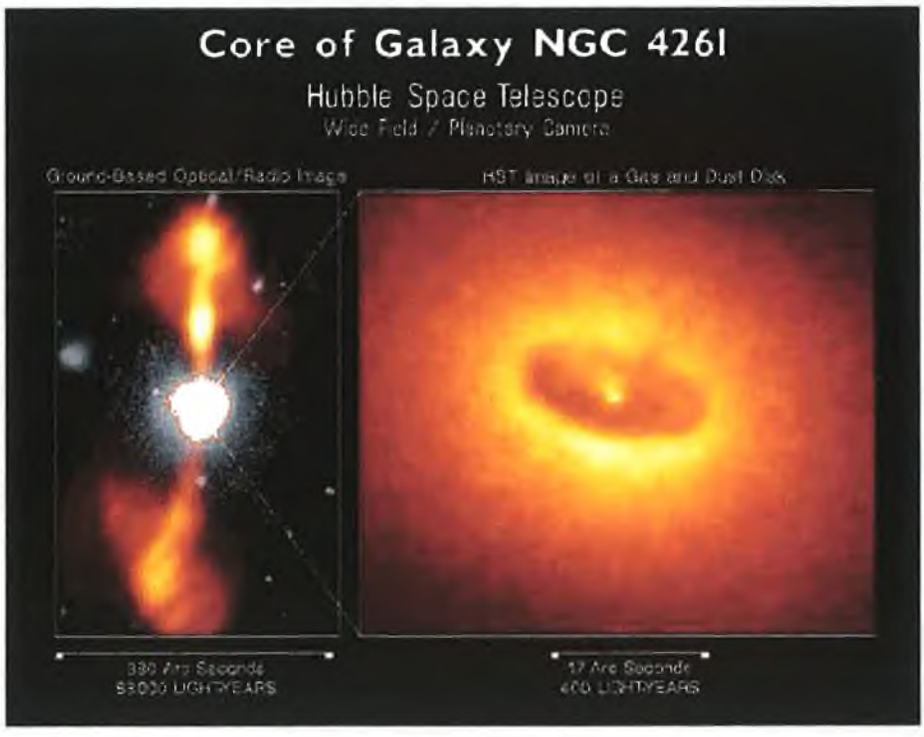

Figure 1.6: Hubble Telescope images of active galaxy NGC 4261

It is now well established that AGN are strong gamma-ray ($E > 100$ MeV) emitters. To be more specific: at least 40% of all EGRET (see Section 2.2) sources are AGN (Thompson 1995), and they make up almost 100% of all identified extragalactic sources seen by this high-energy detector.

TeV gamma rays have only been detected from a class of AGN known as **blazars**, that is BL Lacertae objects (BL Lacs) or flat-spectrum radio quasars (FSRQ). A total of six confirmed AGN have been detected in the VHE regime. The TeV emission from AGN is discussed in more detail in Chapter 4.

1.3.3 X-Ray Binaries

X-ray binaries consist of a collapsed star (usually a neutron star or black hole) and a main sequence star in a tight orbit around a common centre of mass. The intense gravity from the collapsed star pulls matter off the companion star. This matters spirals onto the collapsed star and forms an accretion disk. X-rays originate from the inner region of the accretion disk where the temperature can reach millions of degrees. Many x-ray binary systems are observed to have jets. X-ray binaries might therefore be expected to produce TeV photons through physical processes similar to those in AGN.

The Durham group reported steady unpulsed emission from the x-ray binary Centaurus X-3 (Chadwick 1998), which consists of a 4.8 s pulsar and a companion O-type star. This emission is thought to originate from a region where the interaction of the pulsar's relativistic wind and the companion star creates a shock front. Recently the H.E.S.S. group reported a detection from the millisecond binary PSR 1259-63 (Beilicke et al. 2004), emitting at 10% of the level of the Crab Nebula flux.

1.3.4 Other Potential VHE Sources

Gamma-Ray Bursts

Gamma-ray bursts (GRBs) are short duration, highly intense bursts of hard x-rays and gamma rays from random directions and times in the sky. They are classified as "short" or "long" depending on whether their duration is shorter or longer than 2 s, but the duration is difficult to quantify as it is dependent upon the sensitivity and time resolution of the detecting system.

Since their accidental discovery in 1967, by detectors onboard the American Vela satellites, many subsequent scientific satellites (notably BATSE, BeppoSAX and HETE2) have provided crucial evidence in isolating and identifying the origin of GRBs. In the first years after their discovery, gamma-ray bursts were observed

at the rate of 10 to 20 per year. Now, with more complete coverage and larger detectors, bursts are detected at the rate of over 300 per year.

The **long-duration GRBs** seem to occur outside the Milky Way, and are though to be of cosmological origin. With the measurements of emission and absorption lines from the host galaxies of the GRBs the determination of redshifts has been possible, establishing the extragalactic origin of the long duration GRBs. Today the redshifts of only a handful are known, most have redshifts around $z = 1$, while the most distant lies at a redshift of about 4.5. Long bursts are found occurring predominantly in galaxies with active star formation (Bloom et al. 1999). The idea of a long-GRB/supernova connection has been corroborated by the detection of a very energetic supernova that occurred temporally and spatially coincident with GRB030329 (Hjorth et al. 2003). Thus (at least some of the) long bursts seem to be associated directly with core-collapse supernovae.

The origin of **short bursts** remains in doubt. These bursts, which make up about one-third of all observed GRBs, differ markedly from long ones not only in duration but also in their energy distribution. The spectra of short GRBs are harder (Kouveliotou 1993) - that is, they have a larger fraction of high-energy photons - and their peak energy is higher (Paciesas et al. 2001). Statistical arguments (Mao et al. 1994) also point to a relatively local origin of the short GRB class. They may result either from a special kind of stellar collapse, or from the merger of two compact neutron stars or of a neutron star and a black hole.

A case for jet-like emission from GRBs can be based on the presence of achromatic breaks, which have been identified in several bursts and (under certain assumptions) jet opening angles of $\sim 5^\circ$ have been derived (Frail 2001). The beaming theory implies lower GRB energy then would be required if the emission were isotropic and also supplies the ultrarelativistic effects required to produce the observed non-thermal spectrum and rapid variability. Moreover, if the gamma-ray emission is beamed into a narrow jet, this would mean that the "true" event rate is much higher than the observed rate.

Starburst Galaxies

Starburst galaxies contain areas where formation of stars occurs at about 100 times the rate found in more normal galaxies (such as the Milky Way). Such high rates of star formation imply a high frequency of supernovae and a high cosmic ray density (Völk et al. 1989). There could also be a plasma wind emerging from the galaxy.

Starburst galaxies are predicted to be gamma-ray sources based on the existence of the terminal shock of this stellar wind and the high supernova rate. The CANGAROO group claimed a TeV detection from NGC 253 at the 11σ level (Itoh et al. 2003), with emission that may originate from the extended galactic halo. Unfortunately, recent observations by the H.E.S.S. group have failed to detect any significant signal from this object (Aharonian et al. 2005a). Observations of M 82 and IC 342 in the northern hemisphere have also proved negative thus far.

The Galactic Centre

The centre of the Milky Way galaxy is one of the most interesting regions of the Galaxy. Continued monitoring of the Galactic Centre by the Chandra X-ray Observatory has recently revealed the presence of many compact objects surrounding the mysterious, suspected supermassive black hole called Sagittarius A* (Baganoff et al. 2003). These compact objects are characterised by dramatic x-ray variability and are most likely either neutron stars or black holes

The Galactic Centre has been observed by many VHE experiments including the VERITAS (Kosack et al. 2004) and CANGAROO (Tsuchiya 2004) groups; the most definitive result comes from the H.E.S.S. experiment, which has detected VHE emission at the 9σ level (Aharonian et al. 2004c). The measured flux is $\sim 5\%$ of the Crab Nebula flux in the VHE regime but the precise source is uncertain. The gamma radiation could result from acceleration of electrons or protons in shocks in the accretion flow or in nearby supernova remnants, fol-

lowed by interactions of accelerated particles with ambient matter or radiation. Alternative mechanisms include the annihilation of dark-matter particles accumulating at the Galactic Centre (Gnedin & Primack 2004) or curvature radiation of protons near the black hole (Levinson 2000). The nature of the source and the production mechanism are still not clear, and so a longer exposure is needed.

1.4 Thesis Overview

Chapter 2 discusses the range of experimental techniques used to detect the high energy sources discussed above. Chapter 3 will document the design and operation of the Whipple 10 metre telescope. Chapter 4 deals with the classification and physics of AGN in detail. Current schemes for unification are discussed along with models of gamma-ray production. Chapter 5 discusses the analysis methodology, the standard Supercuts method applied to matched pairs, and a relatively new approach to gamma-ray discrimination, the kernel method. In Chapter 6 these analysis techniques are applied to data from the active galaxy 1ES 2344+514, recorded using the Whipple telescope over five observing seasons. This final chapter summarises the results of the application of the analyses to the dataset, with a discussion of results and conclusions.

Chapter 2

Detection of High Energy Gamma-ray Radiation

2.1 Introduction

The gamma-ray 'window' represents the final frontier in astronomy. First glimpsed over the later decades of the twentieth century, this frontier is fast becoming a more charted terrain. Spectral coverage up to 10 GeV and from 100 GeV to over 10 TeV has been provided by past and current observations. The gap in between will be explored by new experiments.

Since the first theoretical advocation, the practical techniques of gamma-ray detection have had to deal with some important natural limits:

- The flux of high-energy gamma rays from astrophysical sources is quite low and decreases rapidly with increasing energy. For example, Vela (the strongest gamma-ray source in the sky at energies above 100 MeV) has a flux of only 1.3×10^{-1} photons m^{-2} s^{-1} and a differential flux that falls as $E^{-1.89}$. This implies the need for detectors with large collection areas in order to detect the gamma-ray signal at a sufficient statistical significance above the background. For example, a detector with a collection area of ~ 0.1 m^2 will detect about one photon/minute above 100 MeV from Vela,

and only one photon every two hours above 10 GeV.

- It is not possible to reflect and concentrate a beam of gamma-ray photons using lenses and mirrors as with visible light in traditional optical telescopes. Gamma-ray photons can however be detected by collecting the electrons emitted when striking high density materials such as sodium iodide. Three major types of interaction play an important role in radiation measurements and all these processes lead to the partial or complete transfer of the gamma-ray photon energy to electron. Photoelectric absorption predominates for low-energy gamma rays (up to several tens of keV) for the heaviest elements. Pair production predominates for high-energy gamma rays (above 5 MeV). Compton scattering is the most probable process over the range of energies between these extremes. The atomic number of the interaction medium and the energy of the gamma-ray photon have a strong influence on the relative probabilities of the interactions.

- At high energies the flux of charged cosmic rays is much larger than the gamma-ray flux. This makes it essential to develop rejection techniques for the large cosmic-ray background in high-energy gamma-ray astronomy.

- The Earth's atmosphere is opaque to high-energy photons. The probability that a high-energy photon will reach ground level without interacting electromagnetically is negligibly small even at mountain altitudes. Due to this atmospheric absorption it is necessary to place gamma-ray detectors either above the atmosphere on board satellites or balloons, or to use indirect methods to detect gamma-rays from the ground (see Figure 2.1).

2.2 Space-Based Detection

The advent of gamma-ray astronomy has been in the form of orbiting satellite detectors, using techniques akin to nuclear physics to detect and measure incoming

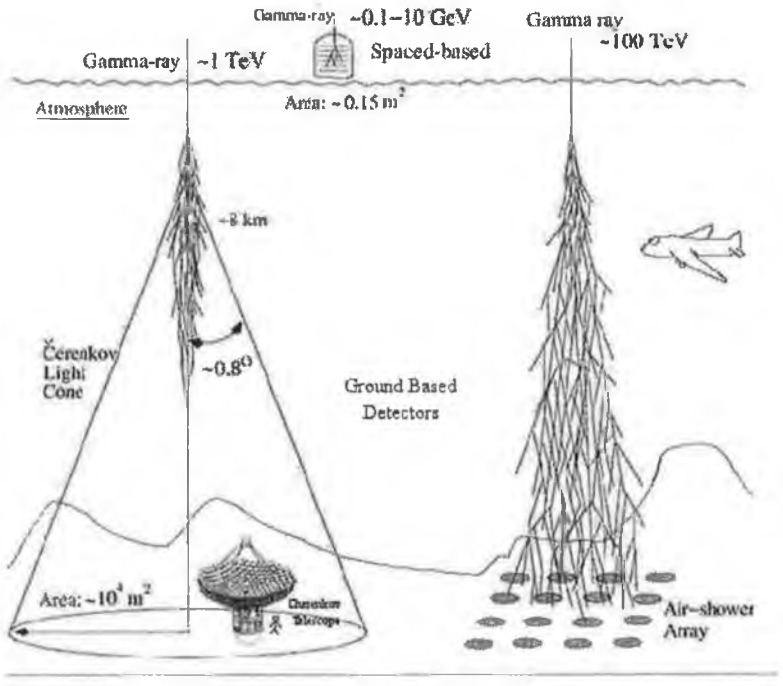

Figure 2.1: The main gamma-ray detector types

cosmic photons.

Gamma-ray photons with energies > 10 MeV entering the detector are absorbed to produce electron-positron pairs. The photon direction is determined with tracking detectors, and its energy is usually measured with total-absorption calorimeters. At lower energies, photons are detected via Compton scattering and the photoelectric effect. Charged cosmic rays are rejected by the use of anti-coincidence shielding so satellite detectors suffer from very little background. Other qualities relevant to space-based detectors are good angular resolution, important for identifying point sources, and good energy resolution which is needed to determine the energy spectrum of the source.

Another important parameter of a satellite-based detector is its **effective collection area**, defined as:

$$A_{eff}(E) = \frac{N}{f(E)T} \tag{2.1}$$

where T is the observation time and N is the number of events recorded, and $f(E)$ is the photon flux to which the detector is exposed in units of photons.m^{-2}.s^{-1}. At low energies, the effective area rises with increasing energy because the photon conversion probability rises. Angular and energy resolution also generally improve with increasing energy.

The first high-energy detector, **Explorer 11**, was launched in 1961 and was sensitive to photon energies greater than 50 MeV. While this satellite detected only 22 cosmic gamma rays, 621 events were detected by the **OSO-3** satellite in 1967. In 1973, detection of gamma rays from the Crab pulsar was reported using a balloon-borne experiment (McBreen et al. 1973), the first detection of a discrete source in this energy range. Unfortunately balloon experiments suffer from a short exposure time and large-albedo gamma-ray background. Other satellite experiments, SAS-2 and COS-B, made the next significant advance in the field. The **COS-B** gamma detector covered a energy range between 70 MeV and 1 GeV, with an effective collection area around 50 cm^2 depending on the incident photon energy. The **SAS-2** detector employed a spark-chamber detector with an anti-coincidence shield, and as such was the prototype for modern high-energy gamma-ray telescopes. Among the results achieved by these early satellites were precise observations of the diffuse flux coming from the galactic plane and the detection of pulsed gamma-ray radiation from the Vela and Crab pulsars.

2.2.1 Energetic Gamma Ray Experiment Telescope

The Energetic Gamma Ray Experiment Telescope (**EGRET**) was the largest gamma-ray space-based detector operated to date and has had a huge impact on the field of high-energy astronomy. EGRET has also been an important guide for VHE astronomy, providing many new sources for target observation lists. The instrument, launched into orbit in 1991 aboard the Compton Gamma Ray Observatory, was a facility consisting of four telescopes, with continuous coverage of the energy range 30 keV to 30 GeV and a tenfold increase in sensitivity over

previous experiments.

EGRET was similar to the earlier COS-B but much larger, with an effective area 25 times greater. The angular resolution ranged from 5.5° for the lower energies to 0.4° for the upper threshold energy. Among the highlights of the EGRET mission was the detection of more than **70 AGN** and **7 pulsars** (Mukherjee et al. 1997; Hartman et al. 1999). The EGRET experiment also detected many unidentified sources, not associated with any known object at other energies. Many of these unidentified objects populate the galactic equator and hence may be galactic in nature. About 40% of these sources have hard power-law spectra which seem to extend beyond 10 GeV. The nature of the large number of unidentified sources discovered by the EGRET experiment may be partially uncovered by a more accurate determination of their positions.

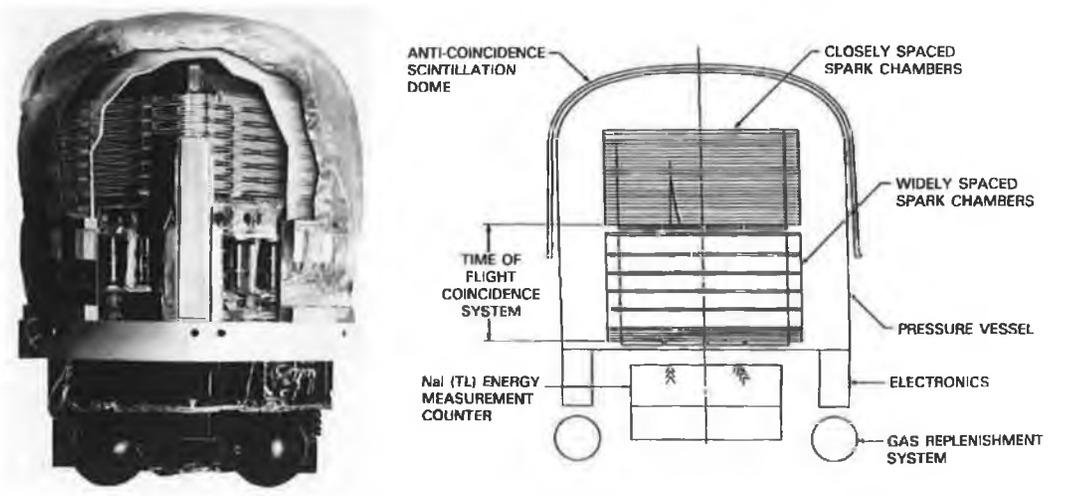

Figure 2.2: The EGRET gamma-ray detector (left) with schematic (right). (Images from NASA).

The EGRET experiment had a design typical of spark-chamber telescopes and consisted of four main components (Figure 2.2). A plastic scintillator anticoincidence shield was mounted over the aperture of the instrument to identify charged cosmic ray events. Beneath this, a gas-filled pressure vessel contained the gamma-ray tracking system. An upper spark chamber, consisting of 28 wire

grid electrodes interleaved with tantalum foil, converted incident gamma rays to electron pairs. This was triggered by a time-of-flight coincidence system composed of two scintillation detectors situated beneath the spark chamber. For the spark chamber to be triggered, the electron-positron pair must be moving in the downward direction and there must be no signal recorded by the anticoincidence shield. Between the two scintillation detectors there were a number of more widely spaced spark-chamber electrodes for better determination of the positron and electron directions. The final component, located at the base of the instrument, was the Total Absorption Spectrometer Crystal (TASC). This thick (eight radiation lengths) NaI scintillator absorbed the energy of the electron-positron pair and provided an estimate of the primary photon energy.

2.2.2 BeppoSAX

BeppoSAX, a program of the Italian Space Agency and the Netherlands Agency for Aerospace Programs, was launched on April 30 1996 from Cape Canaveral and operated for 6 years. It was the first x-ray mission with a scientific payload covering more than three decades of energy (from 0.1 to 300 keV) with a relatively large effective area, medium energy resolution and imaging capabilities in the energy range of 0.1-10 keV.

Some of the scientific highlights of the BeppoSAX experiment were:

- First arcminute positions of gamma-ray bursts.
- First x-ray follow-up observations and monitoring of a gamma-ray burst.
- Broad-band spectroscopy of different classes of x-ray sources.

2.2.3 INTEGRAL

INTEGRAL, launched in 2002 consists of four instruments, a gamma-ray spectrometer (20 keV - 8 MeV), an imager (15 keV - 10 MeV), an x-ray monitor (3 -

35 keV) and an optical monitor.

The combination of these four instruments has allowed INTEGRAL to observe sources simultaneously in optical, x-rays and gamma rays with high spectral and spatial resolution.

Some of the scientific highlights of the INTEGRAL mission are:

- First map of parts of the Galactic plane in the light of nuclear gamma rays emitted by decaying atomic nuclei.
- Discovery of what seems to be a new class of astronomical objects. These are binary systems, probably including a black hole or a neutron star, embedded in a thick cocoon of cold gas. They have remained invisible so far to all other telescopes.
- Solution of a thirty-year-old question by resolving the diffuse glow of gamma rays in the centre of our galaxy and showing that most of it is produced as superposition of radiation from many individual sources.
- Further evidence (together with XMM-Newton) that massive black holes are surrounded by a toroidal gas cloud.
- Gamma-ray burst GRB 031203, detected by INTEGRAL, is the closest cosmic gamma-ray burst on record. It is also the faintest gamma-ray burst on record, suggesting that an entire population of sub-energetic gamma-ray bursts may so far have gone unnoticed.

2.2.4 Swift

Launched into a low-Earth orbit on November 20, 2004, the main purposes of this mission is to respond 'swiftly' to measure the location of GRBs and determine if there is also an afterglow signal in the longer wavelengths of x-rays, UV and optical. Swift has three main co-aligned instruments onboard:

1. the Burst Alert Telescope (BAT),

2. the X-ray telescope (XRT),

3. and the UV/Optical telescope (UVOT).

BAT is a coded-aperture gamma-ray imager with a wide field-of-view that will produce arcminute GRB positions onboard within 10 seconds. The spacecraft will execute a rapid autonomous slew that will point the x-ray and ultraviolet (UV) telescopes at the BAT position in typically ~50 s, to provide the critical afterglow data. The XRT and UVOT will produce sub-arcsecond positions and multiwavelength lightcurves of the afterglow. Redshifts for the majority of the GRBs will be calculated from broad-band spectroscopy.

2.2.5 GLAST

The Gamma-ray Large Area Space Telescope is scheduled to launch in May 2007. Although it follows the same basic principles as EGRET, GLAST employs new technologies to improve dramatically the performance of the system. The detector is composed of alternate sheets of high-Z absorber interlaced with silicon strip detectors for tracking motion of electron-positron pairs. This has a number of advantages over a spark-chamber system. The silicon strip detectors are inexpensive, lightweight and can offer a long lifetime, since no consumable materials are used in their operation (such as gas in a spark chamber). In addition, no separate triggering system is required. An upper strip detector will act as a charged-particle anti-coincidence shield, and energy measurement will be provided by a segmented CsI calorimeter located beneath the layered strip detector. Compared to EGRET, GLAST is expected to have a number of significant improvements in performance:

- Tenfold increase in collection area.
- Fivefold increase in field of view.
- Wider energy coverage (10 MeV - 300 GeV).

- Improved energy resolution, particularly at high energies.
- Tenfold improvement in point source location.
- 1-2 order of magnitude increase in point-source sensitivity.

Name	Period	Range
SAS-2	1972-1973	30 MeV - 200 MeV
COS-B	1975-1982	30 MeV - 5 GeV
EGRET	1991-2000	20 MeV - 30 GeV
BeppoSAX	1996-2002	0.1 keV - 300 keV
INTEGRAL	2002 $\rightarrow$	15 keV - 10 MeV
Swift	2004 $\rightarrow$	$<$ 150 keV
AGILE	2005 $\rightarrow$	30 MeV - 50 GeV
GLAST	2007 $\rightarrow$	10 MeV - 100 GeV

Table 2.1: A summary of space-based gamma-ray detectors.

The falling flux of gamma rays at higher energies necessitates larger collection areas. The limited size of space-based detectors prevents them from observing above a few hundred GeV. To extend past these energy limits and to observe effectively within the very high-energy domain requires other observing techniques. With collection areas approaching 5×10^4 m^2, ground-based detectors offer a solution to this problem.

2.3 Ground-Based Detection

Ground-based gamma-ray detectors are fundamentally different from satellite detectors in that the primary photon is not detected directly. Instead, these detectors take advantage of the interaction of the gamma-rays photon with the Earth's atmosphere. Such collisions of high-energy photons produce particle cascades in the upper atmosphere. The energy of the incident particle is transferred to a burst of secondary particles, which propagates towards the ground. Discovered in 1938 by Pierre Auger, this burst of particle creation is termed an **extensive air shower** (EAS).

A very small fraction of air showers are produced by gamma rays; the rest are generated by cosmic ray protons and heavier nuclei which arrive isotropically from space. There are, however, characteristic differences between the gamma-ray-induced and cosmic-ray-induced showers, a factor which proves significant for discrimination purposes.

2.3.1 Gamma-ray-initiated Showers

As a high-energy gamma-ray photon enters the atmosphere and interacts, the dominant result is the production of an **electron-positron pair** ($e^{\pm}$) in the electric field of an atmospheric nucleus. If the energy is sufficient, the resulting electron and positron can then emit secondary gamma rays via **Bremsstrahlung**. In turn, these gamma rays can produce other $e^{\pm}$ pairs which can undergo further Bremsstrahlung interactions and so on, creating a particle avalanche. The result is a cascade of photons, electrons and positrons, as shown in Figure 2.3, travelling essentially in the original direction of the primary gamma ray. The shower particles spread laterally from the direction of the incident photon, forming a disk some metres thick, perpendicular to the incident photon direction.

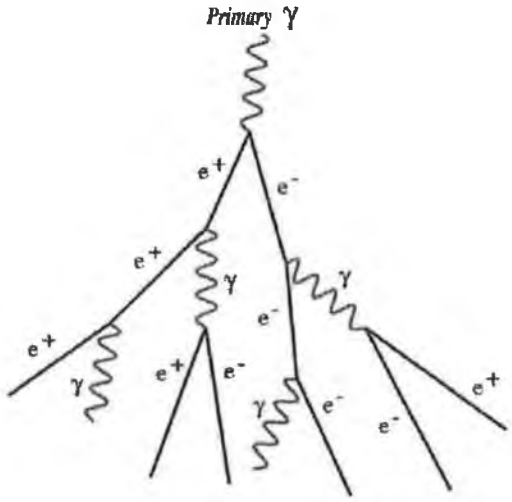

Figure 2.3: Formation of an extensive air shower (EAS) when a gamma-ray photon interacts in the upper atmosphere

The number of particles produced continues to increase progressively in the shower, almost exponentially, until the energy of the electrons and positrons drops below about 80 MeV; below this critical energy electrons and positrons lose their energy via atomic collisions and ionisation rather than by Bremsstrahlung. This effectively brings particle production to a halt and the number of particles decreases as the shower continues to propagate. The consequence is that, for an incident TeV gamma-ray photon, most of the particles exist for a short time at a height of 6-10 km, and the shower subsequently dies out below this.

2.3.2 Cosmic-ray-initiated Showers

The vast majority of air showers are initiated by cosmic rays, most of which are protons. When such a high-energy particle collides with an atmospheric nucleus (nitrogen or oxygen), part of the energy is converted into matter, with the creation of pions (π^0, π^+, π^-) and kaons (K^+, K^-). The fragments of the incident nucleus and the new particles formed travel through the atmosphere at high velocity, until another nuclear reaction takes place in which more particles are created and so on. The number of particles thus increases up to a depth at which the shower reaches the maximum development. This is the point at which the particles start to be absorbed by the atmosphere.

A primary proton of 10^{15} eV would produce a shower that reaches its maximum development at $\sim$ 6 km above sea level, with roughly a million particles created, of which perhaps one-third reach sea level.

The **neutral pions** (π^0) decay almost immediately into two γ-rays ($\pi^0 \rightarrow 2\gamma$, mean lifetime $\tau = 0.84 \times 10^{-16}$ s) which suffer the same processes as a primary gamma ray, creating an electromagnetic component of the shower. The charged pions and kaons may either collide with atmospheric nuclei producing new particles, or they may decay. For example, the charged pion decays into a **muon** and a **neutrino**: $\pi^{\pm} \rightarrow \mu^{\pm} + \nu_{\mu}$ ($\tau \simeq 2.6 \times 10^{-8}$ s). The muon, in turn, can decay into an electron and two neutrinos: $\mu^{\pm} \rightarrow e^{\pm} + \nu_e + \nu_{\mu}$ ($\tau \simeq 2.2 \times 10^{-6}$ s).

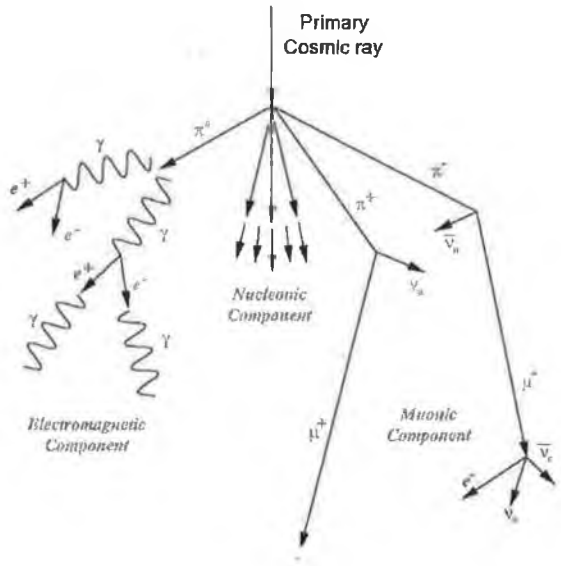

Figure 2.4: A cosmic-ray-initiated particle shower.

Since their velocities are very close to the speed of light, the muons are affected by time dilation and so in spite of their short lifetime, many muons can reach the ground without disintegrating. Hence, in most of the atmospheric showers a significant fraction of the muons produced can reach the ground, and even penetrate hundred of meters underground. The neutrinos produced in the disintegration of pions and muons have a very small probability of interaction with matter and many in fact pass right through the Earth.

2.3.3 Cherenkov Emission

During their brief existence, the thousands of secondary particles in the shower still have a very large energy, inherited from the primary gamma-ray photon or cosmic ray particle. As a result the particles propagate through the air with speed close to the speed of light in vacuum, and in doing so give rise to **Cherenkov radiation**. This radiation is not emitted by the particle itself, as in the case of Bremsstrahlung, but by the local medium.

As a charged particle moves through a dielectric medium (such as air) with

refractive index n, it induces transient electric dipoles in the medium. If the velocity of the particle is higher than the local speed of light in the medium (c/n), there will be no dipoles created in the region ahead of the moving particle. The particle is essentially travelling faster than its own electromagnetic field. This effect produces the equivalent of a sonic boom with the high-speed particles polarising the surrounding gas. These polarised gas molecules consequently radiate brief electromagnetic pulses in the UV/visible region of the spectrum; when these pulses are in phase a coherent wavefront will form. This is the phenomenon of **Cherenkov radiation**.

The emission of Cherenkov light by the EAS is of great importance to gamma-ray astronomy. A primary gamma-ray photon and the ensuing cascade may die out in the upper atmosphere but the Cherenkov light produced in the shower can penetrate to ground level. The Cherenkov light from a shower initiated by a single cosmic gamma-ray photon of energy 1 TeV comes from a median altitude of about 10 km above sea level, and is beamed into a very small angle (typically less than 1° at the height where these particles are generated) illuminating an area on the ground several hundred metres in diameter. This yields an effective detection area in the region of 5×10^4 m^2. The Cherenkov light carries information pertaining to the point of the origin of the primary gamma ray on the celestial sphere, and also to the energy of the primary particle.

Simulations of air showers show that the pulses of Cherenkov light collected from gamma-ray primaries differ from those produced by cosmic ray primaries in fundamental ways. The Cherenkov images shown in Figure 2.5 illustrate the different characteristics of gamma-ray and cosmic ray events, as well as emission from single muons. When a Cherenkov telescope is tracking a VHE gamma-ray source, the image of an EAS produced by a gamma ray arriving from the source direction will point towards the centre of the camera since the axis of the EAS will be orientated parallel to the optic axis of the telescope. Cosmic ray showers, however, arrive isotropically distributed, with the shower axis randomly

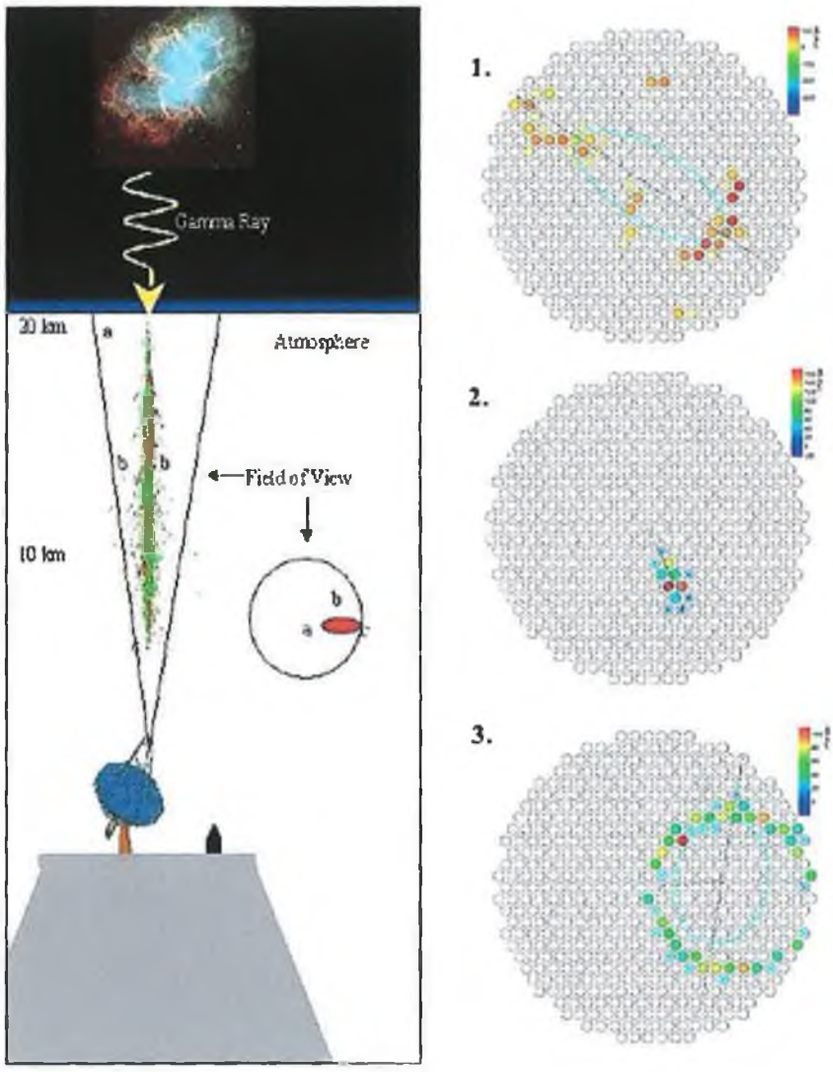

Figure 2.5: Sample events detected by the first VERITAS Telescope: 1. Proton event 2. Gamma-ray event 3. Local muon event.

orientated relative to the optic axis of the telescope.

Differences in the shape of Cherenkov images of EAS arise for physical reasons. Gamma-ray-initiated showers start higher up in the atmosphere and spread out less than cosmic ray showers, due to the smaller transverse momentum in electromagnetic interactions. These two effects produce images of gamma-ray-initiated air showers that are characteristically narrow and compact and which tend to have an elliptical shape aligned with the direction of the incoming photon. Conversely, cosmic-ray-induced air showers produce Cherenkov light images which are much broader and amorphous and less well aligned with the arrival direction.

The way in which these differences are exploited is by measuring the shape, size and orientation of each shower image, and selecting only those that are 'gamma-ray-like' in appearance. This **imaging technique** can remove most of the cosmic ray contamination, resulting in a much-improved ability to detect an excess number of counts from the source direction. The development of this technique led to the first verifiable detection of a TeV source at a high level of statistical significance, and consequently laid the foundation of modern VHE gamma-ray astronomy (Weekes 1989).

2.3.4 Imaging Cherenkov Telescopes

Imaging Atmospheric Cherenkov Telescopes (IACTs) have become the most sensitive technique for the observation of TeV gamma rays. Such detectors can directly record the images of Cherenkov light and can discriminate between electromagnetic and hadronic event with greater then 99.5% efficiency. The properties of Cherenkov telescopes include:

- small field of view, typically less than 5°,
- low duty cycle of only about 15%,
- angular resolution better than 1°,
- good energy resolution ($\Delta E/E$) of the order of 20%,

- a very large collection area for ground-based detectors, of the order of 5×10^4 m^2 compared with less then 1 m^2 for space-based detectors.

The typical IACT design consists of a large optical reflector and a camera placed in its focal plane. For economic reasons, the reflector surface is usually a tessellated structure composed of smaller mirrors; typically these are glass mirrors, anodised or with a quartz coating on the polished surface. The gross mirror profile may be parabolic for minimal time spread, while individual mirrors elements are spherical with a radius that gives the best image quality. The reflector of an imaging telescope must provide an optical resolution of better than 0.1° - 0.2° within a field of view of 2° - 3° in diameter.

The camera is the most important element of the telescope and is decisive for good gamma-ray sensitivity. The camera comprises an array of photomultiplier tubes (PMTs), accompanied by fast signal-processing electronics. The number of PMTs in a camera and in particular the angular size of each PMT determines the minimum angular resolution that the telescope can achieve. High sensitivity to single photons and the best possible time resolution are important. This is because the Cherenkov signal is weak and marginally detectable, and the effect of night sky brightness fluctuations can be minimised by using very short gate intervals. The telescope mirrors reflect the Cherenkov light from a EAS rather than directly imaging an astronomical source. The light is reflected onto the focal plane, where it is captured by the PMT camera. In this way, a Cherenkov light image of the EAS is recorded.

2.3.5 Cherenkov Wavefront Detectors

Solar power plants with their large number of heliostat mirrors can operate as TeV gamma-ray detectors by night. Focusing Cherenkov light onto individual PMTs from such massive mirror areas can in principle provide energy thresholds as low as 50 GeV. At typical operational energies, cosmic rays are much less efficient at producing Cherenkov light, which greatly reduces background. By

utilising the lateral distribution of light as a discriminant, detection of a gamma-ray signal is possible, while estimation of the primary photon energy is in theory more accurate due to multiple sampling of the Cherenkov light pool. However, the small field of view of these experiments make them unsuitable for observations of extended sources, and the complex focal plane instrumentation and often poor quality mirrors render this technique problematic.

The STACEE and CELESTE wavefront experiments have detected both the Crab Nebula and the AGN Markarian 421 (Boone & the STACEE Collaboration 2002; Holder & the Celeste Collaboration 2001).

2.3.6 Extensive Air Shower Detectors

In the energy region above about 10 TeV, a gamma-ray air shower is sufficiently energetic that a significant number of shower electrons can penetrate the atmosphere and reach the ground. At ground level the shower front may extend to several hundred metres, allowing the event to be detected by an array of particle detectors of modest size spread over a sufficient fraction of this area. The thin shower front reaching the ground has a large radius of curvature, so the relative arrival times at different detectors can be used to determine the arrival direction of the primary with an accuracy typically of the order of 1°. The density of electrons at the detectors can be used as an estimate of the primary energy. However, this is susceptible to variations in the height of shower maximum from shower to shower.

A more reliable estimate can be obtained by the use of a water-Cherenkov detector. Particles entering the detector travel at a velocity exceeding the phase velocity of light in water and emit Cherenkov radiation. A series of PMTs, strategically placed around the water pool, provide a snapshot of the shower front based on Cherenkov emission of the particles. To distinguish between shower types a double-level array of PMTs is used; the top level detects emission by the shower front while the bottom level detects emission from a highly-penetrating

population of muons. Since cosmic ray showers are muon-rich and gamma-ray showers are muon-deficient, any shower identified as containing muons can be rejected as background. The direction of the primary gamma ray or cosmic ray is reconstructed using the relative times at where different counters are hit. Shower fluctuations usually limit the angular resolution of EAS arrays to about 0.5°.

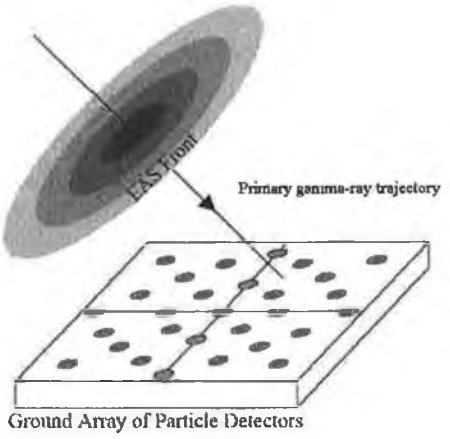

Figure 2.6: A schematic of an extensive air shower detector.

EAS arrays can operate 24 hours a day and in all weather conditions. They can also observe all sources in the overhead sky simultaneously. However, because EAS arrays typically cover only a small fraction of the ground with detectors, they have a high energy threshold and limited background rejection capabilities.

The **TIBET** array of scintillator detectors, with its high-altitude location, has measured the Crab Nebula spectrum above 3 TeV (Amenomori et al. 1999). The **Milagro** detector, located near Los Alamos New Mexico, comprises a 5×10^4 m^3 volume of water observed by 70 PMTs, operates at an energy threshold > 3 TeV. This experiment has also detected the Crab Nebula (Atkins et al. 2004). Both arrays have also detected emission from the active galaxy Markarian 421.

2.3.7 Air Fluorescence Detectors

Extensive air showers that are spread over a very large area can be detected by the UV and visible scintillation light emitted by nitrogen molecules in the vicinity of the shower. The light tracks are imaged by telescopes with cameras composed of PMTs. This method has been used by the Fly's Eye experiment (Matthews et al. 1991), and by the later **HiRes** version, to search for gamma rays above 200 TeV. The Auger project also operates fluorescence detectors in parallel to its extensive array of particle detectors.

2.4 Present Status and Outlook

The imaging Cherenkov telescope has proved the most effective of the ground-based detectors and presently five such IACT experiments are in operation worldwide: the Whipple 10-metre telescope, the MAGIC 17-metre telescope, and the H.E.S.S., VERITAS and CANGAROO III telescope arrays. The capabilities, as well as the scientific goals, of these instruments overlap; however they are physically located in different parts of the world and not in direct competition with each other. H.E.S.S. and CANGAROO cover the southern hemisphere, while MAGIC, VERITAS and Whipple observe the northern hemisphere.

The new gamma-ray detectors now coming on-line have been designed with improved flux sensitivity over the GeV-TeV energy range and lower energy thresholds. Observations at lower energies allow for potential detection of new sources and increased spectral coverage of existing sources. There will also be overlap with the energy range accessible to upcoming satellite-based experiments. An increase in sensitivity can be achieved by increasing the number of gamma-rays collected and by improving the discrimination against background events.

It is the design of the instrument itself that contributes, in the largest degree, to the elimination of background events. An instrument that is designed to take advantage of the inherent differences between signal events and background

events can achieve good intrinsic discrimination by its very nature. Two such experimental designs currently expanding the gamma-ray horizon are large-area detectors and detector arrays.

2.4.1 Large Area Detectors

A larger light collection area increases the number of gamma-ray events detected. The ideal collection area is comparable to the size of the Cherenkov light pool on the ground. The amount of light recorded from an air shower increases more quickly with mirror area ($\propto A$) than the fluctuations in the background light recorded from the night sky ($\propto \sqrt{A}$), the principal background determining the triggering threshold. Collecting more light allows this threshold to be lowered and hence lower energy events can be recorded.

Among the third generation of imaging Cherenkov telescopes is one such large area detector. The fully steerable 17-metre MAGIC telescope, operating at La Palma, has a 234 m^2 mirror area. MAGIC utilises many elements previously untried in atmospheric Cherenkov telescopes, including a lightweight carbon-fibre frame for mirror support, a finely-pixellated camera using advanced hemispherical PMTs, and a 300 MHz flash analog-to-digital-converter system. With an energy threshold approaching 50 GeV, MAGIC will be able to study distant AGN out to a redshift of 2 - 3, while its rapid slew time makes is intended for observing gamma-ray bursts. MAGIC is already operational and has observed the Crab Nebula at the 10σ level in less than one hour and the AGN Markarian 421 at 23σ in 100 minutes (Bock & the MAGIC Collaboration 2005).

2.4.2 Detector Arrays

An array of multiple telescopes can view an air shower stereoscopically from different points on the ground while lying within the Cherenkov pool. Upon combining the multiple images of an event, the gamma-ray events will produce a very different signal from cosmic-ray events. Moreover the array can be triggered in a fash-

ion that eliminates local muon events and reduces accidental night-sky triggers. The additional information gained by stereoscopic observations of air showers improves the energy reconstruction of gamma-ray showers and provides enhanced differentiation between gamma-ray and cosmic ray primaries. The HEGRA experiment, which operated with an array of small aperture telescopes, pioneered the technique and successfully achieved stereoscopic imaging with IACTs (Konopelko et al. 1999).

The new Cherenkov telescope arrays now operational or coming on-line include:

- **VERITAS**: A system of seven 12-metre telescopes in southern Arizona, which will be the largest array in the northern hemisphere. Based on the design of the Whipple 10-metre telescope, all detectors are identical and employ a Davies-Cotton reflector with a 499 PMT camera located in the focal plane. The array will incorporate a number of innovative technologies, most notably a 500 MHz flash analog-to-digital converter system to minimise dead-time. The first telescope has been online since early 2005 and has seen successful operation; the VERITAS four-telescope array is expected to be operational by late 2006. Designed to be flexible, with operation possible as a single detector or a number of sub-arrays, VERITAS will offer a unique opportunity for in-depth studies of AGN, SNRs and GRBs in the 100 GeV to 10 TeV range and with appreciable sensitivity above and below this range. For a full review of the VERITAS project see Weekes et al. (2002).

- **H.E.S.S.**: The H.E.S.S. Collaboration is a joint German-French-British effort, and includes former members of the HEGRA and CAT collaborations. The telescopes are Davies-Cotton design, with an f-number of 1.25, and a focal plane camera comprising 960 pixels (Bernlöhr 2001). H.E.S.S. is currently operating with a four-element array located in Namibia and has detected the Crab Nebula at the 20σ level in 4.7 hours Hinton (2004). A

number of new sources have also been detected (Hofmann 2005).

- **CANGAROO III**: This array is a continuation of the successful Australian-Japanese CANGAROO group. The array comprises four telescopes arranged in a diamond pattern, with inter-telescope spacing $\sim$100 metres (Enomoto et al. 2002). In contrast to the VERITAS and HE.S.S. reflectors, CANGAROO-III utilises a parabolic mirror design, while the focal plane camera is made up of 427 pixels.

The increased background rejection, especially of the cosmic ray muon component, improves the low-energy sensitivity of these array systems, and a 50 GeV threshold may be achievable. The GLAST satellite, to be launched in 2007, will cover the energy from 0.01-100 GeV. The combination of space-based and ground-based detectors will allow simultaneous measurements of spectra over six complete decades in energy. With their improved sensitivities and lower thresholds (Table 2.2), the next-generation VHE instruments will result in the detection of new sources, and should help solve many of the current questions in high-energy gamma-ray astrophysics.

Group	Site	Operating Period	Type	E_{thres} / TeV
CANGAROO	Woomera, Australia	2004→	IACT ×4	0.1
CAT	French Pyrenees	1996-01	IACT	0.25
CELESTE	French Pyrenes	1995-04	WFS	0.03
Crimea	Crimea	1975→	IACT ×2	1.0
Durham Mark6	Narrabi, Australia	1995-00	IACT	0.25
HEGRA CT1	La Palma, Spain	1992-02	IACT	0.5
HEGRA	La Palma, Spain	1998-02	IACT ×5	0.5
H.E.S.S.	Namibia, South Africa	2004→	IACT ×4	0.1
MAGIC	La Palma, Spain	2004→	IACT	0.05
Milagro	New Mexico, USA	2000 →	PDA	1
STACEE	New Mexico, USA	1995→	WFS	0.14
Telescope Array	Utah, USA	1996-00	IACT ×7	0.6
Tibet	Tibet	2000→	PDA	> 3
VERITAS	Arizona, USA	2005→	IACT ×1→7	0.1
Whipple 10m	Arizona, USA	1967→	IACT	0.3

Table 2.2: A summary of ground-based gamma-ray detectors with their relevant specifications. The telescope arrays are shown with their array size, e.g., IACT ×4.

Chapter 3

The Whipple 10-metre IACT

3.1 Introduction

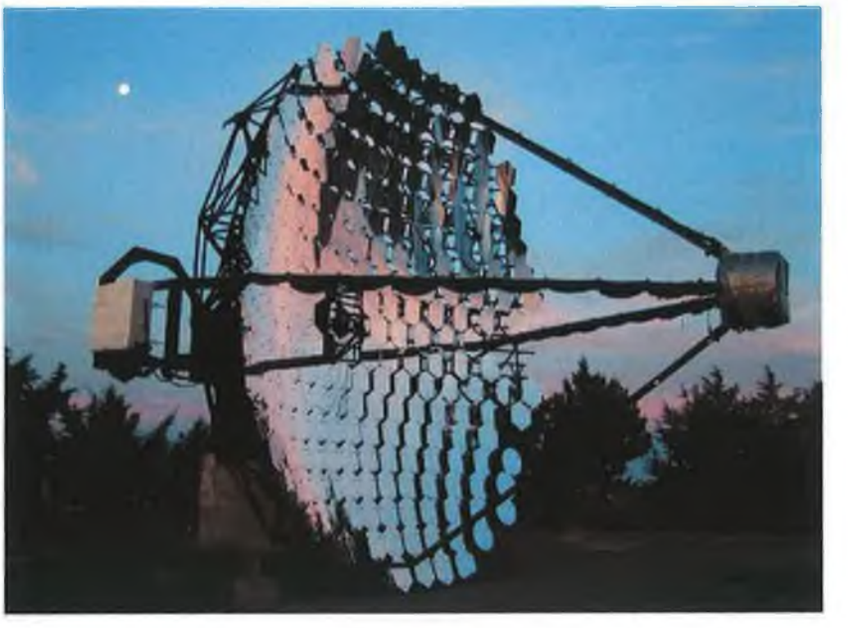

Figure 3.1: The Whipple 10-metre telescope, operated by the VERITAS collaboration on Mt. Hopkins in southern Arizona.

The **Fred Lawrence Whipple Observatory** is located at **Mt. Hopkins** in southern Arizona. At an altitude of 2.3 km above sea level, the observatory is home to several telescopes including the large MMT system as well as the

Whipple gamma-ray telescope. This 10-metre optical reflector was purpose-built in 1968 for gamma-ray astronomy by the Smithsonian Astrophysical Observatory. It is operated by the **VERITAS** Collaboration. Since its inception, numerous modifications have being made to improve the sensitivity and performance of the overall instrument. Throughout the last three decades, the telescope has been used to pioneer the Atmospheric Cherenkov Imaging technique and has been responsible for many key developments in the field, including the first definite TeV detection of the Crab Nebula in 1988 (Weekes 1989). This was the first detection of a steady VHE source at a high level of statistical significance. The steady nature of the emission meant that the Crab could be used as a '**standard candle**' by which VHE telescopes would be able to test their capabilities, and consequently this marked the beginning of a new era in VHE astronomy.

3.2 Optical Reflector

The telescope is a Davies & Cotton (1957) design and consists of a spherical frame supporting a 10-metre diameter tessellated mirror with a detector at the focal point. See Figure 3.1 and Table 3.1.

The spherically curved frame or **Optical Support Structure** (OSS) is a tubular metal structure and is mounted on two motorised drives, giving movement in altitude and azimuth. The OSS having a radius of curvature of 7.3 m and holds the reflecting surface comprising 248 hexagonal mirror facets.

All facets are identical, each having a hexagonal face measuring 61 cm from edge to edge. They are aluminised on the front surface, covered with a protective quartz coating to enhance their response to ultraviolet/blue light and anodised to protect them from weathering. The facets have a radius of curvature twice that of the optical support structure (i.e. 14.6 m), and their axes are aligned as to converge at the center of curvature. The result of this is considerably reduced spherical aberration.

The detector or camera is housed at the focal plane, at a distance of 7.3 m from

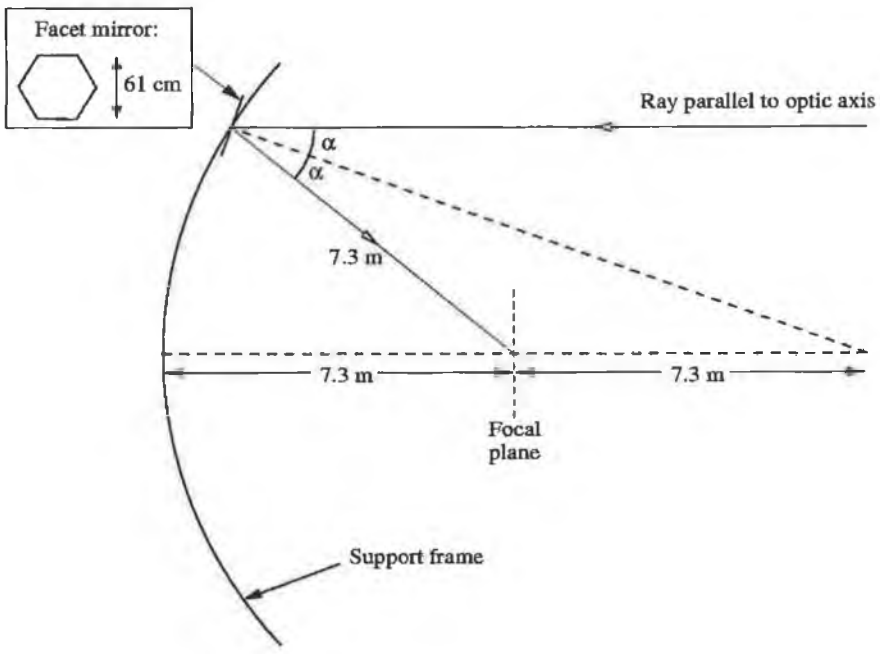

Figure 3.2: The reflector setup for the Whipple telescope.

the reflector dish, yielding a $f/0.73$ telescope. The telescope has a **point-spread function** of $0.11°$.

The Davies-Cotton design was chosen for the Whipple telescope due to its advantages over more traditional telescope designs. Firstly, all the mirror facets are identical, allowing them to be produced rather inexpensively. Secondly, the alignment of the individual mirror facets is relatively straightforward. Finally the Davies-Cotton plan has superior off-axis imaging capabilities compared to the more traditional parabolic telescope designs. This attribute allows better imaging, due to the extended nature of the air showers produced by gamma rays, and increased field of view for the telescope. This spherical design does have a drawback in that the system is not **isochronous** i.e. there is a time difference from light arriving from different parts of the mirror. Light reflecting from the outer facets reaches the camera approximately 6 ns earlier than the light reflected from mirrors in the inner part of the reflector.

Attribute	Value
Opening Diameter	10 m
Focal Length	7.3 m
No. of Mirror Facets	248
Energy Threshold	400 GeV
Energy Resolution	35%
Angular Resolution	0.11°
Pointing Resolution	0.01°
Field of view (FOV)	5°
Crab Sensitivity	5.5 $\sigma/\sqrt{hr}$
Spectral Sensitivity	160-660 nm

Table 3.1: The operational parameters of the Whipple 10-metre telescope

3.3 Detector Design

Ultra-high-speed detection is required to capture the extremely brief Cherenkov signals, which typically last less then 5 nanoseconds. The Cherenkov flashes are detected by an array of photomultiplier tubes (**PMTs**) and very fast electronics, allowing exposure times of the order of 10 nanoseconds in practice. Exposures of such brevity assist in suppressing the effect of the fluctuating night sky. The PMTs are of high quantum efficiency, closely packed in a hexagonal arrangement at the focal plane of the reflector. This camera has been upgraded several times over the last twenty years, with improvements in the angular resolution and field of view (Finley et al. 2000).

The observations in this thesis were carried out using the camera configuration of the year 1999+, which comprised 490 PMTs (see Figure 3.3). Hamamatsu R1398 PMTs are used, which give a fast response (2 ns rise time) and high **quantum efficiency** (~20%) for blue-UV light, the spectrum region in which the Cherenkov radiation from the EAS peaks. There are 379 inner pixels, having an angular size of 0.12°, which are half the size of the 111 outer tubes. The outer tubes were used primarily to test fibre-optic communications before their removal during 2003 and are not included in the telescope trigger or in the analysis.

Light cones are placed over the inner tubes to recover light falling in the

dead space between them and to eliminate extraneous light. The active photocathode occupies only 35% of the total area of each PMT. The remaining space is occupied by mu-metal shielding and plastic casing. The purpose of this shielding is to prevent deflection of the photoelectrons by the Earth's magnetic field.

Figure 3.3: The Whipple camera with 490 photomultiplier tubes.

3.3.1 High Voltage System

The voltage supply to the camera is provided by three LeCroy high voltage (**HV**) modules. These HV units are housed in crates mounted on the telescope counterweights. The HV supply is monitored and controlled via ethernet and custom software. Manual HV control is also present in case of emergency. The PMT anode currents are displayed on a colour-coded graphical user interface (GUI) in the control room. This screen is continually updated, displaying the currents as a corresponding colour as well as a numerical form. PMTs are shown in red if their currents are excessive. The main cause of excessively high current levels is the

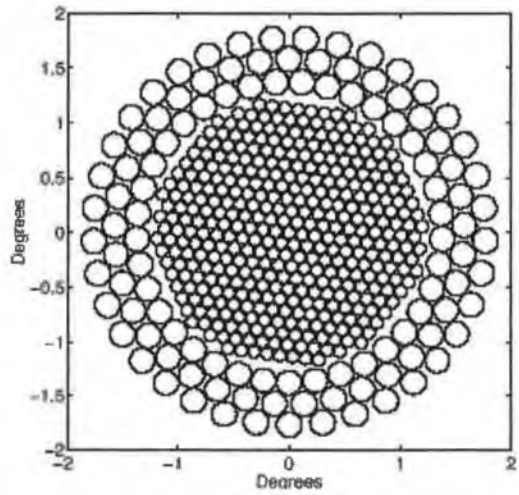

Figure 3.4: An angular map of the PMTs comprising the camera

passage of bright stars across the field of view. Light from a star may typically cause a high current in one PMT, though for very bright stars, a fraction of the light may fall on its neighbours. If the light level is too high, the affected PMTs are switched off to avoid non-linear response and photocathode damage. For fainter stars this is not necessary, though the affected PMTs have higher noise levels due to the greater fluctuations on the background light level.

3.4 Telescope Drive

Control of the telescope azimuth and elevation drive motors is by a dedicated computer, and the position is monitored and fed back via Heidenhein 16-bit position encoders. The equatorial coordinates of the object (right ascension and declination) to be tracked are entered into the tracking computer which calculates the altitude and azimuth for the current time. Approximately every five seconds, the tracking information is transferred to the main data acquisition computer by ftp link. The control program continually adjusts the motor speed to compensate for any deviations from the calculated path. The drive motors can also be operated via manual controls, which are mainly used when stowing the telescope or

for high-speed slewing when a large azimuth angle must be traversed to reach a target object.

3.5 CCD Monitoring

The star field viewed by the reflector is monitored with a CCD camera mounted on one of the side arms of the telescope, pointing directly at the sky. The ST-237 CCD camera used is coupled with a $f/0.85$ lens to give a field of view of $10.8° \times 8.2°$. Stars down to 8th magnitude can be detected with a 5 second integration time. The camera is linked to a control computer by 50 m of RG58 cable. An image is taken approximately every 40 seconds and the digitised image is sent to the computer where it is displayed on a monitor. The positions and intensities of up to 100 stars per image are determined by the computer and transferred by ftp link to the main acquisition computer for inclusion in the data stream. The CCD images can provide information about the sky clarity, telescope pointing accuracy and bright stars which may lead to increased noise levels.

3.6 FIR Pyrometer

A far-infrared (FIR) pyrometer is housed with the CCD camera, and provides a measurement of the average night sky temperature within its 2.8° FOV. The pyrometer effectively acts as a **cloud detector**.

Clouds passing within the FOV produce an increase in the reported pyrometer temperature. This temperature increase is proportional to the height, thickness and water content of the cloud. With no cloud present, the temperature decreases to the quiescent level, which is almost entirely dependent upon the water vapour content in the atmosphere above the detector.

Cloud represents a great hindrance to the propagation of Cherenkov light, and as such it is the predominant cause of low event rates and thus low quality observations. A clear correlation can be seen from Figure 3.5, where cloud cover

has sharply diminished the detected event rate between 300 seconds and 900 seconds.

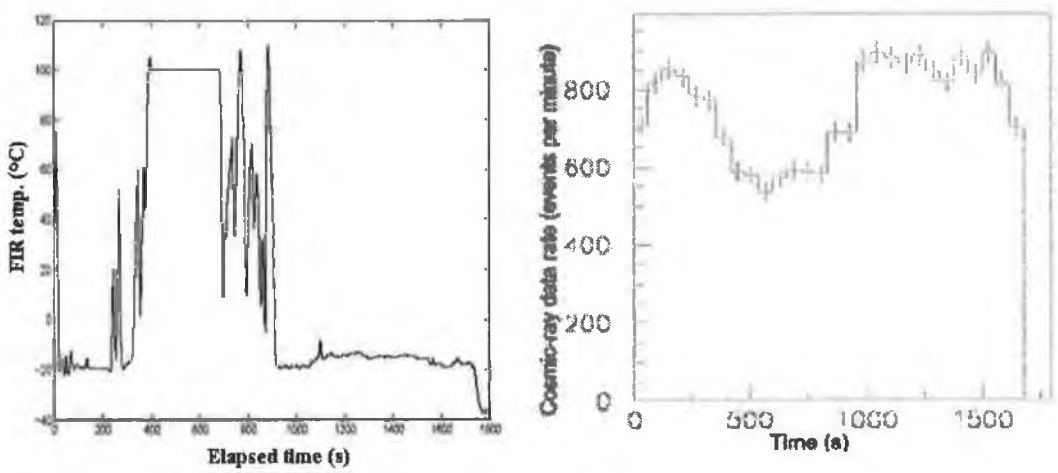

Figure 3.5: Correlation between FIR temperature and cosmic ray rate recorded contemporaneously with the Whipple 10-metre telescope (from Dowdall (2003)).

3.7 Data Acquisition (DAQ)

A building adjacent to the telescope houses all the control and data systems. The acquisition electronics consist of amplifiers, discriminators, analogue-to-digital converter and scalers for each camera pixel. The photomultiplier signals are transmitted to the control building using coaxial cable for the inner channels and by fibre-optic cable for the outer channels. Only the innermost 331 channels form part of the trigger; this is a legacy from a previous camera configuration. The signals for each PMT is passed through a amplifier with gain of ten. The amplifier has three outputs - analogue-to-digital converter (ADC), constant fraction discriminator (CFD) and the current monitor.

Absolute timing for Whipple telescope data is provided by a GPS receiver. The GPS clock allows the absolute UTC time of each event to be stored; a 1 MHz oscillator provides an independent check of relative event times.

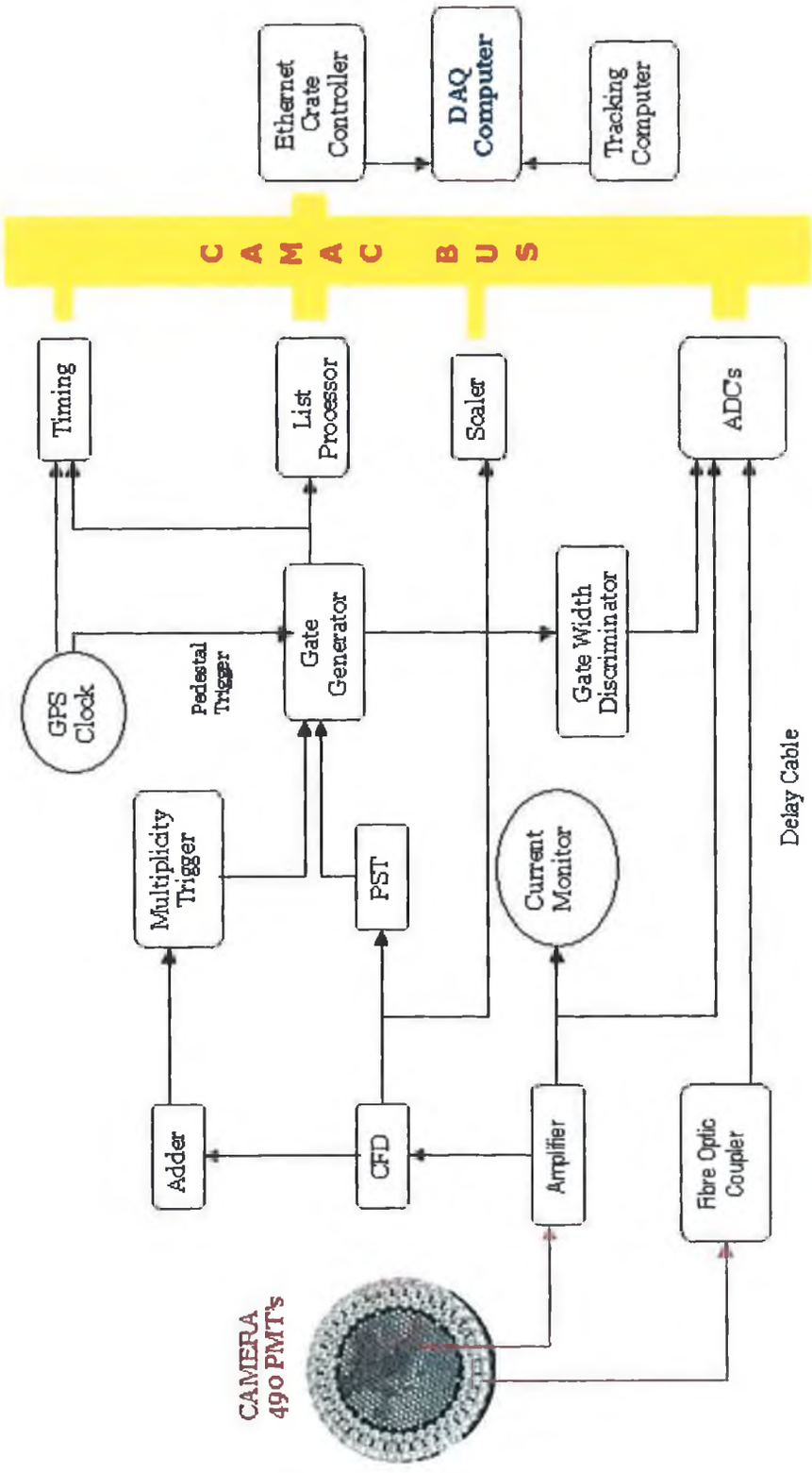

Figure 3.6: Data acquisition (DAQ) system for the Whipple 10-metre telescope.

3.7.1 Analogue to Digital Converters

The ADC integrates the analogue charge from the entire photoelectron pulse of a PMT and translates this into a digital signal, quoted in digital counts (d.c.) (see Figure 3.7). A single photoelectron pulse from the output of a PMT has a rise time of 1-2 ns and a fall time of 6-10 ns. A PMT pulse due to a Cherenkov event is the sum of all the single photoelectron pulses and typically has a rise time of 3-5 ns and a fall of 15-20 ns. After travelling from the telescope to the electronics, this has been broadened further to 4-6 ns rise time and 15-25 ns fall time. Thus, to record the entire pulse the ADC gate width is set to 30 ns. Once the event gate closes, a list processor reads the ADC values and other event information to its buffer.

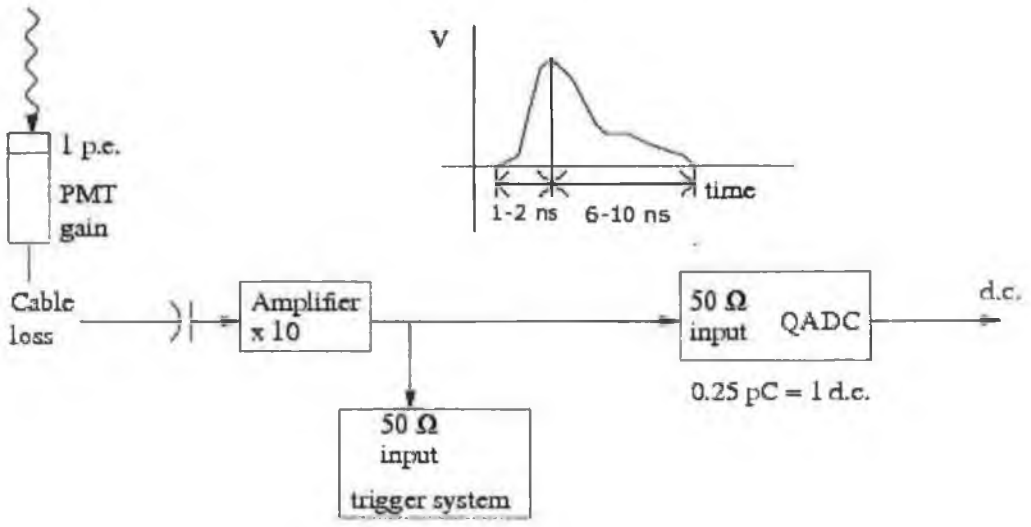

Figure 3.7: Conversion of a single photoelectron (p.e.) to digital count (d.c.) output.

Before digital conversion can occur the signal must be deemed as being part of an event. This is the process of **discrimination**, carried out by the CFD, multiplicity and pattern trigger systems. Each of the inner 331 channels is fed to a constant fraction discriminator, the first stage of the trigger.

3.7.2 Constant Fraction Discriminators (CFDs)

The Whipple DAQ uses CFDs to determine whether a channel has triggered. These discriminators take the amplified PMT signals as their input and output a pulse of preset amplitude and duration when their input signal rises above a preset threshold (35 mV). The timing of the leading edge of the output signal is determined using a constant fraction of the input signal, giving a more accurate synchronisation of signal and trigger pulse than a standard fixed-threshold discriminator. This enables the width of the ADC gate to be reduced, thus improving the signal-to-noise ratio.

3.7.3 The Pattern Selection and Multiplicity Triggers

The pattern selection trigger (PST) was designed and implemented by the Leeds Whipple group (Bradbury 1997). The PST examines overlapping patches of 19 pixels in the camera and deduces whether any of the PMTs above threshold are adjacent to each other. This suppresses random triggers from night sky noise or PMT after-pulsing, and allows the electronics to run at a lower energy threshold whilst maintaining a manageable data rate. The PST is currently set to trigger only when 3 or more adjacent pixels out of the innermost 331 pixels exceed the threshold. This has the effect of biasing the camera in favour of real air shower events and against random fluctuations due to background noise. Thus the accidental trigger rate is significantly reduced, allowing the system to operate at a lower CFD threshold while maintaining an acceptable trigger rate.

A multiplicity trigger is generated whenever a preset number of tubes pass the CFD threshold. The preset number is called the multiplicity. The Whipple telescope uses a **3-fold multiplicity**.

The Whipple telescope now operates with both triggers in effect at a CFD threshold of 35 mV, so that event must pass both the pattern and multiplicity triggers to be recorded. This trigger information will then arrive at the ADCs at the same time as the amplified signal, which was transmitted via a delay cable.

The ADCs integrate the charge over a 30 ns gate starting from the time of the trigger. The GPS clock allows each event to be time stamped with it absolute UTC value. The event is then digitised and transferred to the **Data Acquisition Computer**.

One output from each CFD is fed into a **singles-rate scaler**, which counts the number of times individual channels have triggered. This information is used to diagnose problems with the triggering of specific tubes. The singles-rate scalers are only read during a pedestal-triggered event.

3.7.4 Pedestal Trigger

A GPS clock triggers the data acquisition electronics to record the PMT signals in the absence of an actual Cherenkov event. This data is used both for calibration and for examining system performance. These pedestal events are injected once a second and are tagged to distinguish them from real events. For each phototube, the average ADC count for these pedestal events is used as a measure of the light from the night sky. The variance of this average level is also calculated for each ADC. A very high or low variance for a channel can be suggestive of a problem.

3.7.5 Data Readout and Storage

When a Cherenkov event has passed the discriminators, the ADCs are then read. The ADC output is initially fed to a list processor, a computer with a large memory buffer to store data until received by the DAQ computer. This DAQ computer controls the storage of data for each observational run. It also initialises the CFD and PST modules with their settings, monitors the data rate and coordinates the run start time with the tracking computer. During the observation run some events are displayed on screen with event-rate plots and other diagnostic information.

The data are stored in Fortran records which are then interfaced via the data acquisition software to the Zebra data storage system developed at CERN. This

allows the data to be written to Zebra (.fz) files, which provide data compression, flexibility in the information stored and full portability between different operating systems (provided the host computers have access to the CERN software libraries). The entire set of data for each run is then stored on hard disk awaiting analysis. The analysis is discussed in detail in Chapter 5.

3.8 Observing Methodology

3.8.1 Observing Schedule

The schedule for telescope observations is primarily dictated by the local weather conditions, and the cycles of the Sun and Moon. Clear, dark, settled skies are the usual requirement. Conditions such as high wind speeds (i.e., above 50 km/hr) or lightning can damage the telescope; for example, no observations are made during the summer months when electrical storms are frequent.

The observing season usually starts in September and runs to the following June. This is subdivided into a number of 'dark runs' each lasting approximately three weeks, defined by the orbital cycle of the moon. The increase in the night sky light caused by the presence of the Moon means that for about 5 - 10 days around the time of the full Moon, no observation takes place. Useful observations cannot be made if there is a significant amount of cloud in the sky, since the Cherenkov light, emitted above the cloud level, would be absorbed. These tight observing conditions typically yield an average duty cycle of $\sim$10%.

A typical night's operation focuses on observing a list of target sources, e.g., blazars, SNRs etc. There are two main modes of observations, ON/OFF pair mode and tracking mode.

3.8.2 ON/OFF Mode

An ON-run and an OFF-run are taken in succession. For the ON-run, the telescope is pointed at a specified celestial location (in right ascension and declina-

tion). This may be a previously confirmed TeV source or a potential source. The telescope then tracks this position for approximately twenty-eight minutes as the elevation and azimuth angles of the source change. At the end of the ON-run, the telescope is instructed to slew to right ascension 30 minutes less than that of the source but at the same declination. This corresponds to the same elevation and azimuth as at the beginning of the ON-run (allowing 2 minutes for the telescope to slew to its new position). The new right ascension position is then tracked for 28 minutes (OFF-run), covering the same elevation and azimuth path (i.e. the same part of the sky) as followed by the source during the ON-run. In some cases the OFF-run may be taken before the ON-run, at a right ascension 30 minutes greater than that of the source; this may be done to avoid an OFF-region where there are many bright stars, or to facilitate observations of a source as it rises.

The OFF data can then be used to estimate the background signal that is present in the ON-run. Subsequent filtering and analysis techniques are employed to remove systematically the effects of this background from the ON-run data. The gamma-ray signal, if present, will be weak; over 99% of the events recorded are typically due to cosmic rays and local muons.

3.8.3 Tracking Mode

A tracking run is effectively an ON-run recorded without a corresponding OFF-run immediately before or after it. This tracking mode allows continuous observation, so several runs may be taken in succession without the interruption of a control run.

This mode is useful when searching for potential VHE sources, since a qualitative indication of gamma-ray output can be obtained in a relatively short time. Furthermore, since uninterrupted observations of a source can be made, the tracking mode is useful when studying rapidly varying phenomena, such as the flaring activity of the AGN Markarian 421 and Markarian 501, where ON/OFF observations might cause important time-profile information to be lost. Tracking

observations are also taken when the night-sky conditions are deemed by the observers to be poor. For example, clouds in the field of view are noticeable from fluctuations in the cosmic ray rate. An OFF-run is not useful since it is known that the background rate is varying.

Data to act as a control can be derived from the ON-source data in conjunction with control data recorded for other sources. All events which do not originate from the source direction are deemed to be background events. These events will be orientated randomly, and will not point towards the center of the camera. The orientation is described by **alpha** (α), the angle between the major axis of the image and a line joining the image centroid to the centre of the camera (see Figure 5.1). The ratio of the number of events in the α = 0°-15° band (N_{0-15}) to the number of events in the α = 20°-65° band (N_{20-65}) in a large number of OFF-runs yields a **tracking ratio** R_{trk} (Equation 3.2). So in the absence of an OFF-run, the events in the 20°-65° region of an ON-source alpha plot ($N_{ON}(20° - 65°)$) can be used to estimate the background N_{OFF} from the source direction, i.e. from α = 0°-15°, using

$$N_{OFF} = N_{ON}(20° - 65°) \times R_{trk} \tag{3.1}$$

The tracking ratio and its associated statistical error are given by:

$$R_{trk} \pm \Delta R_{trk} = \frac{N_{0-15}}{N_{20-65}} \pm \sqrt{\frac{N_{0-15}}{N_{20-65}^2} + \frac{N_{0-15}^2}{N_{20-65}}} \tag{3.2}$$

The uncertainty in the OFF-source event rate is correlated with the stability of R_{trk} for different sky-brightness fields and over the course of the observing season. It has been shown that an instability in the tracking ratio throughout a season becomes amplified when applied to large data sets (Quinn et al. 2001). Small differences between regions of the sky can have an adverse effect on the signal estimation. To avoid these difficulties an alternative approach, the matched pair analysis, was employed in the analysis contained in this thesis (see Section 5.4).

3.8.4 Calibration and Diagnostic Data

At the beginning of each night, data are taken for calibration and diagnostic purposes.

- **Nitrogen run**: In analysing the Cherenkov events it is necessary to have contemporary data describing the different characteristics of each of the camera pixels. This is because the individual PMTs that make up the camera differ slightly in performance. That is, the gain for one PMT will not necessarily be equal to that of another, even for the same model, leading to non-uniform response across the field of view. To overcome this problem a "nitrogen run" is used to 'flat-field' the camera. This run is typically a one-minute exposure of uniform flashes from a nitrogen discharge lamp, positioned at the center of the reflector. This lamp shines an equal amount of light on each PMT, providing a signal which may be used to correct for slight differences in their behaviour. Thus, the relative gain of each PMT is determined for a given night. These results are then applied to other data taken on the same night to remove the effect of the different gains inherent in each PMT.

- **Zenith run**: A ten-minute data run is usually recorded with the telescope aimed at an elevation close to the zenith (typically 86°). This data allows for the determinations of relative throughput or transparency for the night sky, as well as checking overall system performance.

- **Pointing check**: The pointing accuracy of the telescope is checked nightly. This is achieved by aiming at a bright star, close to the candidate object, and noting the effect on the currents in the central PMTs.

While the telescope is tracking a candidate source the PMT current display is observed and the HV supply switched off for any PMT showing an excessive current. Since the telescope moves on an alt-azimuth mount, the stars in the field

of view rotate in the camera plane as the source is tracked across the sky. The movement of a bright star must therefore be anticipated by the observer so that PMTs can be switched off before the current becomes too great.

Chapter 4

Active Galactic Nuclei

4.1 Introduction

The radiation emitted from 'normal' galaxies is mainly produced by thermal processes. However, a minority of galaxies also produce a substantial amount of radiation from non-thermal processes such as synchrotron radiation, and exhibit luminosities thousands of times greater than those of normal galaxies. The enormous luminosity is typically produced from a very small volume located at the centre or nucleus. Hence, such objects are referred to as active galactic nuclei. The emission from AGN can cover the entire electromagnetic spectrum, from radio to gamma ray, extending over 20 orders of magnitude in frequency. AGN are generally characterised by high luminosity, non-thermal emission, rapidly-varying luminosity, broad emission lines, and jet-like protuberances.

Such objects represent a unique laboratory for the study of matter in extreme physical conditions. The AGN phenomenon could also shed light on the nature of galactic evolution and provide direct evidence for the existence of supermassive black holes.

4.2 Classification of AGN

Since their discovery, these bright distant objects have been classified in many ways. This is partly due to progressive development of the AGN model. The nomenclature of AGN (and by extension, their taxonomy) has evolved rather organically, and has not always remained consistent.

Many of the AGN initially discovered displayed a variety of properties that at first led them to be classified as separate astronomical phenomena. However, it is now believed that many of the differences may be due to the direction from which these objects are observed, their rate of fuelling and their stage of evolution (Dopita 1997). So it is that with increasing understanding, a more coherent classification scheme is being established.

A simplified classification of AGN can be made based on only two parameters, **radio-loudness** and **emission line widths**. Such a scenario is shown in Table 4.1. An active galaxy is considered radio-loud if its radio luminosity is at least 10 times greater than the optical luminosity. Roughly 85% of AGN occur in radio-quiet galaxies. The other main feature used in AGN classification is the presence or absence of emission lines. Such emissions are produced by the recombination of ions of various elements orbiting within the AGN. The widths of these emission lines are primarily due to the Doppler effect. AGN are then divided into broad-lined and narrow-lined objects. Some objects also exist with unusual emission-line properties, designated as **Type 0** objects. BL Lacertae objects (BL Lacs), for example, have very weak emission lines with typical equivalent widths of less than 0.5 nm.

4.2.1 Radio-quiet AGN

The radio-quiet galaxies can be subdivided into three classes. **Quasi-stellar objects** (QSOs) or 'quasars' reveal little of the host galaxy, which is not well resolved, leaving only the active nucleus visible. This originally caused these objects to be mistaken for stars, as their name implies.

Radio-Loudness	Type 2 (Narrow Line)	Type 1 (Broad Line)	Type 0 (Usual)
Radio-quiet:	Seyfert II	Seyfert I QSO	
Radio-loud:	NLRG { FR I FR II	BLRB SSRQ FSRQ	Blazars { BL Lacs (FSRQ)

decreasing angle to the line of sight $\rightarrow$

Table 4.1: A classification system for AGN, after Padovani (1997)

In **Seyfert galaxies**, the host galaxy is visible. Type I Seyferts generally exhibit both narrow and broad emission lines, as well as a strong non-stellar continuum. Type II Seyferts exhibit only narrow emission lines, and have a weaker non-stellar continuum. When the angle between the observer and the rotation axis is greater than $\sim 45°$, one is viewing a larger fraction of the light reflected from the surrounding torus. This accounts for the apparent difference between Seyfert I and Seyfert II galaxies. Radio-quiet galaxies are thus far not known to be strong gamma-ray emitters.

4.2.2 Radio-loud AGN

Type 2

The narrow-line radio galaxies (**NLRG**) are classified as Fanaroff-Riley I (**FR I**) or Fanaroff-Riley II (**FR II**) sources according to their radio morphology, which is connected with their radio power (Fanaroff & Riley 1974). FR I galaxies are generally less luminous than their FR II counterparts, and tend to have weaker optical emission as well. The radio emission of FR I galaxies is core-dominated, as opposed to the lobe-dominated emission regions of FR II galaxies.

Type 1

Radio-loud Type 1 AGN are broad-line radio galaxies (**BLRG**) and radio-strong quasars. Quasars are generally divided according to the value of their radio spectral index at a few GHz into steep-spectrum radio quasars (**SSRQ**) and flat-spectrum radio quasars (**FSRQ**). Flat-spectrum radio quasars are distinguished from steep-spectrum radio quasars primarily by the shape of their spectrum between 2.7 GHz and 5 GHz. FSRQs have a relatively flat spectrum in this range with spectral index $\alpha < 0.5$, while the indices for SSRQs are larger than 0.5. This distinction reflects the size of the radio-emitting region. In fact, radio emission in SSRQs is explained in terms of synchrotron radiation, which for extended regions has a relatively steep spectrum ($\alpha \sim 0.7$). On the other hand, emission from compact regions typically has a flatter spectrum, thought to be the result of the superposition of various self-absorbed components. The flat radio spectrum then indicates that nuclear emission dominates over the more extended emission, generally associated with the so-called **radio lobes**. Flat-spectrum quasars are generally core-dominated in the radio band, whereas SSRQs or narrow-line radio galaxies are both lobe-dominated. However, even though FSRQs have strong broad lines they are also included in the Type 0 column in Table 4.1 because their multi-frequency spectra are dominated by non-thermal emission as in BL Lac objects.

The broad-line radio-galaxies (**BLRGs**) could be local versions of radio quasars, where the host galaxy is detectable, as Seyfert I galaxies are local versions of QSO (see Padovani (1997)).

Type 0

Type 0 radio-loud sources have very weak emission lines and are known as **BL Lacertae** objects from the name of the class prototype which was originally thought to be a variable star in the constellation of Lacerta. BL Lacs share many of the same properties as their prototype, and generally exhibit highly-beamed

and variable emission.

BL Lacs can be subdivided into x-ray-selected (**XBL**) and radio-selected (**RBL**) BL Lacs, depending on the energy at which the peak synchrotron emission occurs. The XBL classification includes the TeV gamma-ray AGN, while most of the EGRET-identified sources are RBLs. XBLs are sometimes characterized as 'blue', RBLs as 'red'. There has also being an effort to convert this naming convention into something more quantitative (Lin et al. 1999). Under such a plan, BL Lacs are classified as high-frequency (HBL) or low-frequency (LBL) based on a more quantitative criterion. In fact, it turns out that most XBLs are HBLs, and most RBLs are LBLs.

The Type 0 radio-loud objects, i.e. BL Lacs and FSRQs, have also been grouped into a class of objects called **blazars** which are at the focus of this thesis. Blazars are discussed in detail in Section 4.5.

4.3 The Standard Model of AGN

The prodigious energy output characteristic of AGN is believed to be due to accretion of matter onto a compact object.

4.3.1 Accretion Model

To illustrate the energy produced through this process consider a simple model where the central object, with mass M and radius R, is surrounded by an initially stationary, uniform cloud of matter that is gravitationally attracted to the central object. If a small amount of mass (ΔM) is brought in from infinity and deposited on the central body, it must deposit all its gravitational energy $GM\Delta M/R$ in the central compact body. To be in thermal equilibrium, the central mass must radiate this energy away, so we can write the resulting luminosity in terms of the

deposited energy

$$L = \frac{\Delta E}{\Delta t} = \frac{GM\Delta M}{R\Delta t} \tag{4.1}$$

where the central object accretes a mass ΔM in a time Δt. If we write the luminosity in terms of the Schwarzchild radius of the central mass ($R_s = 2GM/c^2$), then Equation 4.1 becomes:

$$L = \left[\frac{R_s}{2R}\right] \dot{M}c^2 \tag{4.2}$$

From Equation 4.2, the luminosity of the central object is seen to be proportional to the rate of change of its rest mass, and the term in brackets can be interpreted as the efficiency of this process.

This result implies that the efficiency goes up as the object becomes more compact. In fact, for a solar-mass neutron star with a radius of 15 km, the accretion efficiency according to Equation 4.2 is $\sim$0.1. This is at least an order of magnitude higher than efficiencies for nuclear reactions (Longair 1992).

The compact body occupying the centre of AGN is believed to be a **supermassive black hole**. The masses of these central bodies have been indirectly inferred to range from $10^6 M_\odot$ to $10^8 M_\odot$. Though other engines have been postulated in the past (ibid.), black holes appear to be the best candidates for producing such large amounts of energy in such small volumes. Accretion onto a black hole is thus the most reasonable process for powering AGN, due to the relatively high efficiency. This can explain the significant amounts of energy released in such small regions (the Schwarzschild radius of a $10^{10} M_\odot$ black hole is 0.001 pc).

A simple **AGN model** is shown schematically in Figure 4.1. The central black hole powers the AGN, and is surrounded by a luminous accretion disk. Orbiting around this disk are clouds which produce the observed emission lines. The broad emission lines are produced by the clouds (dark spots) moving close to the black hole at high velocities ($\geq 10^4$ km/s). The more distant clouds

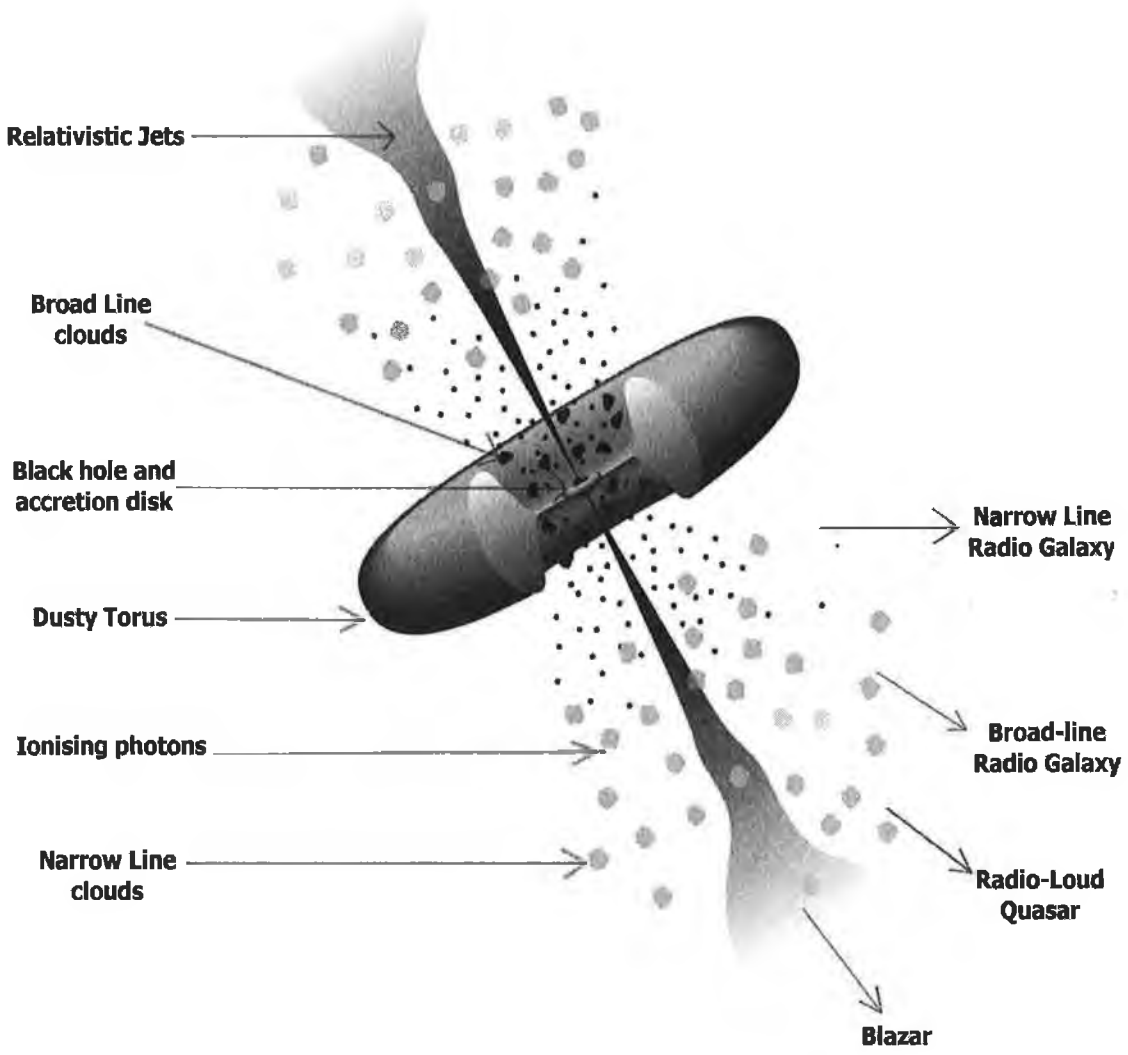

Figure 4.1: An idealised diagram (not to scale) of the current paradigm for radio-loud AGN (after Urry & Padovani (1995)). The thermal emission emanates from the torus and accretion disk, and the non-thermal emission from the jets.

(grey spots) which are moving more slowly are responsible for the narrow-line emission. The thick dusty torus obscures the broad-line region from transverse lines of sight, although some continuum and broad-line emission can be scattered into those lines of sight by hot electrons (black dots). Emanating at relativistic speeds near the black hole are the diffuse plasma jets, characteristic of radio-loud AGN. The exact composition of the outflow is uncertain: both electron-positron and electron-proton scenarios have been proposed.

For transverse lines of sight only the narrow-line emitting clouds are seen (Type 2 AGN), whereas the near-infrared to soft x-ray nuclear continuum and broad-lines are visible only when viewed face-on (Type 1 AGN). Emission characteristic of blazars (Type 0 AGN) results from observations close to the line of sight of the jet.

4.3.2 Jets

The relativistic jet is orientated perpendicular to the accretion disk and produces strong anisotropy and amplification of the continuum emission by relativistic beaming. As far as gamma-ray astronomy is concerned, these jets are the most important features of the AGN model, since it is believed that they Doppler-boost photons to gamma-ray energies.

Shocks in the jet lead to emission of photons, which is principally synchrotron radiation in the radio band and Compton-upscattered emission (of either the synchrotron radiation or external optical/UV photons) at shorter wavelengths. The bulk Lorentz factor for a typical jet varies for different conditions and models, and may range from $\sim$2 to 30, but nevertheless leads to considerable beaming of radiation along the jet direction. If viewed from that direction, as in a blazar, then the object may appear as a strong gamma-ray emitter, sometimes with photon energies up to $\sim$ 10 TeV.

Energetic jets with velocities close to the speed of light can eject hot electrons and gas over great distances. Where these jets meet more dense material, they

cause hot spots and shock fronts. The total kinetic power of a jet may rival the accretion power itself.

What powers jets and why they appear in only a small fraction of sources is unclear. It has been long suggested that magnetic fields enable the spin energy of the black hole to be tapped and liberated as kinetic energy in jets. For example, the spinning black hole may wind up the magnetic fields of the galaxy and expel them along two narrow jets (Semenov et al. 2004). Alternatively, the energy may come from a small volume of space around the black hole itself, or the jets may be produced by the hot accretion disk of gas that spirals into the black hole.

4.3.3 Superluminal Motion

Observational evidence for jets in AGN originally came from radio studies. The jets are not homogeneous, but appear to include a series of knots along their axes. Extended radio observations of these knots in a number of AGN implies that they are moving along the jet at speeds greater than c.

This phenomenon occurs for emitting regions moving at very high (but still sub-luminal) speeds at small angles to the line of sight (Rees 1966). Relativistically moving sources "run after" the photons they emit, strongly reducing the time interval separating any two events in the observer's frame and creating the impression of faster-than-light motion.

4.4 Unification

The axi-symmetric model of AGN discussed above implies widely different observational properties at different viewing angles. This may lead to inherently similar sources displaying widely different observed characteristics, which can give rise to pseudo-classifications - hence the need for a 'unified scheme' where the intrinsic properties are incorporated to unify apparently different classes of AGN.

From this model, it is possible to understand most of the different AGN types

as consequences of different viewing angles with respect to the rotation axis and of the presence or absence of jets. There are two effects of the viewing angle on the observations: simple shadowing effects of the torus and the Doppler-boosting of a relativistic jet viewed at small angles. For large viewing angles the broad-line emission from the galactic core may be hidden by the torus, so that a narrow-line or Type 1 AGN is observed. Evidence for such obscuration has been observed from polarimetric (Antonucci & Miller 1985), infrared and x-ray observations (see Ueno et al. (1994a,b)). These considerations lead to relationships between the viewing angle with respect to the jet direction and the observed properties of radio-loud and radio-quiet AGN.

Seyfert 2 galaxies have therefore been unified with Seyfert 1 galaxies, whilst low-luminosity (FR I) and high-luminosity (FR II) radio galaxies have been unified with BL Lacs and radio quasars respectively (see Antonucci (1993), Urry & Padovani (1995) and references therein). For reasons still unclear, BL Lac objects have extremely weak emission lines, and their continuum is very strong and non-thermal.

4.5 Blazars as Gamma-ray Sources

The majority of extragalactic sources of VHE gamma radiation observed to date fall under the subclass heading of blazars. This makes blazars unique in the extragalactic sky by virtue of the fact that they are observable over the known electromagnetic spectrum, some nineteen decades of energy.

Blazars are characterised by extremely high luminosity non-thermal emission, and short and long time-scale variability. The gamma-ray luminosities are in the range $10^{38} - 10^{41}$ W (under the assumption of isotropy) and in many cases the output in gamma rays dominates the total bolometric luminosity.

Blazars are the special class of radio-loud AGN with their jets pointing more or less towards the observer, and therefore constitute a relatively rare class of object. Since radio-loud objects make up only 10-15% of the AGN population

(Kellermann et al. 1989) and a generous upper limit to the fraction of blazars amongst radio sources is 50% (Stickel et al. 1994), it then follows that blazars probably make up less than 5% of all AGN.

The main properties that characterise blazars are:

- radio loudness,
- rapid variability (high $\Delta L/\Delta t$)
- high and variable optical polarization ($P_{opt} > 3\%$)
- smooth, broad, non-thermal continuum
- compact, flat-spectrum radio emission ($f_{core} \gg f_{extended}$)
- superluminal motion in sources with multiple-epoch Very Large Baseline Interferometry (VLBI) maps.

All the above properties are consistent with relativistic beaming, that is with bulk relativistic motion of the emitting plasma towards the observer.

4.5.1 Relativistic Beaming

There are by now various arguments in favor of relativistic beaming in blazars, summarized for example by Urry & Padovani (1995). Beaming is a direct consequence of the Lorentz transformations of special relativity and the Doppler effect, and has enormous effects on the observed luminosities.

The relativistic Doppler factor for radiation emitted by a source moving at an angle θ to the line of sight is given by:

$$\delta = \frac{1}{[\gamma(1 - \beta cos\theta)]} \tag{4.3}$$

where the Lorentz factor is $\gamma = (1 - \beta^2)^{-\frac{1}{2}}$ with $\beta = v/c$. The Doppler factor relates the intrinsic and observed flux for a source moving with respect to an observer. Photons are received in the observed frame at a rate δ times the rate

they are emitted. The Doppler factor is a strong function of the aspect angle and can become very large for $\beta \rightarrow 1$. Its dependence on the angle between the motion of the source and the observer shows that the observed properties of AGN are dependent on the angle of view. The observed flux increases with decreasing angle, culminating in maximum flux for head-on observation i.e. for $\theta = 0$.

To calculate the brightness in the observer's frame, two factors are involved:

1. The solid angle subtended in the observed and emitted frames is different. The angle θ transforms as $sin\theta' = \delta sin\theta$ and so the solid angle transforms as $d\Omega' = \delta^2 d\Omega$

2. Photons received at some particular energy in the observer's frame will have been emitted at a different energy.

Using a spectrum $F_\nu \propto \nu^{-\alpha}$, it turns out that the observed luminosity (L_{obs}) at a given frequency is related to the emitted luminosity (L_{em}) in the rest frame of the source via

$$L_{obs} = \delta^p L_{em} \tag{4.4}$$

with $p = (2+\alpha)$ in the case of a continuous jet or $p=(3+\alpha)$ in the case of a moving sphere (Urry & Padovani 1995). Thus the emission from a blob approaching an observer is Doppler-boosted and the apparent luminosity is increased by a factor δ^p. The emission from a receding blob will be Doppler-shifted to longer wavelengths and the luminosity decreased by factor δ^p.

For example, with $\theta \sim 2^o$, and using typical values for $\gamma \sim 5$ and $p \sim 3$, the observed luminosity can be amplified by factors of thousands. That is, for jets pointing almost towards the observer the observed luminosity can exceed the luminosity in the rest-frame of the jet by more than three orders of magnitude. As a consequence of amplification, beaming gives rise to a strong collimation of the radiation, which is larger for higher Lorentz factor γ.

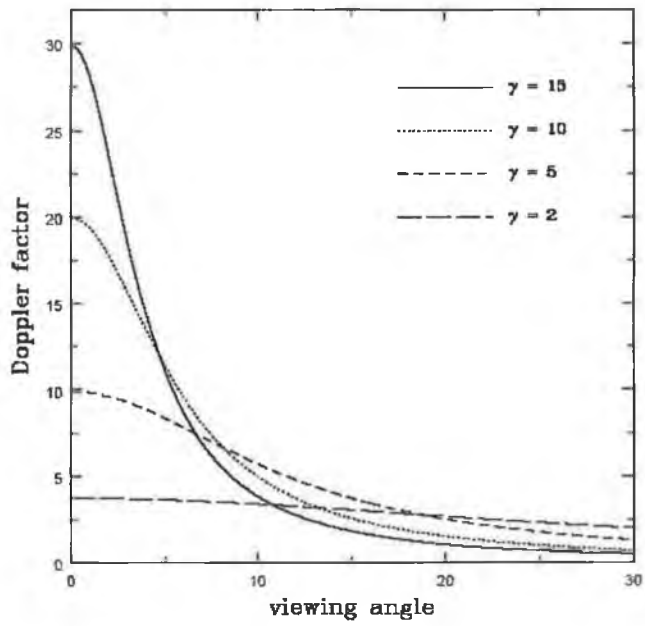

Figure 4.2: The dependence of the Doppler factor δ on the angle to the line of sight. Different curves correspond to different Lorentz factors: from the top down, $\gamma = 15$ (solid line), $\gamma = 10$ (dotted line), $\gamma = 5$ (short-dashed line), $\gamma = 2$ (long-dashed line). From Skelton (1999).

Large-amplitude flux variations over short time scales have been observed for a number of gamma-ray blazars. For example, doubling of the VHE flux from Markarian 421 over a period of fifteen minutes was observed using the Whipple telescope (Gaidos et al. 1996): see Figure 4.3. A limit on the size of the emission region (R') may then be imposed using the causality relationship:

$$R' = dt_{obs} \times c \tag{4.5}$$

where dt_{obs} is the shortest time scale over which variability is observed. This is relevant to the issue of gamma-ray emission from blazars. In fact, if blazar emission were not beamed, the small emission region implied from Equation 4.5, would make it virtually impossible for gamma rays to escape. All gamma-ray photons would be absorbed due to the dense low-energy photon field. The end product would be electron-positron pairs. However, if the radiation is beamed, the

observed variability time scale is a factor δ smaller than the intrinsic variability. As a result, the actual size of the emission region is

$$R = \delta \times dt_{obs} \times c$$

and the gamma-ray photons can escape from the source.

4.5.2 TeV Detections

In 1992 the blazar Markarian 421 (Mrk 421) was detected using the Whipple telescope, the first such object to be detected at photon energies greater than 0.5 TeV (Punch et al. 1992). It has since shown strong variability, with recorded outbursts reaching flux levels of 10 Crab. Moreover, the variability has been very rapid, with doubling times as short as 15 minutes (Gaidos et al. 1996). The most detailed TeV spectrum of Mrk 421 was measured during a period of exceptionally strong and long-lasting flaring activity in early 2001 (Krennrich et al. 2001). The spectrum derived from these data is well fitted by a power law with an exponential cutoff

$$F(E) \propto E^{-\alpha} e^{-E/Ec}$$

with $E_c = 4.3 \pm 0.3$ TeV (Krennrich et al. 2001). The existence of a cutoff energy can be attributed to gamma-ray absorption by the extragalactic infrared background light (**EBL**).

The initial 1992 detection was a surprise, since Mrk 421 was barely detectable by EGRET in the MeV-GeV range, even when flaring. Some quasars, such as 3C279 (z=0.538), are much brighter then Mrk 421 at a few GeV, but the observed upper limits on the TeV flux fall below the extrapolated spectrum by more than an order of magnitude. The common belief is that TeV non-detection of GeV gamma-ray-bright sources is due to absorption of the highest energy photons by pair-production interactions with the EBL (Stecker et al. 1992). However, because Mrk 421 is relatively close ($z = 0.031$), the absorption is small up to

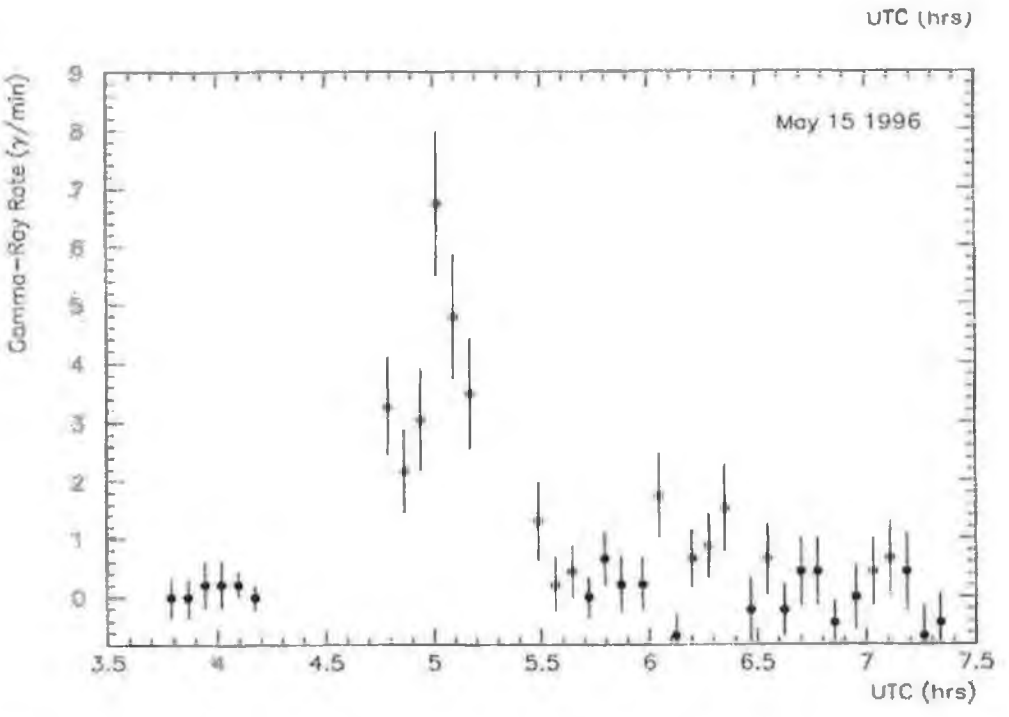

Figure 4.3: The light curve from the Mrk421 VHE flare in May 1996. The short doubling time indicates a very compact emission region (15 light minutes) (Gaidos et al. 1996).

several TeV.

Vassiliev (2000), Dwek & Krennrich (2005), Schroedter (2005) and others have deduced upper limits on the EBL energy density from the TeV spectrum of Mrk 421, and these limits suggest that 1 TeV photons should not be seriously absorbed below $z = 0.1$, though 10 TeV photons would not be expected to reach us from much further away than $z \sim 0.035$.

Since the detection of Mrk 421, five other blazar sources have been detected in the TeV regime: Markarian 501 (Mrk 501), PKS 2155-304, H 1426+428, 1ES 1959+650, 1ES 2344+514.

- Mrk 501, $z = 0.034$, was the third TeV source discovered. It was detected in 1995 by the Whipple telescope at approximately 0.1 Crab (Quinn et al. 1996), and was not seen initially by EGRET. This established VHE gamma-ray astronomy as an independent field. In 1997 Mrk 501 displayed rapid, large-amplitude flux variability (Catanese et al. 1997). The spectral behaviour and the variability time scale of Mrk 501 have been employed in the determination of the effect of absorption by the EBL (Konopelko 2000; Vassiliev 2000).

- PKS 2155-304 is a southern hemisphere source, lying at a redshift of $z = 0.117$. It was first detected in 1999 by the Durham group (Chadwick et al. 1999). Because of the large redshift, this source is of interest for the study of the EBL, which limits the propagation of TeV photons. A 45σ detection of PKS 2155 above 160 GeV was achieved using the H.E.S.S. array (Leroy & the H. E. S. S. Collaboration 2004).

- H 1426+428, which is the most distant confirmed source, lies at a redshift of $z = 0.129$. In 2002, Whipple reported a detection at the 5.5σ level, with observed source strength $\sim$0.06 Crab (Horan & Weekes 2004). Like PKS 2155, H 1426 is of interest for EBL studies because of its large distance (Aharonian et al. 2002a).

- 1ES 1959+650, at a redshift of 0.047 was first detected at VHE energies by the Utah Seven Telescope Array in mid-1998 (Nishiyama 1999). During May 2002, it was seen in a flaring state in the VHE energy regime for the first time by the Whipple Observatory (Holder et al. 2003). During the following two months, the object was intensely monitored by the VERITAS and HEGRA collaborations (Aharonian et al. 2003). Overlapping with the VHE observations were radio, optical and x-ray observations (Horns & Konopelko 2002; Krawczynski et al. 2003).

- 1ES 2344+514 has been monitored by the VERITAS collaboration since 1995 (Catanese et al. 1998)). The object was observed in a flaring state during the night of 20 December 1995. This is the only strong flare observed from this object to date, yielding a significance of 5.3σ. Recently, the HEGRA collaboration reported an independent confirmation of this source (Tluczykont 2003). 1ES 2344 is the primary subject of analysis in this thesis. A more detailed discussion of the source is contained in Chapter 6.

Over the last decade, multi-wavelength campaigns on Mrk 421, Mrk 501, and 1ES 1959+650 have shown evidence for correlation between the x-ray and VHE fluxes. Flares at these energies have been observed on time scales of half-hour to weeks. During these flares, the spectrum typically hardens as the flux increases. It has been noted that the GeV gamma-ray flux varies in magnitude far less than does either the x-ray or TeV emission.

The x-ray and TeV fluxes show similar decay times and amplitudes, which suggests there may be a correlation between the x-ray and TeV gamma ray emission, with the same particles perhaps contributing to both. The high-energy electrons responsible for the synchrotron emission could then give rise to the TeV emission by the inverse-Compton scattering mechanism (see Section 4.5.3). This would imply that the GeV gamma rays ought to be correlated with lower-energy synchrotron emission, such as optical or IR. The exact correlation is difficult to establish as hysteresis occurs and simultaneous x-ray and VHE spectra can

rarely be measured. Multi-wavelength observations of the other VHE blazars 1ES 2344+514, PKS 2155-304, and H 1426+428 have not been as successful because the VHE flux level is very low. This is likely to change with the improved sensitivity of IACT arrays.

4.5.3 The Blazar Spectrum

The spectral energy distributions (**SEDs**) of blazars are typically double-humped, when displayed as plots of νF_ν versus $\log(\nu)$, where F_ν is the integral flux above frequency ν (the photon energy $E = h\nu$).

The first component generally peaks somewhere between the infrared and the optical for the so-called "red blazars", and in the UV/x-ray region for so-called "blue blazars". This lower-energy component is **polarized** and rapidly variable, especially above the peak. This radiation is believed to be produced by a relativistic electron population within the jets of the AGN.

The second component extends up to the gamma-ray regime, peaking at GeV energies in red blazars and at TeV energies in blue blazars, and its origin is less well understood. A popular model is that it originates from inverse-Compton (IC) scattering of seed photons off the electrons in the jet. The origin of the seed photons is under debate, and could be different in red and blue blazars. It is current belief that the seed photons originate external to the jet (thermal emission from disk, broad line regions, or torus) in red blazars, and internal to the jet (synchrotron-self Compton, SSC) in their blue counterparts.

An example of a broad-band AGN spectrum (Mrk 421) is shown in Figure 4.4. The SED is presented as a νF_ν plot. On the νF_ν plot, a power-law spectrum with index $\alpha = -1$ (i.e. $F(E) \propto E^{-1}$) will appear flat; a rising portion will have $\alpha > -1$, and the falling part of the plot will have $\alpha < -1$.

The lower-energy hump, which peaks at $\sim$0.5 keV in Figure 4.4, is believed to arise from synchrotron radiation. The strongest evidence for this is that the emission is highly polarized (Krolik 1999). In this case, since the synchrotron

peak occurs in the x-ray range, the source is classified as an x-ray selected or "blue" blazar.

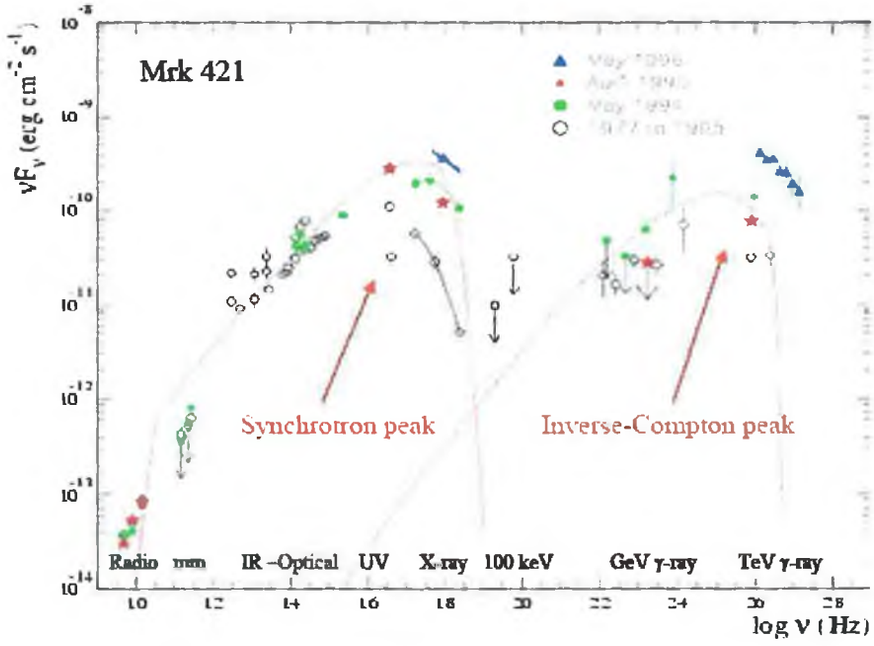

Figure 4.4: Broad-band spectrum of Markarian 421, including observations and model fits.

However, for the higher energy component of the spectrum, there are two main classes of models (Figure 4.5):

1. Leptonic models: High-energy **electrons** involved in the synchrotron emission can produce gamma-rays via inverse-Compton scattering of ambient photons of synchrotron-generated low-energy photons.

2. Hadronic models: High-energy **protons** can produce gamma-rays via collisions with matter in the jet regions.

In electron-based models, the relativistic electrons that cause the synchrotron radiation can also up-scatter the low-energy photons in the jet; this is the synchrotron-self-Compton (SSC) model. In **external-Compton** (EC) models, the seed photons impinge upon the up-scattering electron population from outside

(Sikora et al. 1994). Though both types of models have been applied to observations of Markarian 421, it appears that the SSC models are more appropriate for explaining the emission from this AGN (Coppi & Aharonian 1999).

Figure 4.5: High-energy gamma-ray production in a relativistic jet.

The most immediate consequence of the SSC model is that the synchrotron and IC emission should be correlated. Since the IC spectral component is derived from the synchrotron component within a finite emission volume, the time difference between correlated flares in each band is expected to be approximately the light-crossing time of the emission region (Krawczynski et al. 2002). Since the IC emission follows from the synchrotron emission, one expects it to trail the synchrotron emission by roughly this crossing time. In addition, the peak IC flux is expected to vary as the square of the peak synchrotron flux (Takahashi et al. 1996), so a quadratic fit to the correlated flux ratios in the two bands is also evidence of the SSC process.

SSC models are generally very successful in reproducing the spectra of high-frequency-peaked BL Lacs. However, the mechanism effectively fails in explaining the source spectra where the gamma-ray luminosity exceeds the optical luminosity, a phenomenon observed in some of the strong EGRET blazars. In addition,

recent observations of TeV gamma-ray emission from Mrk 501 during the 1997 flaring state pose severe constraints on models based on electron acceleration and inverse-Compton upscattering alone (Konopelko 1999b).

In hadronic-based models, protons enter the jet (Mannheim 1993). These protons are accelerated up to energies of 10^{18} eV at shock fronts propagating along the jet (Biermann & Strittmatter 1987), where photo-production of pions is the dominant cooling process (Figure 4.5). The pions produced will induce electromagnetic cascades in the jets, creating gamma-ray emission. If the energy of the gamma rays is above the critical value, they will produce $e^{\pm}$ pairs which can in turn radiate high-energy gamma rays. This cascade cycle is repeated until the energy of the gamma rays is less than the critical energy for $e^{\pm}$ pair production.

Simultaneous observations of blazars with different instruments over a wide range of energies may provide some answers as to the mechanisms leading to TeV gamma radiation. Multi-frequency campaigns on Mrk 421 in 1995 and Mrk 501 in 1996 have shown significant correlations between x-ray and gamma-ray emission with time lags of less than a day. This correlation is natural in the context of the SSC model, whereas the proton models are less predictive in this respect. However, the detection of neutrinos from an AGN would unambiguously indicate the presence of protons in the jets. This possibility will depend on significant increases in the sensitivity of future neutrino detectors (Mannheim 1995).

Chapter 5

Analysis Methodology

The overall goal of an imaging Cherenkov telescope is the unambiguous detection of gamma rays from celestial sources. However, the vast majority of the images recorded by such a telescope originate from events which are not due to gamma rays. These are mainly hadronic showers, single local muons and sky noise fluctuations. Therefore, the key to the imaging technique is to record as much information as possible about as many events as possible, and to achieve maximal rejection of the copious background component.

The analysis methods applied to data recorded using the Whipple 10-metre telescope are numerous and varied, and are subject to constant development. While the methods may vary in some respects, they are all based on five principal steps:

1. Data selection
2. Image preparation
3. Image parameterisation
4. Gamma-ray selection
5. Signal calculation (including background estimation).

5.1 Data Selection

When selecting a database to use for a detailed analysis, a number of factors must be considered, such as sky condition, elevation angle and the condition of the telescope system during the course of the observations.

Observations at low elevations, where Cherenkov photons have to transverse a greater length of atmosphere, result in fainter images with reduced angular size. The observed size and intensity of an image can also be affected by variations in the atmospheric conditions, such as the presence of water vapour and cloud. This can have a dramatic effect on the transmission of Cherenkov light. The quality of the events detected by the telescope is greatly dependent upon these factors. Thus, the selection of a database for analysis requires careful consideration. Only observations taken under very good atmospheric conditions, free from hardware malfunctions and at elevation angles greater than 55° were used in the 1ES 2344 analysis.

5.2 Data Reduction and Cleaning Techniques

The raw data recorded by the data acquisition system must be subjected to a number of calibration and cleaning processes before high-level event discrimination is applied. There are a number of stages involved in the preparation of the raw Cherenkov images:

- Software padding is applied when using ON/OFF data to eliminate bias due to difference in sky noise.
- Image cleaning identifies the PMTs which contain genuine Cherenkov signals and rejects those whose signals are exclusively due to night-sky fluctuations.
- Flat-fielding is a relative calibration of the PMT channels to normalise the response of the detector.

- Parameterisation classifies the images in terms of their size and orientation. This then provides a basis for discrimination.

5.2.1 Image Cleaning and Calibration

The pre-parameterisation procedures of pedestal subtraction, PMT gain calibration, software padding and image cleaning all help maximise the true Cherenkov light content of EAS images, while simultaneously minimising the effects of background noise. These procedures are described below in order of their implementation:

- **Noise Padding**: When corresponding OFF-source data are used to estimate the ON-source background, differing NSB levels between the ON and OFF fields can introduce a bias when the analysis is applied. Padding attempts to correct for this. The NSB values are compared between the two fields on a pixel-by-pixel basis, and artificial noise is computationally added to the less noisy pixel according to the equation

$$N_{add} = R_G \sqrt{N_n^2 + N_q^2} \tag{5.1}$$

  Here, N_n is the NSB in the noisier pixel, N_q is the NSB in the quieter pixel, and R_G represents a random number selected from a Gaussian distribution with a mean of 0 and a standard deviation of 1. In this way the noise levels can be approximately equalized between the ON and OFF fields.

- **Pedestal Subtraction**: The pedestal is a small offset value imposed on each ADC channel. The pedestals allow for both negative and positive fluctuations due to night sky noise. The pedestals and the **night sky background** (NSB) are calculated using noise events, which are randomly-triggered (i.e. not triggered by an air shower) snapshots of the sky, recorded at a rate of 1 Hz. The value of the pedestal in the Whipple 10m system

is typically ~25 digital counts for each channel. For a Cherenkov event, the average pedestal value in each channel is subtracted from the value recorded from that channel to derive the signal due the Cherenkov light. The pedestal variance in each channel gives an indication of the night sky background fluctuations for that channel.

- **Image Cleaning**: Every event recorded by the telescope is contained within a number of camera PMTs (pixels). The NSB causes fluctuations in individual pixels that are unrelated to the shower image. Some of the these pixels will contain pure background light while others will contain a mixture of background and Cherenkov light. Each event is cleaned on a pixel-by-pixel basis to remove pixels containing background light. To be considered part of the picture the signal recorded from a pixel must be at least 4.25 times the standard deviation of the pedestal distribution for that channel. To be accepted as part of the boundary for an image, the channel must have a signal not less than 2.25 times the standard deviation of the pedestal distribution and must also be adjacent to a channel that is part of the picture. The pixels passing the picture and boundary cleaning conditions together make up the image of the Cherenkov event. If neither of these conditions is met, the channel is not considered to be part of the image and its value is set to zero. The limits chosen for the standard picture/boundary values (4.25/2.25) were derived from an optimisation routine applied to an extensive Crab Nebula dataset.

- **Gain Normalisation**: After each channel has had its pedestal subtracted and the events have been cleaned, each surviving channel must undergo gain normalisation. This normalization compensates for the differing gain of each PMT. The gain factors are calculated from nitrogen calibration data taken each night. The processes of gain normalisation and pedestal subtraction are collectively known as flat-fielding.

5.2.2 Parameterisation

Upon completion of the low-level processing, the image of each event is parameterised. Hillas (1985) proposed a moment-fitting procedure to quantify the shape and orientation of an image in the camera, based on the assumption that the image is an ellipse. An ellipse is fitted to the image and the Hillas parameters are calculated relative to the centre (see Appendix A). The parameters fall into two main categories, those relating to the shape of the image, and those relating to its position and orientation, as illustrated in Figure 5.1.

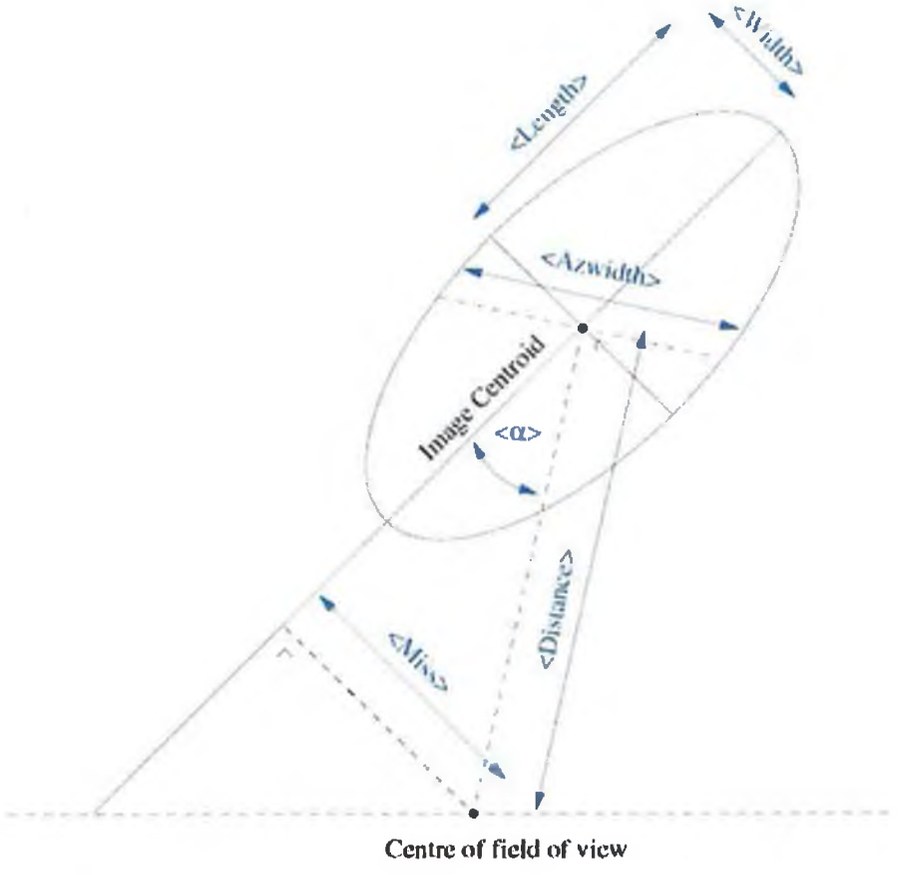

Figure 5.1: Geometrical definition of Hillas parameters, from Dunlea (2001).

The parameters related to the shape and size of the ellipse are:

- **Length**: This is the root-mean-squared (rms) spread of light along the major axis of the image and pertains to the longitudinal development of

the shower.

- **Width**: The rms spread of light along the minor axis of the image, pertaining to the lateral development of the shower.
- **Size**: Sum of the number of digital counts in all tubes which are part of the image, corresponding to the total light content (i.e. the luminosity) of the image. The size of the image is related to the energy of the primary particle.
- **Max1, max2, max3**: The number of digital counts in the highest and second and third highest tubes in the image.
- **Frac3**: This is the percentage of the total light content in the three highest tubes.
- **Asymmetry**: A measure of the asymmetry an image. Gamma-ray images should have their light distributions inclined toward their source position, resulting in a tear drop shape.
- **Length/Size**: Measure of the compactness of the image in relation to its total light content; used to eliminate background due to local muons

Parameters related to the orientation of the image are:

- **Alpha**: The angle between the major axis of the image and a line drawn from the centre of the camera to the centre of the image. It is related to the angle between the axis of the EAS and the axis of the telescope.
- **Distance**: The distance from the centroid of the image to the centre of the field of view of the camera. It gives information on the impact parameter of the shower with respect to the telescope.
- **Miss**: The perpendicular distance between the major axis of the image and the centre of the field of view of the camera. It is a measure of the shower orientation.

After the events of each data run have been parameterised, selection criteria can be used to reject cosmic ray events while retaining gamma-ray showers. Two methods are employed in this work, Supercuts and kernel analysis.

5.3 Supercuts Analysis

The Supercuts technique is the standard method applied to the Whipple data to discriminate between gamma rays and background (Punch et al. 1991). Event selection is carried out based on the image properties, i.e. the shape and orientation of the event image. Discrimination is achieved by rejecting events that do not lie within a chosen range for the parameters. The limits chosen can be thought of as the boundaries of a **gamma-ray domain** in parameter space. Images which have parameter values outside these boundaries are rejected as background. This approach is essentially a **box selection** method.

The boundaries of this gamma-ray domain are initially provided by Cherenkov event simulations. The cuts are then optimised on contemporaneous ON/OFF data from the Crab Nebula, for the particular telescope configuration (see Section 5.3.2 below).

Pre-selection Cuts

At this stage the data have been parameterised, and can now be subjected to preselection cuts. This effectively eliminates a large portion of background events, and is achieved through three forms:

- **Software Trigger Cuts**: A software trigger is applied which rejects background images that are too small to derive meaningful parameters. This serves as a tighter restriction than the analogous hardware trigger. The numbers of digital counts in the highest, and second and third highest, tubes in an image (max1, max2, max3) are required to be above certain levels. When comparing data it is important to take account of variations

in the trigger rate. Use of a fixed software trigger cut helps to compensate for varying hardware triggers.

- **Size Cut**: The size of an image is proportional to the energy of the instigating event. Thus the size cut (if applied) acts as an energy filter, imposed through software.

- **Frac3 Cut**: The frac3 cut requires that the percentage of the total light content in the three highest tubes be below a certain level. Using this cut eliminates events where a high proportion of the total light is contained in three or fewer tubes. Such events tend to be due to sky noise or caused by particles passing physically through the camera.

The events surviving pre-selection undergo further discrimination based on shape and orientation.

Shape and Orientation Cuts

The main parameters used for shape discrimination are length and width. Typical distributions for length and width are plotted in Figure 5.2 and Figure 5.3, respectively, for simulated gamma-rays events and for real background events. It can be seen that gamma-ray images tend to have smaller lengths and widths than the background images. This is due to the smaller dimensions of electromagnetic air showers.

Images due to single muons radiating close to the telescope tend to have large lengths and small sizes. The parameter length/size is used to discriminate between gamma rays and muons. Muons whose impact parameters are small form ring-shaped images (or parts of rings) due to the nature of Cherenkov emission. An ellipse fitted to such an image will be very large, and because the Cherenkov light is emitted by a single particle, it is not particularly intense, so one would expect muons to possess large values of length/size. However, for muons with large impact parameters the ring structure is only partially imaged. Such compact

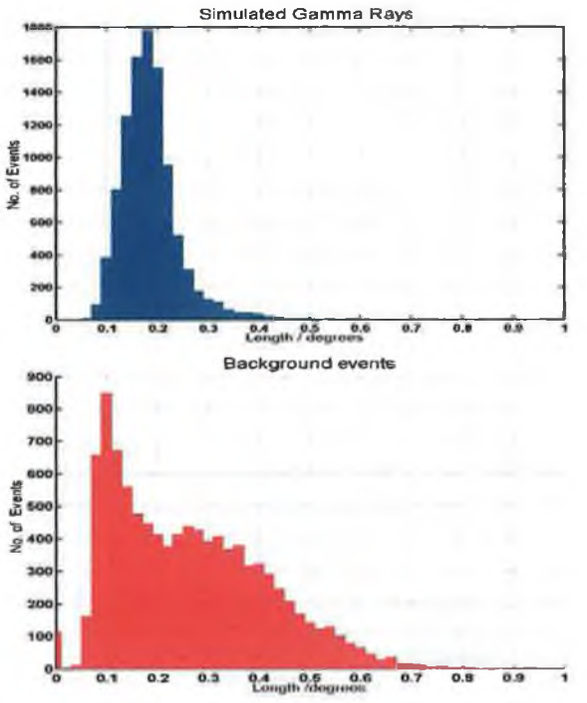

Figure 5.2: Length distributions for simulated gamma-ray events (top) and real background events (bottom).

muon arcs are very similar to gamma-ray-initiated images, and are quite difficult to discriminate.

The distance and alpha parameters of images are used to assist in background rejection. This only holds true when the potential source is considered to be a point source and is centred in the field of view.

- **Distance Cuts**: For a gamma-ray EAS falling close to the telescope, the resulting Cherenkov image will be close to the centre of the field of view, and will be almost circular in shape. Such events are difficult to parameterise correctly, and so are rejected. The images of events falling close to the edge of the camera may be truncated, leading to spurious large values of the alpha parameter. An upper distance cut is applied to remove such events.

- **Alpha Cut**: For a gamma-ray source at the centre of the field of view camera, the major axis of the ellipse should point towards the point of

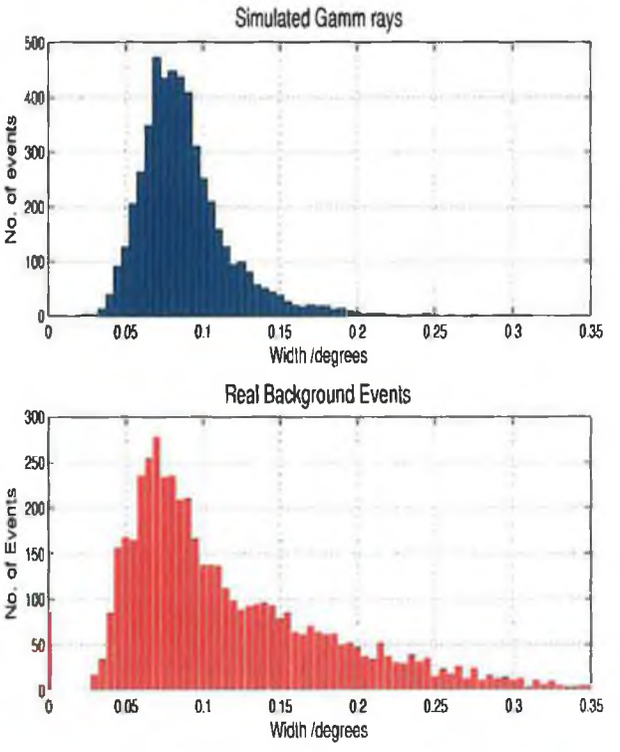

Figure 5.3: Width distributions for simulated gamma-ray events (top) and real background events (bottom).

origin. Thus, the alpha distribution for gamma-ray events originating in the centre of the field of view should peak at zero. This feature is obvious in Figure 5.4.

- **Asymmetry Cut**: For a gamma-ray event, more light falls on the side of the image nearest the point of origin; for such an image the asymmetry is positive. For a completely symmetric image the asymmetry = 0. Background events should have uniformly distributed asymmetries, due to their isotropic points of origin and irregularly shaped images. In this work, the asymmetry cut was not employed due to the small field of view of the camera.

The parameter cuts shown in Table 5.1 were optimized using data taken on the Crab Nebula during the 2000/2001 observing season (Lessard 1999). Collectively

Parameter	Lower Limit	Upper Limit
max1	30 d.c.	-
max2	30 d.c.	-
size	-	-
frac3	-	0.98
length	0.13°	0.25°
width	0.05°	0.12°
distance	0.4°	1°
length/size	0.0004°	-
alpha	0°	15.0°

Table 5.1: Standard parameter cut values; Supercuts 2000.

referred to as Supercuts 2000, these criteria are employed consistently throughout the standard analysis.

5.3.1 Significance Calculation

The measure of the statistical significance of the signal is given by the ratio of the signal to the error, calculated assuming a Poissonian noise distribution, and is determined by:

$$\sigma_{excess} = \frac{N_{ON} - N_{OFF}}{\sqrt{N_{ON} + N_{OFF}}} \tag{5.2}$$

where N_{ON} and N_{OFF} are the number of counts after background discrimination in the ON and OFF datasets, respectively (Li & Ma 1984). The significance measures the probability that the signal is real rather than a random fluctuation in the background level. Normally a significance of at least 3σ is required before a target object can be considered as a source. However, to take account of the fact that systematic effects may be present, a more conservative 5σ level criterion is often employed, coupled with an equivalent result from an independent experiment (Weekes 2000).

The corresponding gamma-ray rate may be determined using:

$$r \pm \Delta r = \frac{N_{ON} - N_{OFF}}{t} \pm \frac{\sqrt{N_{ON} - N_{OFF}}}{t} \tag{5.3}$$

where t is the duration of the scan.

For a graphical representation of the strength of a detection, an alpha plot is generally used, where all cuts except the alpha cut are applied and the alpha distribution is plotted for the surviving events. The presence of a gamma-ray signal is then seen as a peak at $\alpha \sim 0°$. A typical alpha plot for a set of Crab Nebula ON/OFF pairs is shown in Figure 5.4. The **sensitivity** of the detector/analysis system to a given source can be quoted in terms of significance per square root hour ($\sigma/\sqrt{hr}$). In the case of the Crab Nebula the sensitivity, calculated from the Supercuts result in Figure 5.4, is 5.5 $\sigma\sqrt{hr}$. This value of Crab sensitivity for the Whipple 10-metre system has remained generally constant (within $\pm 4\%$) over the observational period relevant in this work.

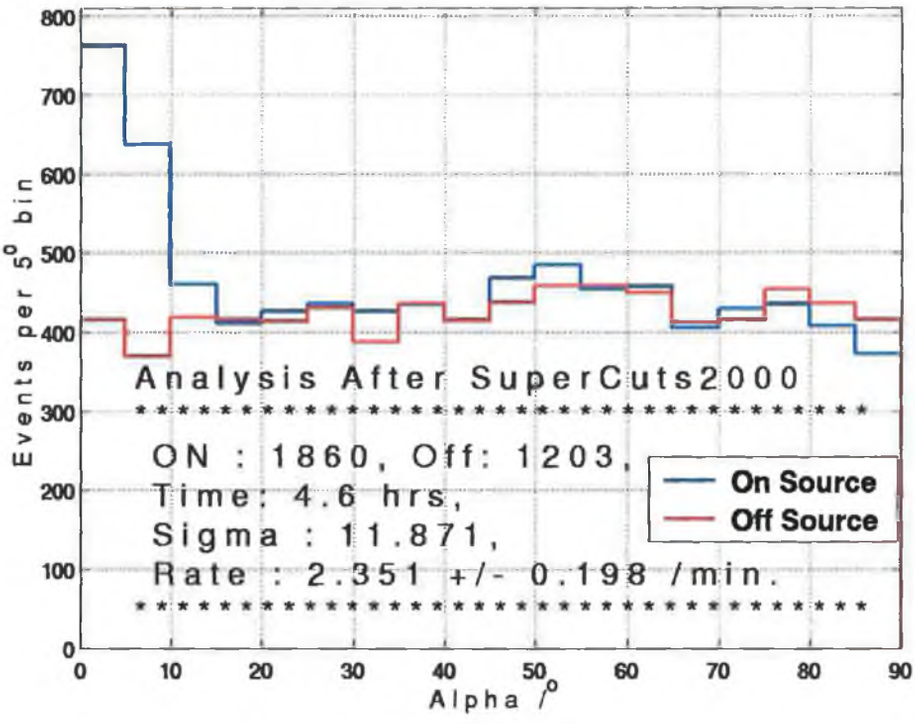

Figure 5.4: Alpha plot from analysis of 10 Crab Nebula pairs after application of Supercuts 2000.

Date	ON-run	OFF-run	Sky Quality	Elevation/°
020915	22717	22718	A	53
021010	22774	22775	A-	73
021031	22853	22854	A-	53
021104	22903	22904	A-	75
021105	22925	22926	A	76
021106	22947	22948	A-	70
021109	23009	23010	A-	65
021111	23036	23037	A	62
021112	23053	23054	A	79
021112	23055	23056	A	69

Table 5.2: Selected Crab Nebula pairs from Sept-Nov 2002. This data set was used to optimise Supercuts for the 2002/2003 observations.

5.3.2 Supercuts Optimisation

In this work, the Supercuts were re-optimised on a season-by-season basis to establish whether any significant improvement in background rejection could be achieved.

The values chosen for Supercuts have traditionally been optimised to give maximum gamma-ray significance on a subset of contemporaneous Crab data. The optimised cuts are tested on other confirmed TeV sources such as Markarian 421 or Markarian 501. Generally, to avoid bias, the Crab optimisation data-set is not used in any further scientific analyses.

As an example of this procedure, the optimisation for the 2002/2003 season is described here. Table 5.2 shows the Crab ON/OFF pairs used in the optimisation procedure. These observations were chosen as having reasonable elevation, stable rates in good weather and freedom from anomalies.

Each selection cut is initialised to a plausible starting value before optimisation begins. The optimum set of selection criteria are then determined with respect to one cut at a time, by fixing all cuts except the one under optimisation. The peak in a plot of gamma-ray significance versus cut value, for the cut under optimisation, represents its first "best-estimate" value. Once the first best-estimate of each cut is found, the process is repeated with the first best-estimates replacing the

Parameter Cut	Supercuts 2000	Re-optimised
Alpha	15°	10°
Lower Distance	0.4°	0.4°
Upper Distance	1.0°	1.0°
Lower Length	0.13°	0.14°
Upper Length	0.25°	0.23°
Lower Width	0.05°	0.05°
Upper Width	0.12°	0.11°
Length/Size	0.0004°/d.c.	0.00035°/d.c.

Table 5.3: Optimised cut values (relative to Crab-like flux and spectrum) compared with standard Supercuts 2000 values.

initial values. The eventual new set of optimised cuts was then subjected to another cycle of optimisation to arrive at the final values shown here. After several iterations the best-estimate cuts converge to their optimised values. For the present analysis the cuts were found to converge sufficiently to their optimised values after three iterations.

Table 5.3 provides a list of the cuts with their initial optimised values. The gamma-ray significance versus cut value distributions for a trial optimisation over all size values is presented in Figure 5.5, as examples of the type of plots obtained in the optimisation process. Changes in the optimum cut values for alpha, length, width and length/size can arise from a combination of tracking, focusing and mirror alignment improvements.

Table 5.4 shows the comparison of significance and rates between the re-optimised parameters and the standard Supercuts 2000 for the 10 Crab pairs used in the optimisation.

	Supercuts 2000	Optimised cuts
Significance /σ	11.871	13.984
Rate /min	2.440	1.681

Table 5.4: A Comparison of Supercuts 2000 and re-optimised cuts applied to Crab Nebula data.

The validity of the new cut values was tested using a selection of Mrk 421 data. The 10 Mrk 421 ON/OFF pairs (Table 5.5) date to Dec 2002 - Jan 2003,

Date	ON-run	OFF-run	Sky quality	Elevation/°
021204	23462	23163	A-	54
021205	23192	23193	B+	68
021207	23238	23239	B	60
021208	23256	23255	B	54
021208	23257	23258	B	60
021209	23274	23275	A-	55
021214	23336	23337	A-	76
030110	23618	23619	A-	81
030112	23640	23639	A-	68
030114	23651	23652	A-	83

Table 5.5: Selected Mrk 421 pairs from Dec 2002-Jan 2003. This data set was used to test the optimised Supercuts for the 2002/2003 season.

and were again selected on the basis of good weather, stable rates and acceptable elevation. A comparison of the significance and rates generated from both sets of cuts on the Mrk 421 pairs is shown in Table 5.6.

	Supercuts 2000	Optimised cuts
Significance $/\sigma$	11.696	13.904
Rate /min	1.934	1.321

Table 5.6: Comparison of Supercuts 2000 and re-optimised cuts applied to Mrk 421 pairs.

When the optimisation is based solely on the significance, the rate typically diminishes. While it appears the optimised cuts do achieve improvement for the Mrk 421 data, no improvement was observed when these cuts were applied in the analysis of a weak source such as 1ES 2344 and so the standard Supercuts 2000 values were employed consistently throughout this work.

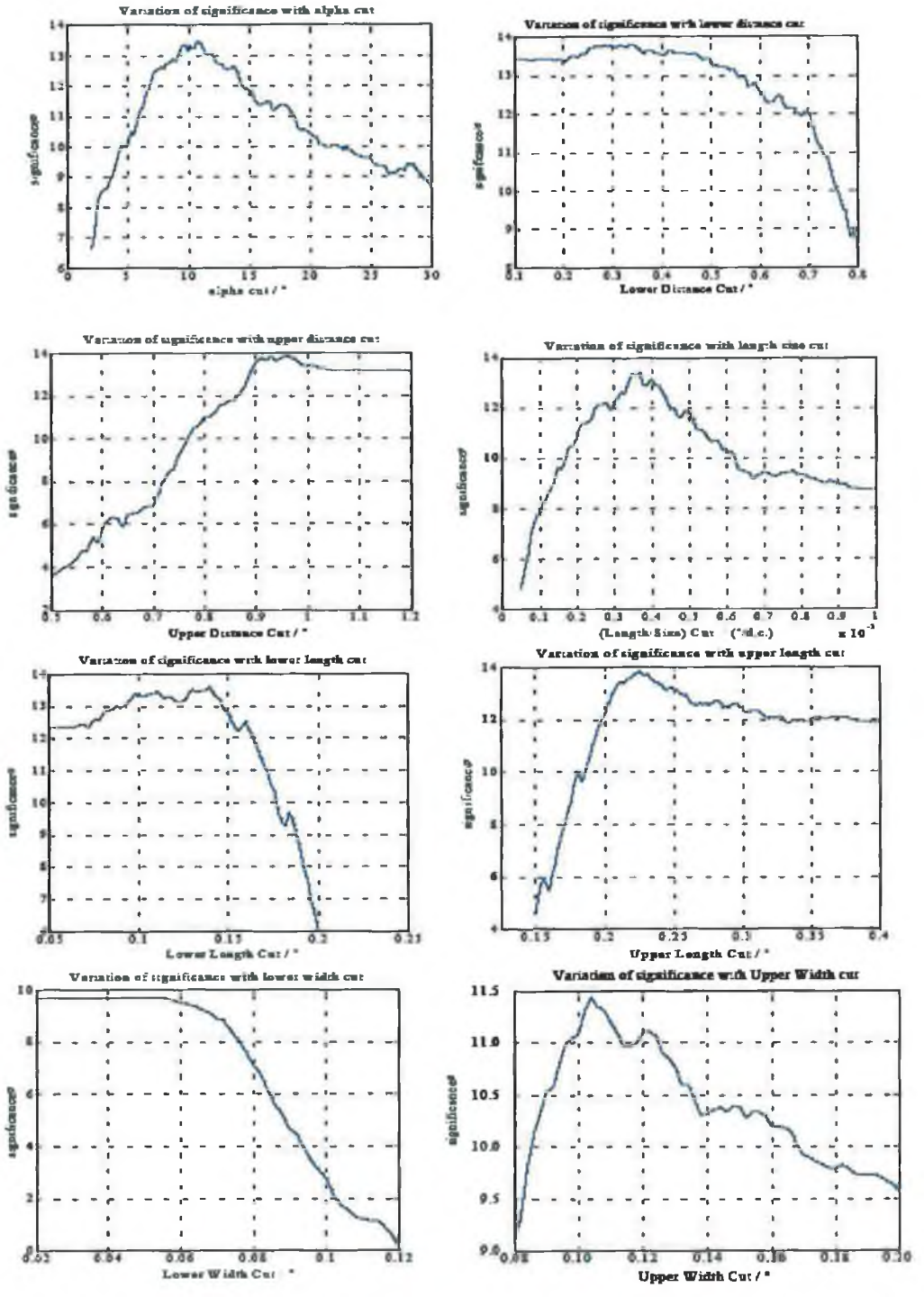

Figure 5.5: Plots of final significance versus cut values for the optimisation procedure. The position of the peak in each plot indicates the optimal cut value.

5.4 Matched Analysis

The ON/OFF analysis discussed above offers the ideal way to estimate the background. However, almost all the observations in the 1ES 2344 dataset have been taken in tracking mode, and the ON-data is thus without the corresponding contiguous control OFF-runs. For reasons discussed in Section 3.8.3, the tracking analysis, which estimates the background exclusively from the ON-run, was not applied to the 1ES 2344 data set.

An alternative method to estimate the background is to match a surrogate OFF-run to each tracking run on the basis of having been recorded at similar elevation and preferably on the same night. Analysis of these matched ON/OFF runs is then carried out as for normal ON/OFF pairs.

5.4.1 Matching Procedure

To match up the most suitable pairs, one must first compile a large set of high-quality OFF-observations. Each ON-run is then compared to all the OFF-runs to find the best match. This comparison uses the method devised by de la Calle Perez (2003), where ON and the OFF runs are matched on the basis of five parameters:

- **Mean Elevation Angle** (*el*): Since the source is usually rising or setting during observation the mean elevation value is of interest. In the matching procedure, the comparison is based on the secant of the mean elevation angle.

- **Relative Throughput** (*thru*): This is a measure of the sky quality, determined by comparison with a standard run that was recorded under optimal sky conditions (LeBohec & Holder 2003). A value ≥ 1 indicates good conditions. A matched pair should have equivalent throughputs, within 0.05, so to ensure that the runs are taken under similar atmospheric conditions.

- **Mean sky-noise** (*nsb)*: This represents the pedestal fluctuations of the photo-tubes. Having similar *nsb* values ensures that extra noise components are not added during software padding.

- **Number of pixels** (*pix*): The number of pixels turned off in a data-run (due the presence of stars etc.).

- **Modified Julian Date** (*mjd*): This marks the date on which the observation was recorded.

Modified Julian Date and relative throughput are used to ensure that both weather and telescope conditions are as similar as possible. The remaining parameters, elevation, mean night-sky background and number of pixels are included in the matching procedure to ensure comparable raw rates.

Relative throughput provides a measure of changes in the atmosphere and telescope over time and is defined as the ratio of the Cherenkov luminosity (i.e. the size of the image) produced by the same extensive air shower under different conditions (LeBohec & Holder 2003). Assuming that the spectrum of cosmic rays is constant at TeV energies, differences between the raw size distributions of two observations must arise from differences between the conditions under which those observations were made. Throughput is calculated using a reference run to which the data run in question is compared. A specific Crab Nebula run (number 23036) recorded under optimum conditions was chosen as the reference. The raw (unselected) size distribution for events in the reference run and that for events in a data run are constructed, and for the example shown in Figure 5.6 the two distributions are offset from one another. The size distribution of the data-run is scaled by a range of factors, until it matches that of the reference dataset. The scaling factor that minimises the difference between the two distributions (as determined using a χ^2 test) is defined as the relative throughput.

Once the run parameters for the ON-source and OFF-source data-sets have being determined, the matching procedure can commence. This is based on a

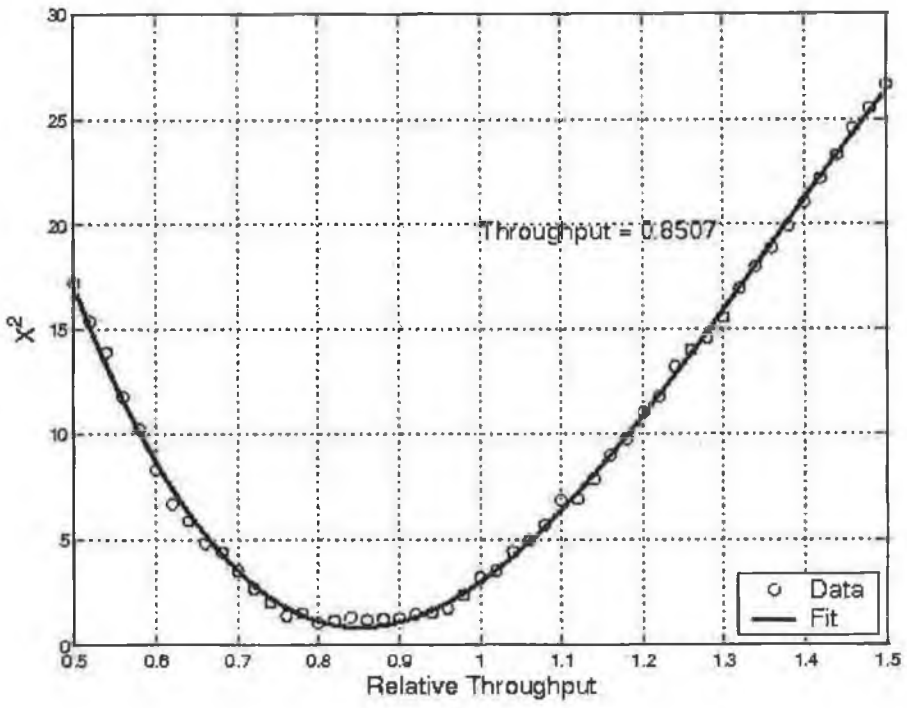

Figure 5.6: The throughput of run number 22717 relative to run number 23036.

matching score defined as follows:

$$Score = \left|\frac{mjd_2 - mjd_1}{w_{mjd}}\right| + \left|\frac{thru_2 - thru_1}{w_{thru}}\right| + \left|\frac{el_2 - el_1}{w_{el}}\right| + \left|\frac{nsb_2 - nsb_1}{w_{nsb}}\right| + \left|\frac{pix_2 - pix_1}{w_{pix}}\right| \tag{5.4}$$

The ON/OFF run parameter differences are weighted with values (w_i) chosen on the basis of improving the efficiency of the matching (de la Calle Perez 2003). The weights used in the present analysis are: $w_{mjd} = 30, w_{thru} = 0.1, w_{el} = 10, w_{nsb} = 0.3, w_{pix} = 5$. For a perfectly matched pair, the parameter differences and hence the *Score* would equal zero. The best-matched pairs are identified as those with the lowest scores. To avoid introduction of systematic effects, each OFF-run is used only once.

Once the matched ON/OFF pairs are obtained, the standard ON/OFF analyses is performed. Any residual difference in the total number of events after cuts can be corrected before the significance calculation is performed, by multiplying the total number of OFF-events by a **scaling factor** (Scf) so that the ON and OFF alpha plots match in the $20° - 65°$ region.

$$Scf = \frac{n_{on}}{n_{off}} \tag{5.5}$$

where n_{on} and n_{off} are the number of events with $20° \leq \alpha \leq 65°$ in the ON and OFF data after cuts. In the case where a scaling factor is applied the significance is calculated using a Gaussian formula (Fegan 2005):

$$\sigma_{excess} = \frac{N_{ON} - (Scf \times N_{OFF})}{\sqrt{N_{ON} + \frac{N_{OFF}^2}{n_{off}^2} n_{on} + \frac{n_{on}^2}{n_{off}^2} N_{OFF} + \frac{n_{on}^2 N_{OFF}^2}{n_{off}^4} n_{off}}} \tag{5.6}$$

and the rate is given by

$$r \pm \Delta r = \frac{N_{ON} - (Scf \times N_{OFF})}{t} \pm \frac{\sqrt{N_{ON} + \frac{N_{OFF}^2}{n_{off}^2} n_{on} + \frac{n_{on}^2}{n_{off}^2} N_{OFF} + \frac{n_{on}^2 N_{OFF}^2}{n_{off}^4} n_{off}}}{t} \tag{5.7}$$

where the uncertainty on Scf has been incorporated into Δr. However, if the overall alpha plots show no difference in the $\alpha > 20°$ region, and $Scf \sim 1$, scaling is not warranted, and the significance and rate are calculated in the normal way (Section 5.2).

5.5 Kernel Analysis

The Supercuts analysis employs a simple multi-dimensional box to discriminate between the gamma-ray and background events. This box acts like a crude filter and is constructed by placing fixed boundary limits on each parameter. This standard selection method has proved very successful, with the detection of a

number of VHE gamma-ray sources. This method, however, is not without disadvantages, including a bias against events of very low and very high energy. An alternative approach to box selection is to evaluate an individual event likelihood. This can thought of as the relative proximity of each event to a population of gamma-ray or hadron events in parameter space. This closeness can be expressed by a kernel function.

This multivariate technique allows for correlations between the parameters, in particular non-linear correlations, to be taken into account. The use of such a technique in TeV gamma-ray astronomy has been described previously by Moriarty & Samuelson (2000) and Dunlea et al. (2001). It was also applied in high-energy nuclear physics in the detection of the top quark (Holmström et al. 1995).

The kernel approach can result in a lower energy threshold in selecting events (~140 GeV), approaching the hardware threshold of the telescope. It has also been shown that the kernel technique offers higher background rejection and improved collection areas when compared with traditional box selection methods such as Supercuts (Gammell 2004).

5.5.1 The Kernel Method

The image parameter set used consists of: the width (w) and length (l) of the image ellipse; the distance (d) from ellipse center to camera center; the natural logarithm of the size ($\ln(s)$) and alpha (α) angle. An event is then represented as a vector $\mathbf{x}$=(α, w, l, d,$\ln(s)$).

Each event is then classified as gamma ray or background depending on a likelihood ratio:

$$R = \frac{f_G}{f_B} \tag{5.8}$$

where f_G is the likelihood that it is a gamma-ray event and f_B is the likelihood that it is a background event. f_G is estimated from a set of N_G gamma-ray

simulations with parameter vectors $\mathbf{g}_i$=$(\alpha_i, w_i, l_i, d_i, ln(s_i))$.

$$f_G = \frac{1}{N_G} \sum_{i=1}^{N_G} K(\mathbf{x} - \mathbf{g}_i) \tag{5.9}$$

f_B is estimated in a similar way from a set of N_B real background events with parameter vectors b_i. The kernel function $K(\mathbf{x} - \mathbf{g}_i)$ is effectively a point-spread function describing the influence of $\mathbf{g}_i$ at $\mathbf{x}$.

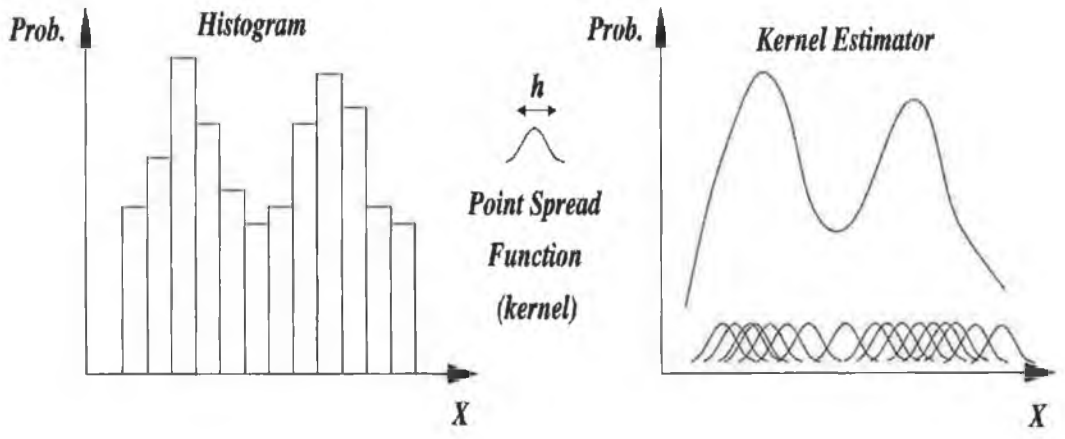

Figure 5.7: The Kernel probability density estimator: each data point is convolved with a point spread function which is then summed, producing a smooth approximation to the probability density distribution.

No simple function can describe the probability density distribution of gamma-ray images nor the distribution of background events. A simple diagrammatic representation of the kernel technique for a hypothetical univariate situation is shown in Figure 5.7. The probability density distribution of X can be crudely represented by a histogram, but the histogram is a less than ideal representation due to its discontinuous nature and its heavy dependence on the binning parameters used. A smoother continuous approximation to the true probability density distribution of X can be obtained by convolving each point in X with a point-spread function, to form a "kernel", and summing the results. The summing of these kernels is not unlike Fourier analysis in which a single-valued periodic

function may be built as a summation of individual sinusoidal components.

In this work a multivariate Gaussian is used as the kernel function:

$$K = \frac{1}{\sqrt{(2\pi)^n |\xi_G|}} \exp\left(-\frac{1}{2}\left(\frac{\mathbf{x}-\mathbf{g}_i}{h_G}\right)^{\mathrm{T}} \xi_G^{-1}\left(\frac{\mathbf{x}-\mathbf{g}_i}{h_G}\right)\right) \tag{5.10}$$

where n is the number of parameters and ξ_G is the covariance matrix of the gamma-ray dataset (a measure of the extent to which each parameter is correlated with every other parameter). For a kernel that is the product of Gaussians, with one Gaussian in each dimension, the scale factor h_G which minimises the mean integrated squared error between the kernel estimator and an actual distribution is (Hand 1982)

$$h_G = \left(\frac{4}{N_G\,(n+2)}\right)^{\frac{1}{n+4}} \tag{5.11}$$

The gamma-ray probability f_G may now be written as

$$f_G = \frac{1}{N_G h_G \sqrt{(2\pi)^n\,(\xi_G)}} \sum_{i=1}^{N_G} \exp\left(-\frac{1}{2h_G^2}\,(\mathbf{x}-\mathbf{g}_i)^T\,\xi_G^{-1}\,(\mathbf{x}-\mathbf{g}_i)\right) \tag{5.12}$$

The background likelihood f_B is estimated in a similar way from a set of N_B real background events with parameter vectors b_i and ξ_B is the covariance matrix of the background dataset,

$$f_B = \frac{1}{N_B h_B \sqrt{(2\pi)^n\,(\xi_B)}} \sum_{i=1}^{N_B} \exp\left(-\frac{1}{2h_B^2}\,(\mathbf{x}-\mathbf{b}_i)^T\,\xi_B^{-1}\,(\mathbf{x}-\mathbf{b}_i)\right) \tag{5.13}$$

For each event recorded in the ON and OFF files, the image is parameterised to give the vector $\mathbf{x}$. In this analysis, f_G and f_B are calculated on the basis of Equation 5.12 using a set of 10000 simulations[1] for g_i and 10000 real background events for b_i. The logarithm of the likelihood ratio, $\log(R)$, can now be calculated;

[1]The kernel estimator will depend on the spectral features of the gamma-ray sample. In the present case, the simulations were drawn from a power law spectrum with index 2.5 (as measured for the Crab Nebula emission). Thus the estimator can be expected to perform best for a source with a similar spectrum.

providing a score for each real data event processed. Thus, in a ideal distribution of $\log(R)$ values, gamma-ray events would be expected to possess positive $\log(R)$ values, and background events negative values.

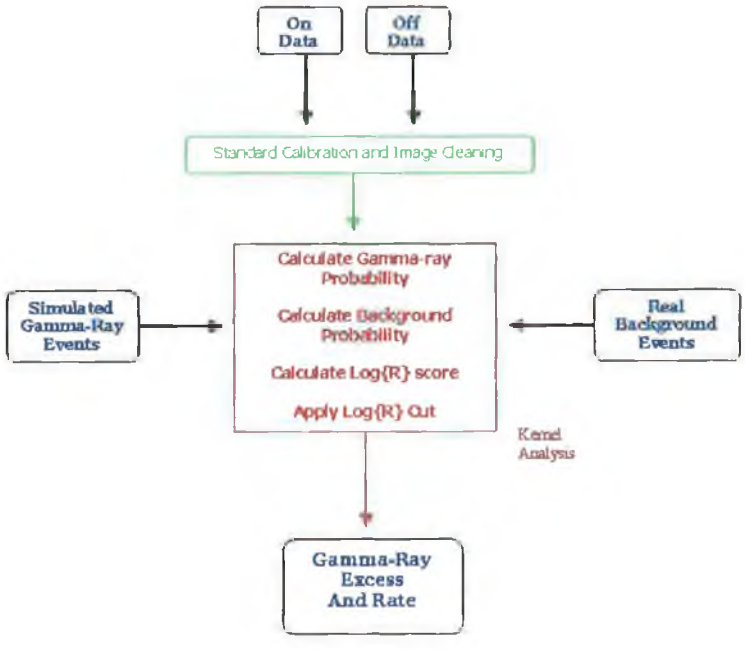

Figure 5.8: The kernel analysis procedure for ON/OFF data.

For a given $\log(R) = r_c$ value, the significance is determined using the standard Poisson excess calculation:

$$\sigma_{excess} = \frac{N_{ON} - N_{OFF}}{\sqrt{N_{ON} + N_{OFF}}} \tag{5.14}$$

where N_{ON} and N_{OFF} are the number of events with $\log(R) \geq r_c$ in the ON and OFF datasets, respectfully.

The gamma-ray rate, where t is the duration of the source observation, is calculated using Equation 5.3.

5.5.2 Pre-selection

Kernel analysis is computationally intensive as every event is compared with every gamma-ray simulation and with every background event. Two possibilities

for reducing the analysis time have been investigated, pre-selection of events and lattice analysis (Moriarty & Samuelson 2000).

The probability distributions f_G and f_B defined by Equations 5.12 and 5.13 represent the convolution of the gamma-ray simulations and background samples with a point-spread (kernel) function. The value of the log-likelihood function, $\log(R)$, can therefore be calculated for a **lattice** of points in n-dimensional parameter space. Values between the nodes of the lattice can be estimated using linear piecewise interpolation. The lattice analysis need only perform one linear piecewise interpolation per event, resulting in a reduced analysis time. Production of a sufficiently dense lattice requires many more calculations than a typical full kernel analysis on a data-run but it need only be carried out once for a given detector configuration.

Since most events in the data-set are not gamma-ray-initiated, many can be eliminated with loose cuts on individual parameters before applying the kernel analysis. By rejecting, in advance, those events whose parameters values fall within the background regions of parameter space, it is possible to reduce the kernel analysis computational workload, without significantly reducing the final gamma-ray rate. The pre-selection method can reduce the number of calculations by a factor of five and is the method employed in this work. The pre-selection cuts used for this work are $\alpha < 30°$, width$< 0.20°$ and length$< 0.35°$.

5.5.3 Simulations

In order to calculate the probability score for each data event the kernel analysis requires a set of pure gamma-ray events and a set of pure background events. In the latter case a sample of real events from contemporaneous OFF-source data is sufficient. The set of gamma-ray events are obtained from a series of computer simulations.

Before the kernel analysis begins the real background data and the simulated gamma-ray data are parameterised in the normal manner as described in Sec-

tion 5.2.2. The simulated gamma-ray events were produced and accumulated using the GrISU package, developed by VERITAS collaborators at Grinnell and Iowa State universities (Mohanty et al. 1998). As shown in Figure 5.9, the gamma rays created by the simulations do reproduce statistically the same parameter distributions as that of real events selected from Crab Nebula data by the Supercuts analysis.

The process of simulating gamma rays is split into three sequential components:

1. Production of an atmospheric particle shower from a VHE gamma ray. The routine **Kascade** simulates the physics of the particle showers that occur in the atmosphere. It traces out segments of the paths of all the particles created as the gamma rays interact with nuclei and produce electron-positron pairs. It effectively creates a 3-dimensional map of the EAS, reconstructing the interactions of each secondary particle as it descends through a model atmosphere. The Kascade programme was originally developed by Kertzman & Sembroski (1994).

2. The 3-D map created by Kascade is passed to **Cherenk**, the second program in the chain. Cherenk is a Monte Carlo routine which simulates the physics of Cherenkov radiation, models the atmosphere and index of refraction and calculates emission angles (Carter-Lewis 1992). The effects of the Earth's magnetic field are also included.

3. The final part of the simulation process models the optical and electronic processes in the Whipple 10m telescope system. The **GrISUDet** code tracks individual Cherenkov photons as they reflect from the mirrors and illuminate the camera and models the charge pulses produced by the photomultiplier tubes and subsequent electronics. At this stage, artificial noise is also injected into the data to reflect the level of background fight falling on the telescope. By varying the amount of noise in the simulations, and

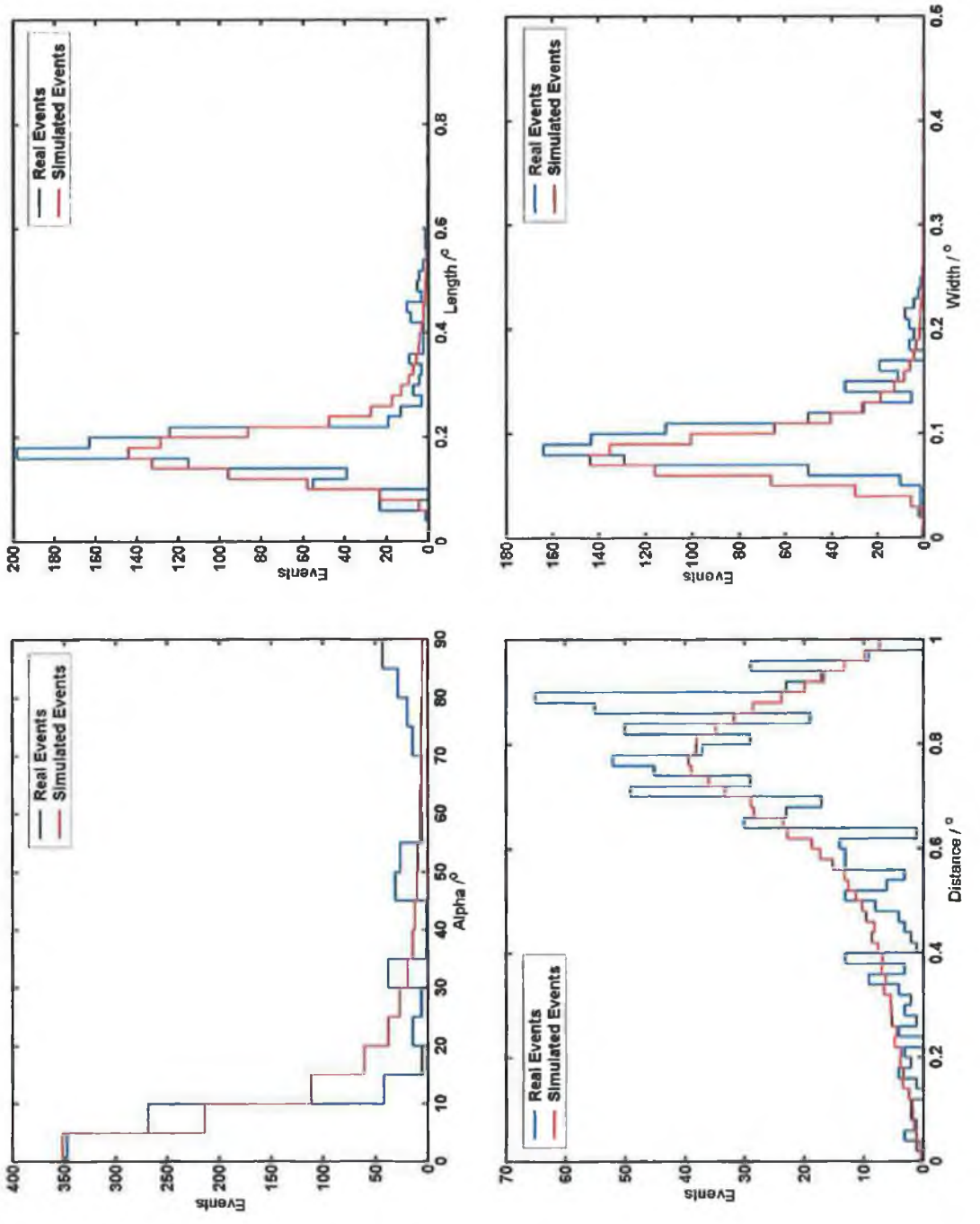

Figure 5.9: A comparison of parameter distributions between real gamma-ray events selected from the Crab after Supercuts and simulated gamma-ray events from a Crab-like spectrum.

comparing the resulting pedestal variance distribution to that of the real Crab Nebula data, the most suitable value can be identified.

Simulated events which have an energy above the energy threshold of the telescope will result in a 'trigger'. These simulated triggered events are subjected to image cleaning, calibration and parameterisation, exactly as for real Cherenkov events, and they can then be used for the kernel analysis or for diagnostic investigations.

In this work, gamma-ray events with energies chosen randomly from a 0.1 TeV to 10 TeV power-law distribution with a differential spectral index of 2.5 (the TeV spectral index of Crab Nebula) were simulated entering the atmosphere at 70° elevation (similar to the average elevation of the 1ES 2344 database). From a total of $\sim 1.5 \times 10^6$ simulations, 50000 events resulted in a trigger.

5.5.4 Optimisation of Kernel Cut

Ideally, if gamma-ray and background events were completely distinct, the $\log(R)$ boundary separating both populations would occur at zero, making discrimination easy. Unfortunately, this is not the case and with both distributions overlapping to some extent, optimisation is required to determine the most efficient $\log(R)$ cut. The kernel analysis effectively merges the five parameters (length, width, distance, size and alpha) into a single $\log(R)$ score. Thus, only this one parameter is optimised.

In order to determine the optimal $\log(R)$, a database of 10 ON/OFF pairs taken on the Crab Nebula was established. These were the same pairs used in the Supercuts optimisation in Table 5.2. These runs were taken during 2002, on nights with particularly clear skies. As with the Supercuts optimisation, the kernel cut was optimised using the significance of the signal above background.

In a plot of gamma-ray significance versus $\log(R)$ the peak represents the $\log(R)$ value above which the optimum signal-to-noise ratio is obtained (see Figure 5.10). From this plot, a value of $\log(R)$=5.1 was chosen as the optimised

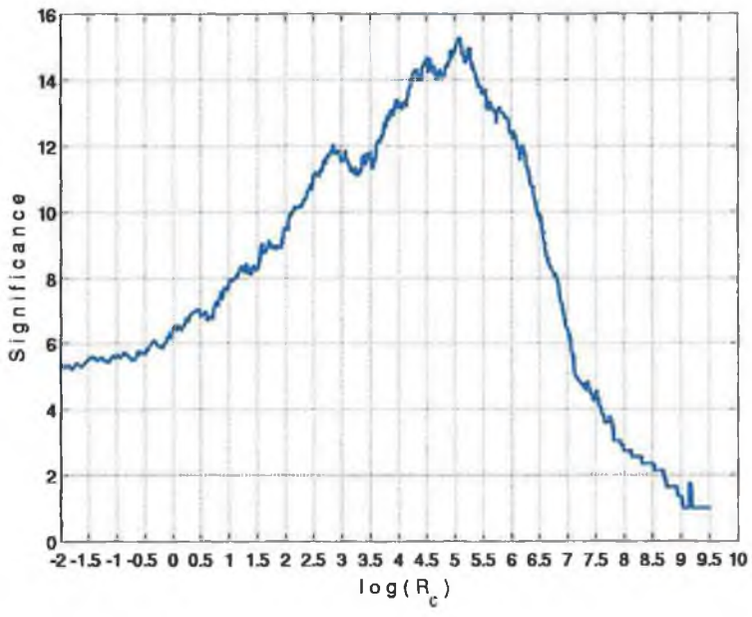

Figure 5.10: The kernel result for 10 ON/OFF pairs from the Crab Nebula. The peak of this distribution indicates the optimal kernel cut value.

kernel cut. The significance obtained from the kernel optimisation (15.22σ) is seen to be greater than the result from the Supercuts optimisation (13.98σ), the gamma-ray rate is also slightly larger at 1.81 /min compared to 1.68 /min.

5.6 Flux Calculation

The analysis methods discussed in the previous sections are applied to observational data to determine the rate and significance of VHE emission. The detection rate is typically stated as counts per minute. However, to provide more useful physical information about the astrophysical source, the rate is converted into a flux, represented as counts per unit area per unit time.

In order to do this it is necessary to perform an exact calibration of the collector (i.e. the telescope and the gamma-ray selection technique), both in terms of its energy response and its collection area (Kertzman & Sembroski 1994). Neither is easily defined; the collection area, *A(E)*, increases as a function of

energy while the gamma-ray flux from an object decreases with increasing energy, thereby complicating the energy response of the detector. The collection area may be estimated directly from gamma-ray simulations but the energy response determination requires a priori knowledge (or assumptions) regarding the source gamma-ray spectrum, usually assumed to be a power-law spectrum.

The integral flux above a given energy threshold E_{th} is defined as:

$$\text{Flux}(E > E_{th}) = \frac{N}{T \times A_{eff}} \tag{5.15}$$

where N is the number of gamma rays detected in the time T and A_{eff} is the effective collection area of the telescope, which accounts for the gamma-ray detection efficiency post-analysis.

5.6.1 Effective Collection Area

The collection area of a Cherenkov telescope represents the area over which Cherenkov events trigger the telescope. The collection area provides a measure of the **efficiency** of gamma-ray detection over a range of energies. The collection area is much larger than the physical mirror size because Cherenkov photons from gamma-ray showers that reach the telescope are produced 5-20 km higher up in the atmosphere, depending on the primary energy. With a typical 3° field of view and a 10 km shower height, this corresponds to a theoretically possibly area in excess of 2×10^5 m^2 . However, this value is not attainable in practice and is typically reduced by up to a factor of 4, mainly because of light attenuation in the atmosphere.

To determine the collection area, gamma-ray-initiated air showers with impact distances up to 250 m were simulated. These simulations are those discussed previously in Section 5.5.3. An impact radius of 250 m relative to the telescope corresponds to an area of $A_o = \pi(250\text{ m})^2$. The collection area at a particular energy can be calculated by projecting a number of simulated showers ($N_{incident}$) over the area A_o, and counting the number of them which trigger the telescope

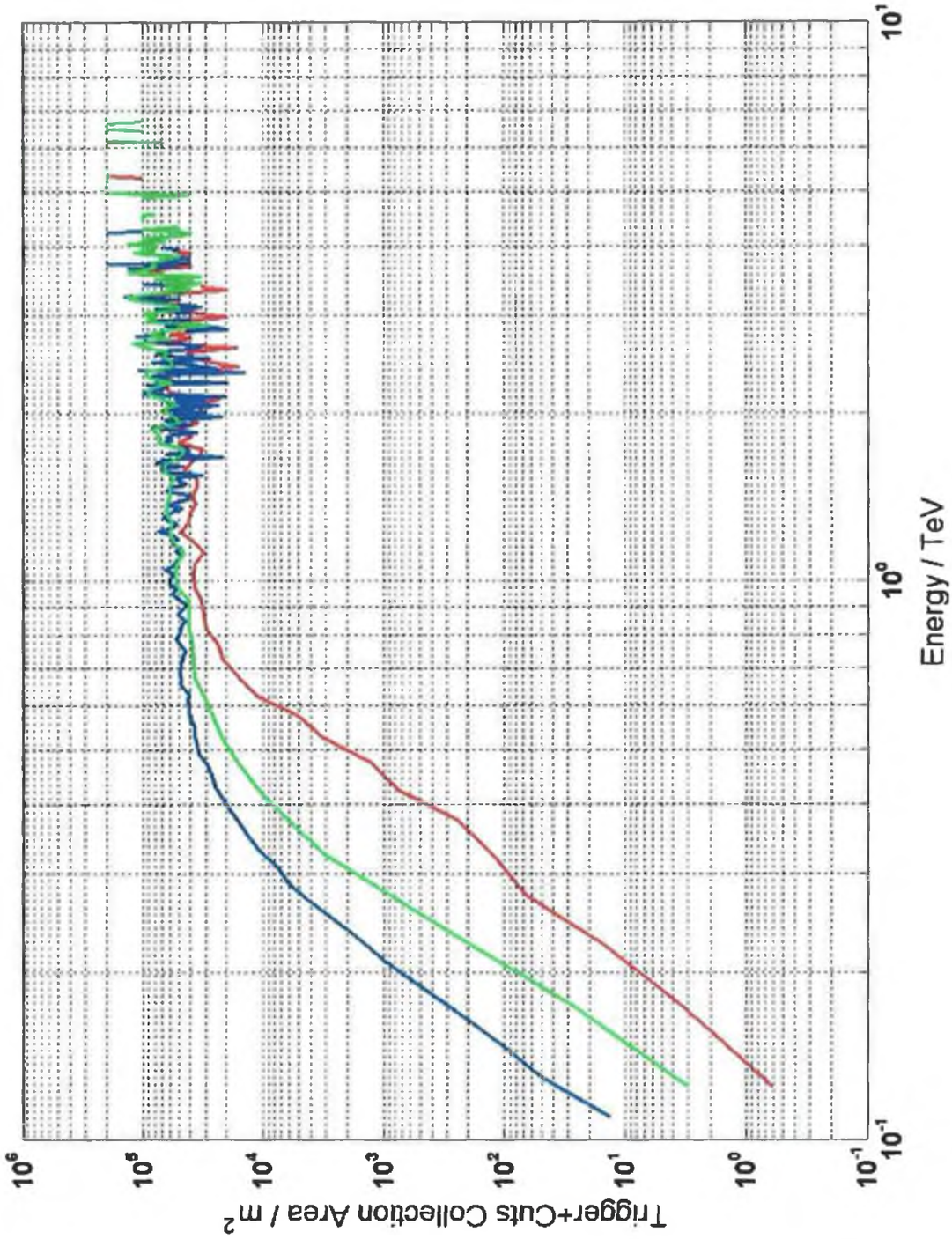

Figure 5.11: Collection area distributions for the Whipple 10m telescope after Supercuts 2000 (blue), kernel analysis (green) and Supercuts with a 0.8 TeV energy threshold (red). The distributions were calculated using gamma-ray simulations at 70° elevation from a Crab-like spectrum.

and pass the gamma-ray selection criteria ($N_{trigger+cuts}$). The collection area at that energy is given by:

$$A(E) = A_o \left(\frac{N(E)_{trig+cuts}}{N(E)_{incident}} \right) \tag{5.16}$$

The behaviour of the collection area as a function of energy, *A(E)*, is shown in Figure 5.11 for both the Supercuts and kernel methods. It is characterised by a initial steep increase corresponding to the instrumental threshold energy, followed by a more or less flat region where the source spectrum can be accurately determined. For Supercuts there is a gradual reduction at higher energies due to the upper distance cut which effectively restricts the maximum impact parameter at which Cherenkov images are accepted. Also note the large fluctuations beyond 1.5 TeV, a consequence of the sharply falling spectral index (α=-2.5), which results in a very low number of gamma rays being produced from the simulation process, even from a sample of 1.5 million events.

The collection area provides a measure of the sensitivity of the telescope to a uniform distribution of gamma rays at different energies. However, *A(E)* is not sufficient to characterise the response of the telescope to a particular gamma-ray source without incorporating the effect of the source spectrum. This is achieved by convolving the collection area curve with the source spectrum, resulting in a **differential response curve**:

$$\frac{dR}{dE} = A(E) \, . I_\gamma . E^{-\alpha} \tag{5.17}$$

where R is the gamma-ray rate, I_γ is the flux constant, and α is the differential spectral index. The differential response provides a measure of the true sensitivity of the collector to gamma rays from the source under observation.

Using the simulation database detailed in Section 5.5.3, collection area and energy threshold values were calculated. The energy thresholds were calculated assuming a Crab Nebula like spectrum, i.e. $I_\gamma . E^{-\alpha} = 3.20 \times 10^{-7} \times (E/\mathrm{TeV})^{-2.49}$

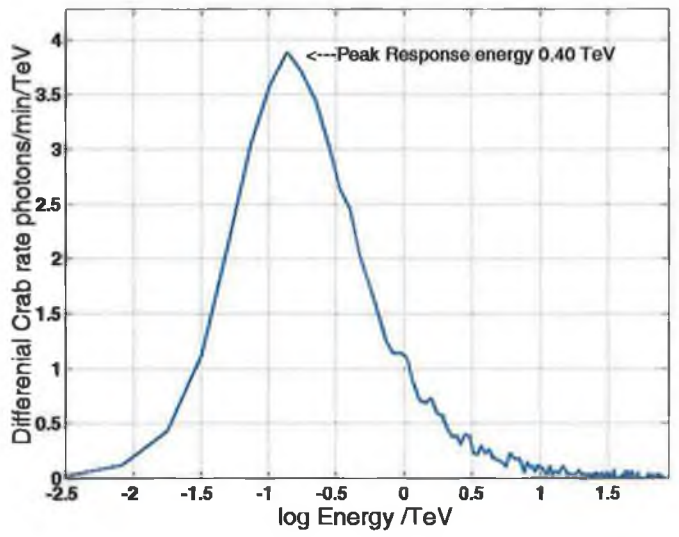

Figure 5.12: Differential response curve using 50000 simulated gamma-ray events describing the Whipple telescope response to a source with a Crab-like spectrum.

m^{-2} $s^{-1}TeV^{-1}$ (Hillas et al. 1998). The conventional definition of the **energy threshold** (E_{th}) is the point where the differential rate of gamma rays from the Crab Nebula reaches a maximum. This effectively occurs at the peak in the differential response curve (see Figure 5.12). Thus the conventional energy threshold is the collector's peak response energy (PRE) to a Crab-like spectrum.

The other parameter used in classifying the response of the telescope is the **effective collection area** (A_{eff}). This can be derived in terms of the collection area function $A(E)$ using a method similar to that of Kertzman & Sembroski (1994):

$$R(> E_{th}) = \int_{E_{th}}^{\infty} A(E) I_\gamma E^{-\alpha} dE = A_{eff} \int_{E_{th}}^{\infty} I_\gamma E^{-\alpha} dE \tag{5.18}$$

Rearranging we have an expression for the effective area:

$$A_{eff} = \frac{R(> E_{th})}{Flux(> E_{th})} = \frac{\int_{E_{th}}^{\infty} A(E) I_\gamma E^{-\alpha} dE}{\int_{E_{th}}^{\infty} I_\gamma E^{-\alpha} dE} \tag{5.19}$$

This calculation is effectively a division of the area under the differential

response curve by the area under the source spectrum, from the energy threshold upwards. For the Supercuts 2000 selection criteria, the effective area was found to be $(3.98 \pm 0.12) \times 10^4$ m^2.

5.6.2 Upper Limits

If analysis of a source results in a non-detection (i.e., if the excess is not statistically significant), there remains the possibility of imposing upper limits on the gamma-ray flux. One such method to impose an upper restriction on the flux is to:

- calculate a 99.9% confidence level (C.L.) upper limit on the count rate using the method of Helene (1984),
- express the counts upper limit as a fraction of the Crab Nebula count rate for the same season (this corrects for season-to-season variations in factors like the PMT gain and mirror reflectivity which effect the telescope response, and therefore its gamma-ray count rate),
- convert to a flux upper limit by assuming a Crab-like spectrum with effective collection area A_{eff}.

The Helene method calculates the probability density function of the number of source events based on the number of events in the ON and OFF data. Using the probability density function it it possible to determine the maximum number of events coming from the source with a given confidence level, assuming statistical fluctuations only. In practice, the upper limit N_{ul} on the number of counts is calculated iteratively by numerically solving the equation:

$$1 - CL = \frac{I\left(\frac{(N_{ul}-N)}{\sigma}\right)}{I\left(\frac{-N}{\sigma}\right)} \tag{5.20}$$

where CL is the desired confidence level (0.999), N_{ul} is the upper limit on the number of counts, N is the excess number of events ($N_{ON}-N_{OFF}$), σ is $\sqrt{N_{ON}+N_{OFF}}$

and *I(z)* is the error function:

$$I(z) = \frac{1}{\sqrt{2\pi}} \int_z^{\infty} e^{\frac{-x^2}{2}} dx \tag{5.21}$$

To convert the counts upper limit to a flux upper limit, an intermediate step is applied whereby the counts upper limit is converted to an upper limit of the gamma-ray rate in terms of the average rate from the Crab Nebula for the same season the source exposure time t:

$$UL_{c.u.} = \frac{N_{UL}/_t}{rate_{Crab}} \tag{5.22}$$

This upper limit in Crab units can then be converted into an absolute flux above the energy threshold of the telescope by assuming a Crab-like spectrum.

$$UL_{abs} = UL_{c.u.} \times F_{Crab} \tag{5.23}$$

where F_{Crab} is the Crab Nebula integral flux above the energy threshold of the telescope for the relevant season. This flux upper limit calculation takes advantage of the fact that the VHE Crab Nebula flux is steady over at least a 7-year period so that changes in the Crab Nebula count rate are most likely due to changes in the telescope sensitivity or threshold (Hillas et al. 1998; Aharonian et al. 2004a).

Chapter 6

VHE Gamma-ray Observations of the Blazar 1ES 2344+514

The analysis methodology described in the previous chapter was applied to determine the VHE gamma-ray flux of the blazar 1ES 2344+514 during the period 1999-2004. The analysis results are presented in Section 6.2.1. First a synopsis of the multi-wavelength history of 1ES 2344 is adumbrated.

6.1 History and Source Overview

1ES 2344+514 was first detected in the energy range 0.2-4 keV by the Einstein Slew Survey[1] (Elvis et al. 1992). This survey was constructed from data collected during the space-based Einstein mission from 1978 to 1981. Subsequent observations at all wavelengths showed 1ES 2344+514 to be an unresolved point source with observed characteristics as follows:

- the host galaxy of 1ES 2344 is elliptical with a half-width half-maximum radius of $r_e = 7.12 \pm 0.02$ kpc, assuming H_0 =50 km s^{-1}Mpc^{-1} and q_0=0 (Urry et al. 2000)

[1]The designation '1ES 2344+514' indicates a source in the 1^{st} Einstein catalogue with RA 23h44m36.26s and Dec 51d25m37.4s using J1950 (Patnaik et al. 1992).

- redshift 0.044
- central black hole of mass $10^{8.80\pm0.16} M_{\odot}$ derived from stellar velocity dispersion measurements (Barth et al. 2003)
- a distinctive radio/optical/x-ray flux (Stocke et al. 1990)
- non-thermal emission which almost completely masks the thermal emission from the surrounding host galaxy
- the absence of emission lines with observed equivalent width greater than 0.5 nm, which suggests that the source is not a quasar
- a continuum break strength (CBS), the relative depression of the continuum below 400 nm in the rest frame, smaller than 25% (Perlman et al. 1996). This is indicative of a power law spectrum.

Based on these properties 1ES 2344 is classified as a **BL Lac** object.

6.1.1 Radio and Optical Observations

The earliest radio data were obtained by the University of Texas Radio Astronomy Observatory at 365 MHz during a sky survey from 1974-1983 (Douglas et al. 1996). Radio observations followed at 1.4 GHz in 1983, at 4.85 GHz in 1987 and at 8.4 GHz in 1990 by the Very Large Array (Condon & Broderick 1985; Perlman et al. 1996; Patnaik et al. 1992).

In the optical and far-infrared, observations of 1ES 2344 are masked by the thermal emission from the host galaxy. Observations with the Hubble Space Telescope in 1996 measured a R-band brightness of the nucleus of 16.83 ± 0.05 mag from a fit of a point source plus galaxy convolved with the point-spread function of the telescope (Urry et al. 2000). During continued monitoring through 1998, optical variability was evident with the R-band brightness varying from 16.47 mag (Nilsson et al. 1999) to 17.00 mag (Falomo & Kotilainen 1999). An optical

monitoring program in 2000-2001 found short-timescale variability to be weak, with maximum intra-day variability of $\Delta V = 0.18$ mag, including galaxy light (Xie et al. 2001) . A relatively large brightness decrease of 0.35 mag was observed in the V-band over 2 weeks in January 2001.

6.1.2 X-ray Observations

1ES 2344 showed rapid x-ray variability on a time scale of hours in the 0.1-10 keV energy band during a week-long campaign of observation by the BeppoSAX satellite in 1996 (Giommi et al. 2000). A follow-up observation in 1998 found 1ES 2344 to be in a very low state, implying a frequency shift of the peak synchrotron emission by a factor of 30 or more. This suggested the interpretation that two distinct electron populations contribute to the synchrotron emission, one a steady low-energy component, the other extending from soft to hard x-rays with rapid time variability. During the 1996 x-ray campaign, near-simultaneous VHE observations at the Whipple observatory of 25 hours did not result in a detection. The peak response for most sources detected with EGRET lies at around 300 MeV (Hartman et al. 1999); an upper limit at 300 MeV of about 3.4×10^{-11} erg cm^{-2} was derived by Schroedter (2004).

6.1.3 Previous Reports of VHE Gamma-ray Emission

VHE gamma rays were first detected from 1ES 2344 on the night of 20 December 1995, with a significance of 5.3 σ. This has been the strongest VHE emission measured from this object to date. The detection was made by the Whipple collaboration, and reported at the 1997 International Cosmic Ray Conference (Catanese et al. 1998). The flare data consists of 3 ON/OFF pairs and 1 tracking run with a total of 110 minutes ON-source, summarized with a lightcurve shown in Figure 6.1. The signal was considered tentative because follow-up observations through 1997 did not detect further evidence for emission, nor had other observatories reported the object to be in a high state.

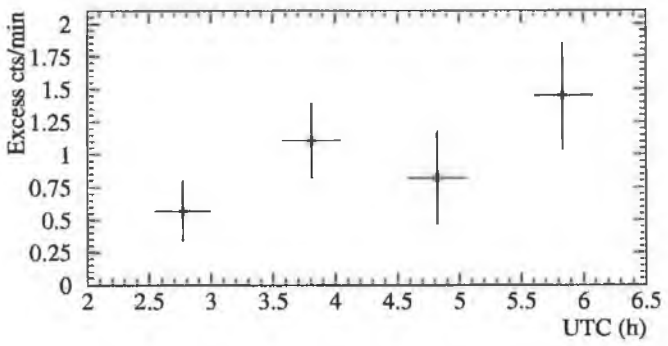

Figure 6.1: 1ES 2344 flare light curve from VHE observations on 20 December 1995 (Catanese et al. 1998).

Monitoring from 1998 to 2000 using the Whipple telescope resulted in an exposure of 24 hours showing a small positive excess of 3.1σ (Badran et al. 2001). This data consisted of tracking runs only, and thus is subject to systematic effects arising from the use of a tracking ratio. Based on observations totalling 24 hours during 1997 and 1998, the HEGRA experiment reported a significance of 3.3σ (Konopelko 1999a). Subsequent HEGRA observations in 2002, combined with the 1997/1998 data for a total of 72.5 hours ON-source, resulted in a positive detection with significance 4.4σ at a integral flux level above 800 GeV of $(0.08\pm0.03)\times10^{-7}$ photons.m^{-2}.s^{-1} (Tluczykont 2003). This result definitively confirmed 1ES 2344 as a source of VHE emission. A summary of the VHE observations to date is given in Table 6.1.

Date	**Reference**	**Exposure [hrs]**	**S**^{a} $[\sigma]$	**Integral Flux** $[\times10^{-7}\mathrm{m}^{-2}\mathrm{s}^{-1}]$	**E**$_{thresh}$ **[TeV]**
1995/1996	Catanese et al. (1998)	20.5	5.8	1.7±0.5	0.35
20 Dec 95	Catanese et al. (1998)	1.85	5.3^b	6.6 ±1.9	0.35
1996/1997	Catanese et al. (1998)	24.9	0.4	$< 0.82^c$	0.35
1998	Konopelko (1999a)	23.4	3.3	$< 0.09^d$	1.0
2000	Badran et al. (2001)	24	3.1	1.1±0.1^e	≈ 0.4
1997-2002	Tluczykont (2003)	72.5	4.4	0.08±0.03	0.8

Table 6.1: VHE measurements of 1ES 2344. ^{a}Statistical excess, ^{b}part of the data used in the above entry, ^{c}99.9%C.L. upper limit, ^{d}99% upper limit, ^{e} statistical error only.

6.2 Investigation of TeV Emission from 1ES 2344 between 1999 and 2004

Since the original 1995/1996 detection, the VERITAS collaboration has regularly monitored 1ES 2344. Observations up to 2000 were reported by Badran et al. (2001). The work presented here considers all 1ES 2344 observations using the Whipple 10m telescope from 1999 to 2004, with a view to assessing the activity of the source during this period. The motivation to perform this multi-seasonal analysis was boosted given that this object was confirmed as a source of TeV radiation by the HEGRA observations.

The database comprises 141 $\times$ 28 minute observations from September 1999 to May 2004, recorded in good weather, with steady cosmic ray rate and at elevations $> 55°$. The total time of the exposure is 64.5 hours. Information regarding the seasonal raw data is shown in Table 6.2.

Period	No. of ON-runs	Raw ON events
1999/2000	15	527124
2000/2001	60	4708168
2001/2002	27	2305210
2002/2003	10	514521
2003/2004	29	2032897
Total	141	10087920

Table 6.2: 1ES 2344 raw data, showing the total number of events recorded in each season.

Only 10 of the total 141 observations were taken in ON/OFF mode, leaving the remaining 131 without the necessary OFF-runs to make a reliable flux estimate. The matching method described in the previous chapter was therefore used to partner these tracking runs with the most compatible control observations. The matching process identifies the most suitable control run (i.e. an OFF-run from another source) for a given ON-source observation, based on a set of parameters describing the run (elevation, throughput, mean sky noise, pixels turned off, and the date of observation). Software padding (discussed in Sec-

tion 5.2.1) was applied to the entire data set. The resulting parameterised data set was then subjected to the discrimination criteria of Supercuts and kernel analysis, as described in Chapter 5.

6.2.1 Supercuts Analysis Results

Table 6.3 displays the season-by-season results after application of Supercuts 2000. The camera configuration was stable over the entire period 1999 to 2004, with the same number of central pixels and similar discriminator levels, making it possible to apply consistent cuts (Table 5.1). The energy threshold of the telescope varies slightly from year to year, due to changes in mirror reflectivity and changes in the electronic gain. The average energy threshold after cuts was calculated to be 400 GeV; the threshold energies for individual seasons are given in Table 6.4.

Although the overall significance from the 141 pairs is less then 3σ, the detected rate is considered to constitute a real signal, given that the source has being confirmed as a VHE emitter. However, because the significance for each season are all individually below 2σ, upper limits on the gamma-ray flux have also been calculated (see Table 6.4).

Period	Exposure /min.	ON	OFF	Sigma	Rate /min
1999/2000	418.95	1221	1267	-0.763	-
2000/2001	1612.88	11285	10986	1.736	0.186±0.107
2001/2002	750.04	3998	3845	1.525	0.203±0.133
2002/2003	278.79	801	799	0.034	0.006±0.163
2003/2004	808.71	4390	4344	0.437	0.057±0.131
Total	3.86×10^3	21695	21259	2.104	0.113±0.054

Table 6.3: 1ES 2344 data after application of Supercuts 2000.

As part of the matching procedure, a scaling factor was applied to the OFF-data for each season to account for residual differences between ON and matched OFF data. This involves scaling the ON and OFF alpha plots to match in the 20° to 65° region. The significance and rate are then calculated using Equation 5.6

and Equation 5.7, respectfully, including the uncertainties associated with the scaling process. The resulting increased uncertainty on the excess, after scaling, contributes to diminished significance levels and a greater uncertainty on the gamma-ray rates. However, in the combined dataset of all five seasons, a scaling factor was not required as the 20° to 65° region for the ON and matched-OFF data were in very close agreement (Figure 6.2). The significance and rate were thus calculated as normal using Equation 5.2.

The alpha distribution for the entire data set is shown in Figure 6.2. For each of the seasons with substantial datasets (> 12 hrs ON-source), there is an indication of an excess at small α angles (see Figures 6.4, 6.5, 6.6).

Period	**Rate** [**Crab**]	**Flux** [$\times 10^{-7}\mathbf{m}^{-2}\mathbf{s}^{-1}$]	**Flux Upper Limit** [$\times 10^{-7}\mathbf{m}^{-2}\mathbf{s}^{-1}$]	$\mathbf{E}_{Thresh}$ [TeV]
1999/2000	-	-	< 0.501	0.500
2000/2001	0.063	0.576	< 1.20	0.378
2001/2002	0.072	0.632	< 1.43	0.389
2002/2003	0.002	0.019	< 1.06	0.420
2003/2004	0.021	0.175	< 0.99	0.303

Table 6.4: 1ES 2344 rates for different seasons in units of the average contemporary Crab rate together with integral fluxes and 99.9% C.L. upper limits.

The rates for individual seasons in Crab units and the corresponding integral flux values above the energy threshold are presented in Table 6.4. The flux upper limits calculated at the 99.9% confidence level using the method described in Section 5.6.2 are also included. The flux results are presented graphically as a lightcurve in Figure 6.3.

The plot shows no evidence for long term variability: the fluxes for each season agree with the average within the error bars. Investigation of the flux for increasingly shorter timescales, down to individual nights, showed no indication of any flaring activity.

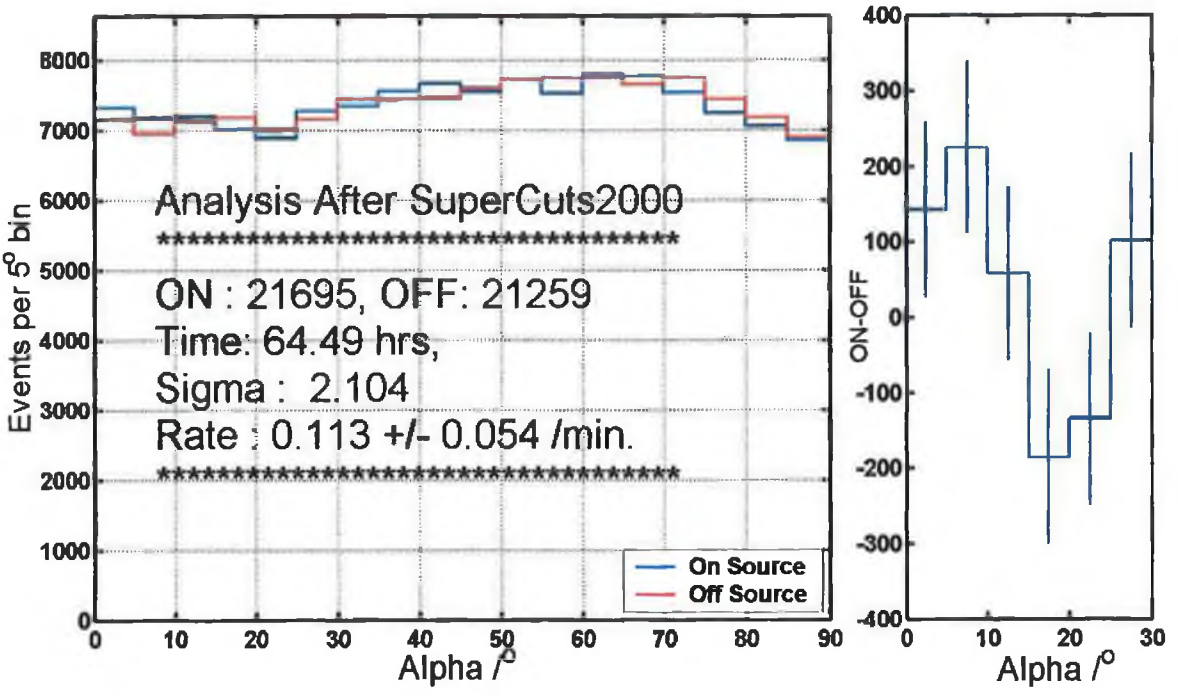

Figure 6.2: Overall alpha plot for 141 1ES 2344 pairs, after application of Supercuts 2000. The right panel shows alpha ON-OFF.

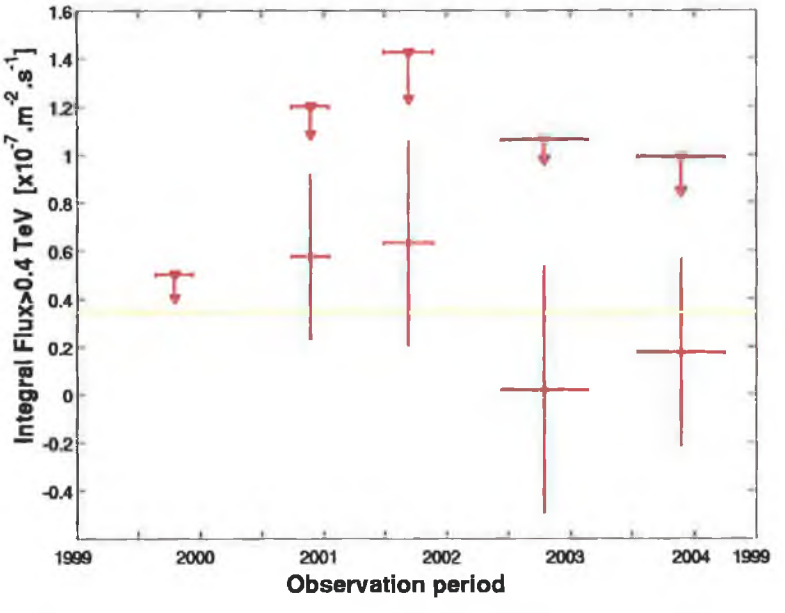

Figure 6.3: 1ES 2344 lightcurve with integral flux and 99.9% C.L. flux upper limits for each season. The average flux is indicated by the yellow line.

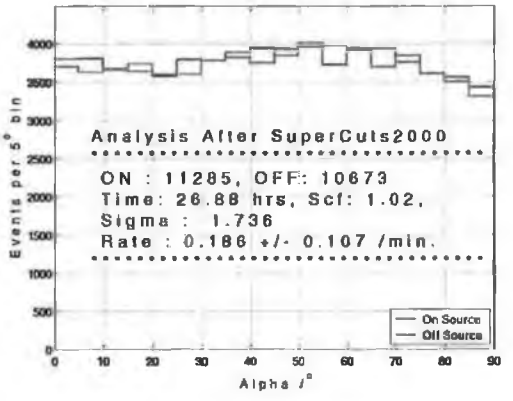

Figure 6.4: The alpha plot for 60 1ES 2344 pairs from the 2000/2001 season, after application of Supercuts 2000.

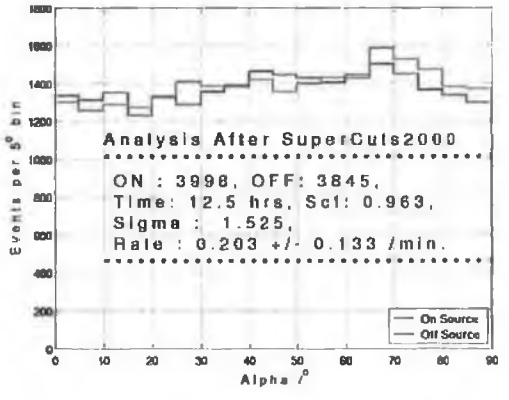

Figure 6.5: The alpha plot for 27 1ES 2344 pairs from 2001/2002, after application of Supercuts 2000.

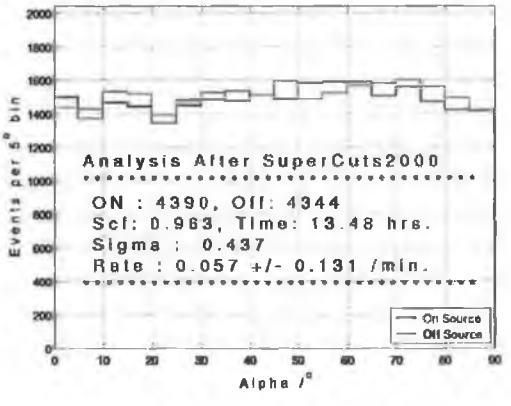

Figure 6.6: The alpha plot for 29 1ES 2344 pairs 2003/2004, after application of Supercuts 2000.

6.2.2 Kernel Analysis

The kernel procedure was applied to the overall data set and subsets. However, the behaviour was found to be somewhat unstable, often producing results for pairs which were at variance with those obtained using the Supercuts approach. This behaviour has already been noted by Gammell (2004), who attributed it to systematic effects associated with the selection of the OFF-runs.

Since the kernel procedure does not apply any lower energy cut, its performance may be susceptible to small differences, such as sky brightness, between data-sets, particularly for events near the energy threshold of the telescope, where these effects are likely to be more pronounced. In the case of the matched pairs, the likelihood of small differences between ON and OFF runs is much higher than in real pairs. This may provide an explanation for the instability of the kernel analysis in the current work.

However, artificially raising the energy threshold (by applying a lower size cut in the kernel analysis) did not appear to make any significant improvement. This suggests that much more detailed investigation of the kernel technique is required before it can be applied in the case of weak sources with matched data.

6.3 Discussion of Results

The overall result from the Supercuts analysis of 1ES 2344 showed a significance of 2.1σ. An earlier analysis of a subset of this data performed by Badran et al. (2001) showed a greater significance of 3σ. There are a number of factors which may account for the difference between these results. Firstly, the data analysed by Badran et al. (2001) consisted almost entirely of tracking runs, and for reasons reported in Section 3.8.3 there is a greater uncertainty in the tracking ratio, particularly in the case of 1ES 2344 where there are many bright stars in the field of view. Secondly, Badran et al. (2001) re-optimised the picture/boundry and parameter cut values on the basis of a combination of rate and significance

rather than on the latter alone; an untested procedure which may not be entirely reliable. Since then this method has not been used by the Whipple collaboration in the presentation of any other results.

To make a comparison with the quiescent flux as determined by HEGRA, the 1ES 2344 data set was analysed at the corresponding energy threshold of 800 GeV. This was achieved by including a non-zero size cut in the discrimination process. To determine the appropriate lower size limit an incremental size cut was applied to the simulation data until the energy distribution was found to peak at 800 GeV; a size cut of 1020 digital counts was chosen (Figure 6.7). The integral flux above 800 GeV was calculated using an effective area at that threshold of $(3.50 \pm 0.35) \times 10^4$ m^2.

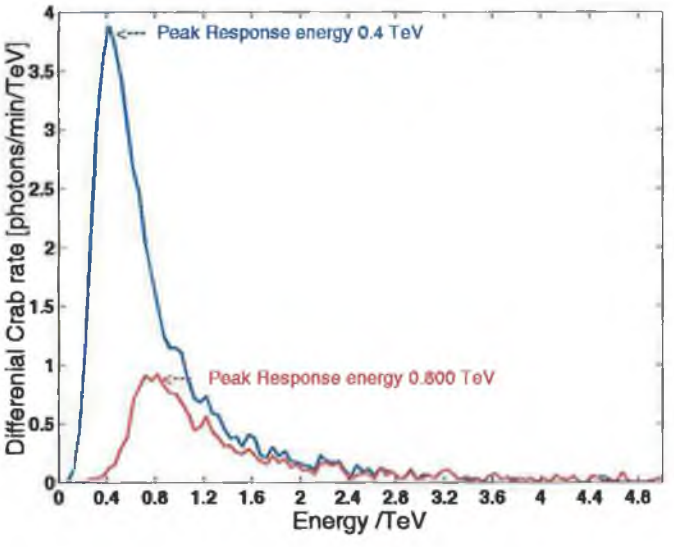

Figure 6.7: Peak response curves for simulated gamma rays after application of Supercuts 2000 (peak response energy 0.4 TeV) and with addition of lower size cut 1020 d.c. (peak response energy 0.8 TeV).

Table 6.5 shows the resulting flux values and flux upper limits for energy thresholds of 400 GeV and 800 GeV. It is noted that the flux above 800 GeV compares very well with the HEGRA value of $(0.08 \pm 0.03) \times 10^{-7}\mathrm{m}^{-2}\mathrm{s}^{-1}$. The uncertainties however differ by a factor of two, even though the total exposure

times are comparable: this may be attributed to the increased background rejection possible using the stereoscopic arrangement of the HEGRA experiment. With comparable observing times one can clearly reason that HEGRA, detecting 1ES 2344 with an overall significance of 4.4σ, operated with much better sensitivity when compared with the Whipple 10m system. Indeed the sensitivity of the HEGRA system to the Crab Nebula ($10\ \sigma/\sqrt{hr}$) is almost double that achieved by the Whipple experiment ($5.5\ \sigma/\sqrt{hr}$).

Period	**Sigma** $[\sigma]$	**Rate** $[\gamma/\mathbf{min}]$	**Flux** $[\times 10^{-7}\mathbf{m}^{-2}\mathbf{s}^{-1}]$	**Flux Upper Limit** $[\times 10^{-7}\mathbf{m}^{-2}\mathbf{s}^{-1}]$	$\mathbf{E}_{Thresh}$ [TeV]
1999-2004	2.10	0.070	0.29 ± 0.14	<0.56	0.40
1999-2004	1.72	0.013	0.07 ± 0.04	<0.21	0.80

Table 6.5: 1ES 2344 integral fluxes calculated at 400 GeV and 800 GeV for the entire Whipple data set. Flux upper limits are also given at the 99.9% C.L.

A lightcurve combining the fluxes from the HEGRA and the Whipple observations from 1997 to 2004 is shown in Figure 6.8. The HEGRA fluxes for 1997, 1998 and 2002 were calculated from values given in Tluczykont (2003), using an effective area of 3.02×10^4 m^2. For the 2002-2003 season, where there are observations from both experiment, there is good agreement, although the error bars are large. While the difference between the results may be largely statistical in nature, there are also systematic effects due to source variability and in the positioning of the Whipple energy threshold to match that of HEGRA. Overall the combined results from both experiments are consistent with a steady flux above 800 GeV of 0.08×10^{-7} m^{-2} s^{-1} over the entire period 1997-2004.

Assuming that the emission follows a power-law spectrum, with differential flux proportional to $E^{-\alpha}$, the ratio of the integral flux values in Table 6.5 can be used to obtain an estimate of the spectral index α, using

$$\left(\frac{E_1}{E_2}\right)^{-\alpha+1} = \left(\frac{F(>E_1)}{F(>E_2)}\right) \tag{6.1}$$

The flux results imply a spectral index of $\alpha = 3.0\pm^{0.9}_{2.5}$ (statistical error only).

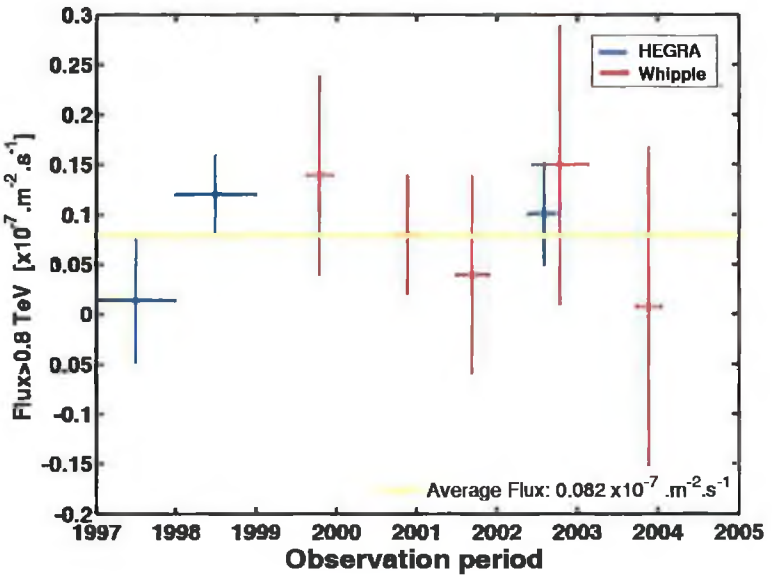

Figure 6.8: Combined 1ES 2344 lightcurve from 1997 to 2004. Both the Whipple and HEGRA fluxes above 0.8 TeV are shown, with the average flux indicated in yellow.

The recent determination by Schroedter (2004) of the spectrum of 1ES 2344 during the strong flare of December 1995 yielded a value of 2.54 ± 0.17 for the spectral index.[2] Schroedter (2004) employed effectively the same matching procedure in the analysis of the 1997 flare data.

The simulations employed throughout this work were generated with a Crab-like spectrum with index of 2.5. While this is a reasonable approximation given that the flare spectrum for 1ES 2344 shows an index of $\sim$ 2.5, the low-flux spectral index may indeed be different. This approximation may have introduced systematic effects associated with the calculation of the effective collection area and thus the integral flux values at the 400 GeV and 800 GeV energy thresholds. The systematic effects are likely to be smaller than the statistical uncertainties quoted above. Due to this large uncertainty on the flux values the spectral index for the low flux emission must be regarded as entirely consistent with the spectral

[2]The flare spectrum of 1ES 2344 between 0.8 TeV and 12.6 TeV: $\frac{dN}{dE\,dA\,dt} = (5.1 \pm 1.0_{st} \pm 1.2_{sy}) \times 10^{-7} E^{-2.54 \pm 0.17_{st} \pm 0.07_{sy}} \mathrm{TeV}^{-1}\mathrm{m}^{-2}\mathrm{s}^{-1}$ (from Schroedter (2004)).

index measured for the flaring state.

However, it is interesting that the flare spectrum appears to be harder than the spectrum during the low-level activity documented in this study and in the HEGRA results. This is consistent with the observation of the bright flares of Mrk 421 and Mrk 501 which have shown that on average the VHE spectrum becomes harder with increasing flux level (Krennrich et al. 2002; Aharonian et al. 2002b). It is possible that this is a common trend in the behaviour of blazars. In the context of electron synchrotron models, such behaviour would indicate that in flaring activity not only does the electron density increase, but that the electrons are also accelerated to higher energies. This is consistent with x-ray observations of a shift in the synchrotron peak to higher energy.

The flare spectrum of 1ES 2344 is similar to that of 1ES 1959+650, which is located at a similar distance, steeper than the brightest flare spectra of Mrk 421 and Mrk 501, both located at a distance about half that of 1ES 2344, and harder than the spectra of PKS 2155-304 and H 1426+428, which are located almost three times as far away. This trend is consistent with attenuation caused by the infrared extragalactic background radiation where a steepening of the spectral index is expected with increasing source distance (Schroedter 2005).

6.4 Conclusions

1ES 2344 is an exceptional object. It has being confirmed as a TeV emitter based on the 1995 flare and the HEGRA observations from 1997 to 2002, and has thus been detected over nearly 18 orders of magnitude in energy, from radio to VHE. Figure 6.3 shows the broadband spectral energy distribution of 1ES 2344 in the form of a νF_ν plot, with the inclusion of the integral fluxes above 0.4 TeV and 0.8 TeV obtained from this work.

VHE blazars are generally characterised by extreme variability in the TeV energy range. 1ES 2344 may be somewhat unusual in this respect since there has only been one VHE flare from this object in the last ten years of observa-

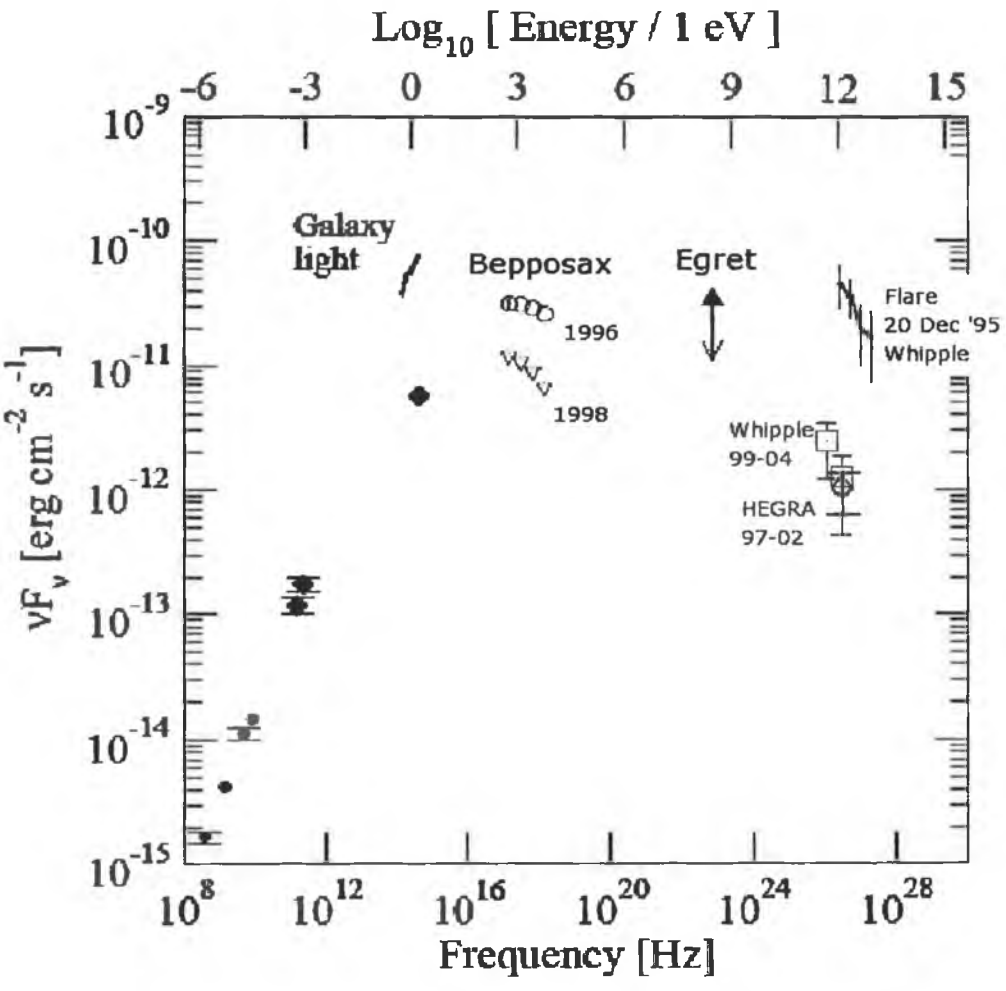

Figure 6.9: 1ES 2344 Spectral Energy Distribution. Data taken from the following sources: 365 MHz from Texas radio survey (Douglas et al. 1996), 1.4 GHz from Greenbank (Becker et al. 1993), 4.85 GHz from Greenbank (Gregory et al. 2000), 8.4 GHz from VLA (Patnaik et al. 1992), galaxy photometry at millimeter wavelength from (Stevens & Gear 1999), galaxy photometry at K, H, and J-bands from 2MASS (Jarrett et al. 2003), galaxy and nucleus R-band photometry obtained with Hubble Space Telescope and corrected for interstellar reddening (Urry et al. 2000). X-ray observation by BeppoSAX (Giommi et al. 2000), upper limit at 300 MeV from EGRET (Hartman et al. 1999). VHE flare spectrum obtained with the Whipple telescope. Quiescent VHE gamma-ray flux during the period 1997-2002 from HEGRA (Tluczykont 2003). The results from this analysis are indicated as Whipple 99-04.

tion. During this episode the flux was seen to increase by up to a factor of 20 compared to its quiescent state. All of the other blazars in the TeV catalog have demonstrated flaring activity more frequently than 1ES 2344. Overall, 1ES 2344 can justifiably be called an extreme galaxy, or at least an extreme example of the class of TeV blazars.

The spectra of the blazars Mrk 421 and Mrk 501 have been observed to harden during periods of flaring activity. In the case of 1ES 2344+514, the quiescent spectral index was estimated in this work to be $\alpha \sim 3$, compared to the flaring state where $\alpha \sim 2.5$. However, measurement of the low-level flux activity at a higher significance is clearly needed if a strong statement about the shape and extent of its TeV and broad-band emission is to be made; at present the uncertainties involved are simply far too large.

It is presumed that one can infer the diffuse extragalactic background indirectly by measuring the expected TeV cutoff in the spectra of VHE sources. At this stage, with more extragalactic TeV detections, the estimates and upper limits placed on the infrared photon density are becoming progressively constrained. Detection of TeV emission from other objects at large redshifts is highly desirable in order to assess the impact of intergalactic absorption on deformation of the intrinsic gamma-ray spectra. A broader understanding of the intrinsic emission spectrum of TeV blazars will allow the absorption effects of the EBL to be defined more accurately.

If TeV blazars share common intrinsic emission behaviour, evaluation of the EBL based on flare spectra may be unreliable since the intrinsic characteristics of these objects are greatly altered during flaring episodes. It is thus clear that the low-level emission from TeV blazars warrants further investigation. Hitherto, the spectral behaviour and the correspondence between x-ray and TeV observations have been examined in detail only during strong flaring episodes. Since the indications are that the spectra in that case are modified by transient conditions within the blazar jet, a comprehensive study of the behaviour at low flux levels may be

essential to obtaining reliable information about the cosmic infra-red background. In the past, such low flux investigations have been impractical due to the very long exposures required to derive spectra with sufficient precision (as evidenced by the present study). With the advent of atmospheric Cherenkov telescope arrays, spectra information can be obtained on more manageable timescales, allowing the behaviour of blazars at low flux levels to be examined and compared.

The HEGRA experiment which operated from 1997 to 2002 on La Palma pioneered and proved the value of the multiple Cherenkov telescope technique. A comparison of the quiescent flux of 1ES 2344 as determined from this work and by HEGRA clearly demonstrates that with simultaneous observations from multiple telescopes, a much improved background rejection is possible, yielding results with smaller uncertainties. This has been dramatically demonstrated by the H.E.S.S. array in Namibia, which has achieved unprecedented sensitivity. The impact of this increased sensitivity has already been shown by the high-significance detection of eight new galactic TeV sources (Aharonian et al. 2005b) and the detection for the first time of VHE emission from the blazar PKS 2005-489 (Aharonian et al. 2005c).

In the northern hemisphere, the telescope array being built by the VERITAS Collaboration will achieve a similar level of performance. We can expect that the quiescent behaviour of 1ES 2344 and other blazars which demonstrate extreme levels of emission will be elucidated in more detail. It can be anticipated that such studies will lead to important insights both in relation to the internal mechanisms at work in blazar jets and in the wider context of the effects which modify blazar spectra external to the source.

Appendix A

Definition of the Hillas parameters

Suppose the i^{th} PMT is given coordinates x_i, y_i (in degrees) and registers a signal S_i. The origin of the coordinate system is in the centre of the array of PMTs. An ellipse is fitted to the image and the Hillas parameters are calculated relative to the centre. For a graphical description of the parameters see Figure 5.1. The major axis of the ellipse is expressed by the equation y = ax + b. The fitting of the ellipse employs the following simple moments:

$$\langle x \rangle = \frac{\sum s_i x_i}{\sum s_i},$$
$$\langle y \rangle = \frac{\sum s_i y_i}{\sum s_i},$$
$$\langle x^2 \rangle = \frac{\sum s_i x_i^2}{\sum s_i},$$
$$\langle y^2 \rangle = \frac{\sum s_i y_i^2}{\sum s_i},$$
$$\langle xy \rangle = \frac{\sum s_i x_i y_i}{\sum s_i},$$
$$\langle x^3 \rangle = \frac{\sum s_i x_i^3}{\sum s_i},$$
$$\langle y^3 \rangle = \frac{\sum s_i y_i^3}{\sum s_i},$$
$$\langle x^2 y \rangle = \frac{\sum s_i x_i^2 y_i}{\sum s_i},$$
$$\langle xy^2 \rangle = \frac{\sum s_i x_i y_i^2}{\sum s_i},$$

and

$$\sigma_{x^2} = \langle x^2 \rangle - \langle x^2 \rangle ,$$
$$\sigma_{y^2} = \langle y^2 \rangle - \langle y^2 \rangle ,$$
$$\sigma_{xy} = \langle xy \rangle - \langle x \rangle \langle y \rangle ,$$
$$\sigma_{x^3} = \langle x^3 \rangle - 3 \langle x \rangle \langle x^2 \rangle + 2 \langle x \rangle^3 ,$$
$$\sigma_{y^3} = \langle y^3 \rangle - 3 \langle y \rangle \langle y^2 \rangle + 2 \langle y \rangle^3 ,$$
$$\sigma_{x^2y} = \langle x^2 y \rangle - 2 \langle xy \rangle \langle x \rangle + 2 \langle x \rangle^2 \langle y \rangle - \langle x^2 \rangle \langle y \rangle ,$$
$$\sigma_{xy^2} = \langle xy^2 \rangle - 2 \langle xy \rangle \langle y \rangle + 2 \langle x \rangle \langle y \rangle^2 - \langle x \rangle \langle y^2 \rangle ,$$

Given the following definitions:

$$k = \sigma_{y^2} - \sigma_{x^2},$$
$$l = \sqrt{k^2 + 4\sigma_{xy}^2},$$
$$m = \langle y^2 \rangle - \langle x^2 \rangle ,$$
$$n = \sqrt{m^2 + 4 \langle xy \rangle^2},$$
$$u = 1 + \frac{k}{l},$$
$$v = 2 - u,$$

the Hillas parameters are calculated from:

$$\langle Size \rangle = \sum s_i,$$
$$\langle Length \rangle^2 = \frac{\sigma_{x^2} + \sigma_{y^2} + 1,}{2}$$
$$\langle Width \rangle^2 = \frac{\sigma_{x^2} + \sigma_{y^2} - 1,}{2}$$
$$\langle Miss \rangle^2 = \frac{u\langle x \rangle^2 + v\langle y \rangle^2}{2} - \frac{2\langle xy \rangle \sigma_{xy}}{l},$$
$$\langle Azwidth \rangle^2 = \frac{\langle x \rangle^2 + \langle y \rangle^2 - n}{2},$$
$$\langle Dis\tan ce \rangle^2 = \langle x \rangle^2 + \langle y \rangle^2 ,$$
$$\langle Alpha \rangle = \sin^{-1} \left(\frac{\langle Miss \rangle}{\langle Dis\tan ce \rangle} \right) ,$$

The calculation of the parameter asymmetry requires the angle, ψ, between the

Bibliography

Aharonian, F., et al. 2002a, *Astronomy and Astrophysics*, 384, L23

Aharonian, F., et al. 2002b, *Astronomy and Astrophysics*, 393, 89

Aharonian, F., et al. 2003, *Astronomy and Astrophysics*, 406, L9

Aharonian, F., et al. 2004a, *Astrophys. J.*, 614, 897

Aharonian, F., et al. 2004b, *Nature*, 432, 75

Aharonian, F., et al. 2004c, *Astronomy and Astrophysics*, 425, 13

Aharonian, F., et al. 2005a, *Astronomy and Astrophysics* (submitted)

Aharonian, F., et al. 2005b, *Science*, 307, 1938

Aharonian, F., et al. 2005c, *Astronomy and Astrophysics* (submitted)

Amenomori, M., et al. 1999, *Astrophys. J. Lett.*, 525, L93

Antonucci, R. 1993, *Ann. Rev. Astron. Astrophys.*, 31, 473

Antonucci, R. R. J., & Miller, J. S. 1985, *Astrophys. J.*, 297, 621

Atkins, R., et al. 2004, *Astrophys. J.*, 608, 680

Badran, H. M., Weekes, T. C., & the VERITAS Collaboration. 2001, in Proc. 27^{th} Int. Cosmic Ray Conference, Hamburg, 2653

Baganoff, F. K., Maeda, Y., & Morris, M. 2003, *Astrophys. J.*, 591, 891

Barth, A. J., Ho, L. C., & Sargent, W. L. W. 2003, *Astrophys. J.*, 583, 134

Becker, R. H., Helfand, D. J., & White, R. L. 1993, *Bulletin of the American Astronomical Society*, 25, 1445

Beilicke, M., Ouchrif, M., Rowell, G., & Schlenker, S. 2004, *The Astronomer's Telegram*, 249

Berge, D., Funk, S., Hinton, J., Lemoine-Goumard, M., de Naurois, M., Rolland, L., & the H.E.S.S Collaboration. 2005, in Proc. 2^{nd} Int. Symposium High Energy Gamma-Ray Astronomy, Heidelberg 2004. AIP Conf. Proc., Vol. 745, 263

Bernlöhr, K. 2001, in Astronomische Gesellschaft Meeting Abstracts, 304

Biermann, P. L., & Strittmatter, P. A. 1987, *Astrophys. J.*, 322, 643

Bloom, J. S., et al. 1999, *Astrophys. J.*, 518

Bock, R. K., & the MAGIC Collaboration. 2005, in Proc. 2^{nd} Int. Symposium High Energy Gamma-Ray Astronomy, Heidelberg. AIP Conference Proc., Vol. 745, 628

Boone, L. M., & the STACEE Collaboration. 2002, *Bulletin of the American Astronomical Society*, 34, 1266

Bradbury, S. 1997, in Proc. Int. Workshop Towards a Major Cherenkov Detector V, Kruger Park, 365

Carter-Lewis, D. 1992, Internal VERITAS Coll. Memo (unpublished)

Catanese, M., et al. 1998, *Astrophys. J.*, 501, 616

Catanese, M., et al. 1997, *Astrophys. J. Lett.*, 487, L143

Chadwick, P. M. 1998, *Astrophys. J.*, 503, 391

Chadwick, P. M., et al. 1999, *Astrophys. J.*, 513, 161

Condon, J. J., & Broderick, J. J. 1985, *Astron. J.*, 90, 2540

Coppi, P. S., & Aharonian, F. A. 1999, *Astrophys. J. Lett.*, 521, L33

Davies, J. M., & Cotton, E. S. 1957, *Solar Energy Sci. Eng.*, 1, 16

de la Calle Perez, I. 2003, Ph.D. thesis, University of Leeds (unpublished)

Dopita, M. 1997, *Publications of the Astronomical Society of Australia*, 14, 230

Douglas, J. N., Bash, F. N., Bozyan, F. A., Torrence, G. W., & Wolfe, C. 1996, VizieR Online Data Catalog, 8042

Dowdall, C. 2003, M.Sc thesis, Galway-Mayo Institute of Technology (unpublished)

Drury, L. O., Aharonian, F. A., & Völk, H. J. 1994, *Astronomy and Astrophysics*, 287, 959

Dunlea, S. 2001, Ph.D. thesis, National Universtity of Ireland (unpublished)

Dunlea, S., Moriarty, P., & Fegan, D. J. 2001, in Proc. 27^{th} Int. Cosmic Ray Conf., Hamburg, 2939

Dwek, E., & Krennrich, F. 2005, *Astrophys. J.*, 618, 657

Eiderlman, S., Plummer, D., & Schachter, J. 2004, *Phys. Lett. B*, 592, 1

Elvis, M., Plummer, D., & Schachter, J. 1992, *Astrophys. J.*, 257

Enomoto, R., et al. 2002, *Astropart. Phys.*, 16, 235

Falomo, R., & Kotilainen, J. K. 1999, *Astronomy and Astrophysics*, 352, 85

Fanaroff, B. L., & Riley, J. M. 1974, *Mon. Not. R. Astr. Soc.*, 167, 31

Feenberg, E., & Primakoff, H. 1948, *Physical Review*, 73, 449

Fegan, S. J. 2005, VERITAS Collaboration Meeting, Rio Rico, Arizona (unpublished)

Finley, J. P., et al. 2000, in Proc. GeV-TeV Gamma-ray Astrophysics Workshop, Snowbird, Utah, 1999. AIP Conf. Proc., Vol. 515, 301

Frail, D. A. 2001, *Astrophys. J.*, 562, L55

Gaidos, J. A., et al. 1996, *Nature*, 383, 319

Gammell, S. 2004, Ph.D. thesis, National University of Ireland, Dublin (unpublished)

Giommi, P., Perri, M., & Fiore, F. 2000, *Astronomy and Astrophysics*, 362, 799

Gnedin, O. Y., & Primack, J. R. 2004, *Phys. Rev. Lett.*, 93, 1302

Gregory, P. C., Capak, P., Gasson, D., & Scott, W. K. 2000, in Proc. IAU Symp. 205, Manchester, 98

Hand, D. J. 1982, Kernel Discriminant Analysis (Somerset, N.J.: John Wiley and Sons, Inc.)

Hartman, R. C., et al. 1999, *Astrophys. J. Suppl.*, 123, 79

Hayakawa, S. 1952, *Prog. Theo. Phys.*, 8, 571

Helene, O. 1984, *Nucl. Instrum. Methods A*, 228, 120

Hillas, A. M. 1985, in Proc. 19^{th} Int. Cosmic Ray Conf., La Jolla, Vol. 3, 445

Hillas, A. M., et al. 1998, *Astrophys. J.*, 503, 744

Hinton, J. A. 2004, *New Astronomy Review*, 48, 331

Hjorth, J., et al. 2003, *Nature*, 423, 847

Hofmann, W. 2005, in Proc. Conf. Towards a Network of Atm. Cher. Det. VII, Palaiseau (forthcoming)

Holder, J., et al. 2003, *Astrophys. J. Lett.*, 583, L9

Holder, J., & the Celeste Collaboration. 2001, in Proc. Int. Symp. High Energy Gamma-ray Astronomy. Heidelberg 2000. AIP Conf. Proc., Vol. 558, 635

Holmström, L., Sain, S. R., & Miettinen, H. E. 1995, *Computer Physics Communications*, 88, 195

Horan, D., & Weekes, T. C. 2004, *New Astronomy Review*, 48, 527

Horns, D., & Konopelko, K. 2002, *The Astronomer's Telegram*, 96

Hutchinson, G. W. 1952, *Philos. Mag.*, 43, 847

Itoh, C., et al. 2003, *Astronomy and Astrophysics*, 402, 443

Jarrett, T., Huchra, J., Schneider, S., Cutri, R., & Chester, T. 2003, in Proc. IAU Symp. 216: Maps of the Cosmos, Sydney

Kellermann, K. I., Sramek, R., Schmidt, M., Shaffer, D. B., & Green, R. 1989, *Astron. J.*, 98, 1195

Kertzman, M. P., & Sembroski, G. H. 1994, *Nucl. Instrum. Methods A*, A343, 629

Konopelko, A. 1999a, in Proc. 26^{th} Int. Cosmic Ray Conf., Salt Lake City, Vol. 3, 426

Konopelko, A. 1999b, *Astropart. Phys.*, 11, 135

Konopelko, A. 2000, in Proc. GeV-TeV Gamma-ray Astrophysics Workshop, Snowbird, Utah, 1999. AIP Conf. Proc., Vol. 515, 159

Konopelko, A., et al. 1999, *Astropart. Phys.*, 10, 275

Kosack, K., et al. 2004, *Astrophys. J. Lett.*, 608, L97

Kouveliotou, C. 1993, *Astrophys. J. Lett.*, 413, L101

Krawczynski, H., Coppi, P. S., & Aharonian, F. 2002, *Mon. Not. R. Astr. Soc.*, 336, 721

Krawczynski, H., et al. 2003, AAS/High Energy Astrophysics Division, 7

Krennrich, F., et al. 2001, *Astrophys. J. Lett.*, 560, L45

Krennrich, F., et al. 2002, *Astrophys. J. Lett.*, 575, L9

Krolik, J. H. 1999, Active Galactic Nuclei: from the central black hole to the galactic environment (Princeton, Princeton University Press)

LeBohec, S., & Holder, J. 2003, *Astropart. Phys.*, 19, 221

Leroy, N., & the H. E. S. S. Collaboration. 2004, in SF2A-2004: Semaine de l'Astrophysique Francaise

Lessard, R. W. 1999, Whipple Collaboration Internal Memo (unpublished)

Levinson, A. 2000, *Phys. Rev. Lett.*, 85, 912

Li, T., & Ma, Y. 1984, *Chinese Astronomy and Astrophysics*, 8, 151

Lin, Y. C., et al. 1999, *Astrophys. J.*, 525, 191

Longair, M. 1992, High Energy Astrophysics Vol. I, 2^{nd} edition (Cambridge, Cambridge University Press)

Mannheim, K. 1993, *Astronomy and Astrophysics*, 269, 67

Mannheim, K. 1995, *Astropart. Phys.*, 3, 295

Mao, S., Narayan, R., & Piran, T. 1994, *Astrophys. J.*, 420, 171

Matthews, J., et al. 1991, *Astrophys. J.*, 375, 202

McBreen, B., Ball, S. E., Campbell, M., Greisen, K., & Koch, D. 1973, *Astrophys. J.*, 184, 571

Mohanty, G., et al. 1998, *Astropart. Phys.*, 9, 15

Moriarty, P., & Samuelson, F. W. 2000, in Proc. GeV-TeV Gamma-ray Astrophysics Workshop, Snowbird, Utah, 1999. AIP Conf. Proc., Vol. 515, 338

Morrison, P. 1958, *Il Nuovo Cimento*, 7, 858

Mukherjee, R., et al. 1997, *Astrophys. J.*, 490, 116

Muraishi, H., et al. 2000, *Astronomy and Astrophysics*, 354, L57

Nilsson, K., Pursimo, T., Takalo, L. O., Sillanpää, A., Pietilä, H., & Heidt, J. 1999, *Publ. Astr. Soc. Pacific*, 111, 1223

Nishiyama, T. 1999, in Proc. 26^{th} Int. Cosmin-ray Conf., Salt Lake City, 370

Paciesas, W. S., Preece, R. D., Briggs, M. S., & Mallozzi, R. S. 2001, in Proc. Int. Workshop: Gamma-ray Bursts in the Afterglow Era, Rome 2000, 13

Padovani, P. 1997, in Proc. Moriond Workshop: Very High Energy Phenomena in the Universe, 7

Patnaik, A. R., Browne, I. W. A., Wilkinson, P. N., & Wrobel, J. M. 1992, *Mon. Not. R. Astr. Soc.*, 254, 655

Perlman, E. S., et al. 1996, *Astrophys. J. Suppl.*, 104, 251

Punch, M., et al. 1992, *Nature*, 358, 477

Punch, M., et al. 1991, in Proc. 22^{th} Int. Cosmic Ray Conf., Dublin, 464

Quinn, J., et al. 1996, *Astrophys. J. Lett.*, 456, L83

Quinn, J., Hughes, P., & Gammell, S. 2001, Internal VERITAS Coll. Memo (unpublished)

Rees, M. J. 1966, *Nature*, 211, 468

Schroedter, M. 2004, Ph.D. thesis, the University of Arizona (unpublished)

Schroedter, M. 2005, *Astrophys. J.* (submitted)

Semenov, V., Dyadechkin, S., & Punsly, B. 2004, *Science*, 305, 978

Sikora, M., Begelman, M. C., & Rees, M. J. 1994, *Astrophys. J.*, 421, 153

Skelton, P. 1999, Ph.D. thesis, the University of Leeds (unpublished)

Stecker, F. W., de Jager, O. C., & Salamon, M. H. 1992, *Astrophys. J. Lett.*, 390, L49

Stevens, J. A., & Gear, W. K. 1999, *Mon. Not. R. Astr. Soc.*, 307, 403

Stickel, M., Meisenheimer, K., & Kuehr, H. 1994, *Astron. Astrophys. Suppl. Ser.*, 105, 211

Stocke, J. T., Morris, S. L., & Gioia, I. 1990, *Astrophys. J.*, 348, 141

Takahashi, T., et al. 1996, *Astrophys. J. Lett.*, 470, L89

Thompson, D. 1995, *Astrophys. J. Suppl.*, 101, 259

Tluczykont, M. 2003, in Proc. 28^{th} Int. Cosmic Ray Conf., Tsukuba, 2547

Tsuchiya, K. 2004, *Astrophys. J. Lett.*, 606, 115

Ueno, M., Ichikawa, T., Sato, S., Kasaba, Y., & Ito, M. 1994a, in Astrophysics and Space Science Library 190: Infrared Astronomy with Arrays, The Next Generation, 119

Ueno, S., Mushotzky, R. F., Koyama, K., Iwasawa, K., Awaki, H., & Hayashi, I. 1994b, *Publ. Astr. Soc. Japan*, 46, 71

Urry, C. M., & Padovani, P. 1995, *Publ. Astr. Soc. Pacific*, 107, 803

Urry, C. M., Scarpa, R., O'Dowd, M., Falomo, R., Pesce, J. E., & Treves, A. 2000, *Astrophys. J.*, 532, 816

Vassiliev, V. 2000, in Proc. Texas Symp. Relativistic Astrop. and Cosm., Paris, 1998. Nuclear Physics B Proc., Vol. 80, 130

Völk, H. J., Klein, U., & Wielebinski, R. 1989, *Astrophys. J. Lett.*, 213, 12

Weekes, T. C. 1989, *Astrophys. J.*, 342, 379

Weekes, T. C. 2000, in Proc. GeV-TeV Gamma-ray Astrophysics Workshop, Snowbird, Utah, 1999. AIP Conf. Proc. 515, 3

Weekes, T. C. 2003, Gamma-Ray Astronomy (Bristol: Institute of Physics Publishing)

Weekes, T. C., et al. 2002, *Astropart. Phys.*, 17, 221

Xie, G. Z., Li, K. H., Bai, J. M., Dai, B. Z., Liu, W. W., Zhang, X., & Xing, S. Y. 2001, *Astrophys. J.*, 548, 200